Optimization of the positioning of sensors and energy harvesters for the design of portable physical activity recognition systems

Damien Hoareau

To cite this version:

Damien Hoareau. Optimization of the positioning of sensors and energy harvesters for the design of portable physical activity recognition systems. Mechanical engineering [physics.class-ph]. Université de Rennes, 2023. English. NNT : 2023URENE006 . tel-04470223

HAL Id: tel-04470223
https://theses.hal.science/tel-04470223v1

Submitted on 21 Feb 2024

COLLEGE DOCTORAL BRETAGNE
MATHS, TELECOMS
INFORMATIQUE, SIGNAL
SYSTEMES, ELECTRONIQUE

école
normale
supérieure
rennes

THÈSE DE DOCTORAT DE

L'ÉCOLE NORMALE SUPÉRIEURE DE RENNES

ÉCOLE DOCTORALE Nº 601
Mathématiques, Télécommunications, Informatique, Signal, Systèmes, Électronique
Spécialité : *EGE-FOT*

Par
Damien Hoareau

Optimisation du positionnement de capteurs et de récupérateurs d'énergie pour la conception de systèmes portables de reconnaissance d'activité physique.

Thèse présentée et soutenue à l'ENS de Rennes, le 10 juillet 2023
Unité de recherche : CNRS UMR 8029, laboratoire SATIE

Rapporteurs avant soutenance :

Gérard Dray	Professeur des universités à IMT Mines Alès
Isabelle Dufour	Professeure des universités à l'Université de Bordeaux

Composition du Jury :

Président : Gérard Dray, Professeur des universités à IMT Mines Alès
Examinateurs : Elie Lefeuvre, Professeur des universités à l'Université de Paris-Saclay
Encadrant de thèse : Gurvan Jodin, Agrégé préparateur à l'École normale supérieure de Rennes
Encadrant de thèse : Jacques Prioux, Professeur des universités à l'École normale supérieure de Rennes
Dir. de thèse : Florence Razan, Professeure des universités à l'École normale supérieure de Rennes

Invité(s) :

Charles Pontonnier	Maître de conférences à l'École normale supérieure de Rennes
Nicolas Bideau	Maître de conférences à l'Université de Rennes 2

REMERCIEMENTS

Durant mes trois années de thèse je n'ai cessé de remettre en question mes capacités. Parsemée d'obstacles, la route fut parfois longue et difficile, me laissant souvent uniquement entrevoir mes réussites. J'ai cependant eu la chance d'être entouré de personnes qui m'ont offert un soutien infaillible et qui m'ont accompagné tout au long de ce parcours. J'aimerais ainsi remercier toutes ces personnes, qui j'espère, comprendront à travers mes propos l'importance qu'ils ont eu pour moi.

Je remercie dans un premier temps les membres de mon jury : Gérard Dray, Isabelle Dufour, Elie Lefeuvre, Charles Pontonnier et Nicolas Bideau. Merci pour nos échanges autour de mon manuscrit et de ma soutenance de thèse. Les remarques bienveillantes et les questionnements dont vous m'avez fait part ont permis des discussions intéréssantes et ont renforcé mon choix de continuer dans la même direction.

Je remercie également mes encadrants de thèse sans qui tout ça n'aurait pas été possible : Jacques Prioux, Gurvan Jodin, Florence Razan. Merci pour votre bonne humeur et votre soutien tout au long de ces trois années, vous avez su vous rendre disponible pour moi malgré vos contraintes. Vos conseils et remarques m'ont beaucoup apporté. Vous avez réussi à me rassurer quand il le fallait et je vous en suis très reconnaissant. C'est en partie grâce à vous que je suis devenu qui je suis, merci encore.

Je remercie ma famille qui, même située de l'autre côté de l'équateur, m'a soutenu tout au long de mon parcours. C'est aujourd'hui avec un sentiment d'accomplissement et de fierté que je partage avec vous ce que j'ai réussi.

Cela fait maitenant sept années que l'on se connaît, au début binôme de cours et à la fin colocataire, c'est à ton tour d'être remercié Hassen Soualah (aka le %, le BZD, et tous les autres acronymes que je ne citerai pas). Comme tu as pu le voir, cette thèse n'a pas toujous été facile pour moi, il y a eu des périodes compliqués. Plus que tu ne le pense, ta bonne humeur, nos discussions, nos sessions de jeux vidéos ont participés à mon bien être. C'est pour tout cela que je te remercie. Je ne t'oublie pas le troisième coloc Clément Trotobas, malgré la distance, on a su trouver des moments pour "acheter/vendre des offres en or" (les abonnements d'un an ne sont pas rentables). Merci pour tous ces moments de joie et de rigolade.

Je remercie également Alexia Marsal. Merci pour ton soutien et de m'avoir apporté tout ce dont j'avais besoin. J'ai toujours pu compter sur toi spécialement durant cette dernière année de thèse qui a été des plus intense. Grâce à toi les obstacles me paraissent beaucoup moins infrachissables, merci de m'accompagner dans mon quotidien.

Je remercie aussi Nikita Houdot. Merci pour ton énergie et toutes ces sorties décompressantes. C'est à chaque fois un réel plaisir, je suis désolé pour les samoussas du pot de thèse que tu n'as pas pu goûter.

Merci à mes amis avec lesquels je passe des moments toujours aussi agréables : Romain, Adèle, Bastien, Anas, Cédric, Mirado, Sarah, Laura, Clara, Loick, Vincianne, Alexis, Aténé. Merci de m'avoir permis d'avancer grâce à votre bonne humeur.

Je remercie également mes collègues de l'ENS et des divers laboratoires avec lesquels j'ai pu échanger tout au long de ma thèse et qui ont toujours su offrir une bonne ambiance : Guénolé, Briac, Thibault, Béatrice, Youen, Marvin, Simon, Alexandre, Zinédine, Lancelot, Pauline, Claire, Pierre-Antoine, Ibrahim, Benjamin, Hamid, Sara, Charles, Sébastien G., Sébastien H., Patrice, Marielle, Roman, George, Damien G., Olivier, Sophie.

Merci aux étudiants avec qui j'ai pu travailler lors de leur stage : Damien H., Clémence, Julien, Arnaud, Corentin, Benoît, Mathis. Ce fut un réel plaisir de travailler avec vous.

Enfin, je remercie le laboratoire Karolinska Institutet et CAMM pour m'avoir acceuilli avec la plus grande bienveillance lors de ma mobilité ERASMUS+. Je remercie plus particulièrement ma tutrice Liyun Yang et mes collègues : Xuelong Fan, Mélanie, Julio, Nuria, Alicia, André.

TABLE OF CONTENTS

LIST OF ABBREVIATIONS

ACO	Ant colony optimization
AI	Artificial intelligence
ANN	Artificial neural network
AWGN	Additive white Gaussian noise
BMI	Body mass index
CNN	Convolutional neural network
CusToM	Customizable Toolbox for Musculoskeletal simulation
CWT	Continuous wavelet transform
DA	Deflection axis
DBN	Deep belief network
DC	Direct current
DT	Decision tree
EIE	Extracted impact energy
EMG	Electromyography
FFT	Fast Fourier transform
GA	Genetic algorithm
GPS	Global positioning system
GRU	Gated recurrent unit
HAR	Human activity recognition
HMM	Hidden Markov model
HOG	Histogram of oriented gradients

I3D	Inflated-3D
IMU	Inertial measurement unit
k-NN	k-Nearest neighboor
LCA	Life cycle analysis
LPS	Local positioning system
LR	Logistic regression
LSTM	Long short-term memory
MAE	Mean absolute erro
MEMS	Micro-electromechanical system
MMH	Manual Material Handling
MoCap	Motion capture
MODWT	Maximum overlap discrete wavelet transform
MRF	Most relevant feature
MSD	Musculoskeletal disorder
NN	Neural network
NSGA	Non-dominated sorting genetic algorithm
PCA	Principal component analysis
PEG	Piezoelectric generator
PSD	Power spectral density
PSO	Particle swarm optimization
PV	photovoltaic
RBF	Radial basis function
RF	Radio frequency (1)
RF	Random forest (2)
RID	Real IMU data

RMSE	Root mean square error
RNN	Recurrent neural network
RRP	Robustness - Reliability - Precision
SAAS	Smart activity assessment system
SD	Standard deviation
SID	Synthesized IMU data
SMEEI	Simulated model energy of extracted impacts
SVM	Support vector machine
SysML	Systems modeling language
TSE	Total signal energy
TSME	Total simulated model energy
VGG	Visual geometry group

LIST OF FIGURES

LIST OF TABLES

RÉSUMÉ EN FRANÇAIS

Située à l'interface entre les capteurs portables et les problématiques de l'analyse du mouvement, cette thèse s'intérèsse à la reconnaissance de l'activité humaine à travers une approche systémique.

L'analyse du mouvement comprend de nombreux champs d'applications comme la santé, le sport ou l'ergonomie. Les enjeux se situent dans le domaine de l'instrumentation, du matériau au système notamment dans la conception de systèmes embarqués autonomes. Parmi les capteurs les plus utilisés, on retrouve les centrales inertielles généralement composées d'un accéléromètre, d'un gyroscope et/ou d'un magnétomètre. Leur faible coût, leur légèreté et leur compacité offrent de grands avantages quant à leur intégration dans les systèmes embarqués. On trouve l'utilisation de centrales inertielles et de goniomètres pour l'évaluation des postures de l'utilisateur [1] ou encore pour la quantification de la charge de travail des sportifs [2]. Ainsi, la taille du marché des centrales inertielles se voit grandir avec une augmentation estimée à 13.08 % (taux de croissance cumulée 2022-2027) [3]. Les applications se fondant sur l'utilisation de ces centrales inertielles sont de plus en plus nombreuses. Partie intégrante de l'analyse du mouvement, on trouve la reconnaissance d'activité humaine. Cela consiste généralement à classifier de façon automatique des actions effectuées par l'utilisateur. En s'appuyant sur différentes configurations de centrales inertielles et de méthodes de classification, plusieurs applications de reconnaissance d'activité sont présentées dans la littérature [4, 5] et constituent un premier verrou. Cependant, le placement des centrales inertielles sur le corps humain n'est pas trivial. En effet, la précision de la reconnaissance dépend non seulement des paramètres des méthodes employées mais aussi intrinsinquement du positionnement de ces capteurs. Ainsi, il est nécessaire de s'assurer du placement optimal de ces capteurs pour prétendre à l'obtention d'une précision optimale de la reconnaissance d'activité. D'après nos recherches, il n'existe pas de méthode générale permettant d'obtenir ces optimums de positions. C'est une problématique commune à toutes les applications.

Un autre verrou des systèmes embarqués pour la reconnaissance du mouvement consiste à s'interroger sur les aspects énergétiques. L'autonomie d'un système de reconnaissance de l'activité humaine est un pilier important ajoutant flexibilité et confort dans l'analyse des mouvements humain. L'alimentation des divers capteurs et organes présents se fait habituellement par l'utilisation de piles ou batteries. Néanmoins, dans un objectif de développement durable, il est nécessaire de reconsidérer cette question. Il existe de nos jours d'autres moyens d'alimenter les systèmes électriques comme par exemple l'utilisation de récupérateurs d'énergies [6]. Parmi les plus répandus, on retrouve les récupérateurs d'énergie cinétique comme les générateurs piezoélectriques [7]. Offrant une bonne versatilité et adaptabilité, ils peuvent être utilisés dans de nombreuses configurations différentes sur le corps humain. Plus particulièrement, l'utilisation de poutres piezoélectriques présente un réel intérêt pour la récupération d'énergie [8, 9]. Cependant, la conception de ces systèmes vibrants pour des signaux non stationnaires comme les accélérations est complexe, en particulier pour les signaux avec des grandes dynamiques comme les activités sportives. De plus, l'energie récupérée est dépendante de la position et de l'orientation du générateur sur le corps humain. Réaliser des mesures expérimentales n'est pas simple car cela nécessite une instrumentation lourde (appareils à très haute impédance) limitant les mouvements de l'utilisateur.

Ainsi, les contributions apportées par cette thèse concerne de manière globale la détermination des positions optimales de centrales inertielles sur le corps humain pour la reconnaissance d'activité, mais aussi la détermination du placement et de l'orientaion optimal de générateurs piezoélectriques sur le corps humain. Cette thèse est en 4 parties : la première partie concerne la mise en place des outils nécessaires pour déterminer le placement optimal des centrales inertielles ; la deuxième partie concerne l'étude de l'énergie récupérable sur le corps humain par des poutres piezoélectriques ; la troisième partie traite de l'optimisation de la reconnaissance d'activité et de la consommation énergétique ; et enfin la dernière partie s'intéresse à un aspect plus pratique, plus précisément l'évaluation d'un système de capteurs intégrés dans un vêtement.

— **Partie 1 :** Cette première partie concerne la mise en place des outils nécessaires à l'évaluation des positions optimales de centrales inertielles sur le corps humain. L'évaluation expérimentale de toutes les positions du corps humain n'est pas faisable : cela implique dans un premier temps d'instrumenter entièrement le corps de l'utilisateur ce qui engendrerait un inconfort et un potentiel risque de blessures; dans un deuxième temps cela nécessite trop de ressources matériels et temporelles. Pour palier à ce problème, notre approche se base sur la synthèse de données issues d'un modèle biomécanique. Ainsi, il est possible d'obtenir en chaque point de ce modèle biomécanique les grandeurs physiques d'accélérations et de vitesses.Tout d'abord, il est nécessaire de vérifier la fiabilité des données synthétisées pour mener des investigations quant à la reconnaissance d'activité. Les résultats ont montré que l'utilisation des données synthétisées permet de tester de nombreuses positions de capteurs réels sans faire d'expérimentations pour trouver les positions optimales des centrales inertielles. Cette étude a fait émerger de nouveaux verrous, orientant ainsi les perspectives. Ces résultats sont établis sous certaines hypothèses, notament l'absence de l'influence des corps mous; hypothèse abordée dans la partie 4.

— **Partie 2 :** Cette seconde partie s'intéresse à l'autoalimentaiton d'un système porté et plus particulièrement à la récupération d'énergie piezoélectrique sur le corps humain. Ici encore, les installations expérimentales nécessitent des contraintes limitant les actions effectuées par l'utilisateur. De plus, le temps nécessaire pour tester exhaustivement toutes les configurations possibles serait trop important. On propose donc une méthode permettant d'évaluer ces configurations mais aussi d'évaluer les caractéristiques pertinentes quant à la génération d'énergie par les poutres piezoélectriques. À partir des accélérations réelles mesurées, un modèle à paramètres distribués de poutre piezoélectrique est simulé pour prédire l'énergie récupérable sur le corps humain. Ainsi, les emplacements et orientations optimales sont évaluées numériquement sur 17 positions du corps humain à partir de mesures d'accélérations réelles. Les résultats ont montré que dans notre application, la main droite était la meilleure position. Il est à noter que les expériences ont été conduites sur un seul sujet sur un ensemble de mouvements sportifs limités. Un autre résultat est que les chocs dus aux actions effectuées ont été identifiés comme caractéristiques pertinentes pour générer de l'énergie. La limitation principale de cette étude est la fréquence d'échantillonnage des capteurs ne permettant pas de caractériser entièrement les chocs mesurés.

— **Partie 3 :** Cette troisième partie traite de manière générale d'optimisation pour concevoir un système portable de capteurs. Elle est séparée en 2 parties. L'une concerne l'évaluation des positions optimales de centrales inertielles tout en considérant un aspect énergétique; et l'autre analyse l'influence de la géométrie des poutres piézoélectriques sur la récupération d'énergie sur le corps humain.

L'évaluation des positions optimales de centrales inertielles est réalisée à travers une optimisation multi-critères visant à maximiser la précision de la reconnaissance

et à minimiser la puissance consommée. La formulation du problème nous oriente vers l'utilisation d'un algorithme génétique. Les compromis entre reconnaissance optimale et consommation minimale sont illustrés à travers un front de Pareto. Ainsi, les meilleurs compromis énergie/information apparaissent comme des combinaisons de positions et configurations pour les centrales inertielles.
L'étude de l'influence de la geométrie des poutres est conduite en optimisant les orientations des générateurs. Les résultats montrent que pour une quantité de matière définie la position optimale varie en fonction de la géométrie. Les limitations sont les mêmes que celles définies précédemment. De plus, l'étude s'est limitée à quelques paramètres afin de ne pas augmenter d'autant plus la complexité du problème. Des études futures pourront se pencher plus en détail sur ces paramètres.

— **Partie 4 :** Cette dernière partie s'intéresse aux erreurs de mesures induites par l'intégration de centrales inertielles dans un vêtement. Cette partie se base sur des mesures expérimentales pour des applications dans le domaine de l'ergonomie. Les mouvements relatifs existants entre la peau et un vêtement peuvent induire des erreurs dans les mesures des centrales inertielles. On s'est intéressé ici à l'influence de ces artefacts sur la mesure des postures du haut du corps. Le système utilisé est composé de 3 centrales inertielles situées sur les épaules et le bas de la nuque. Grâce à des algorithmes de fusion de données, plus particulièrement le filtre de Kalman, on peut remonter aux orientations des capteurs puis des membres supérieurs. Comparées à un ensemble de capteurs placés directement sur la peau, les erreurs sont évaluées à travers une campagne de mesure (12 sujets, expérimentations réalisées en Suède). Les résultats ont montré que les erreurs induites par le mouvement relatif du vêtement étaient d'autant plus importantes si les mouvements effectués étaient de grandes amplitudes. Cette première étude a permis de mettre en évidence les erreurs existantes et de les quantifier. Les études futures visent l'utilisation d'algorithmes de compensation de ces erreurs.

Une étude de conception et d'intégration de centrales inertielles dans un vêtement a également débuté et la conception d'un premier prototype de système autonome de reconnaissance de l'activité a été réalisé (Figure 1).

Composé de centrales inertielles, d'un micro-contrôleur et d'une batterie, ce système récupère les données d'accélération et de vitesse angulaire et les sauvegarde localement sur une carte SD pour un traitement a posteriori. Cette première version a permis de mettre

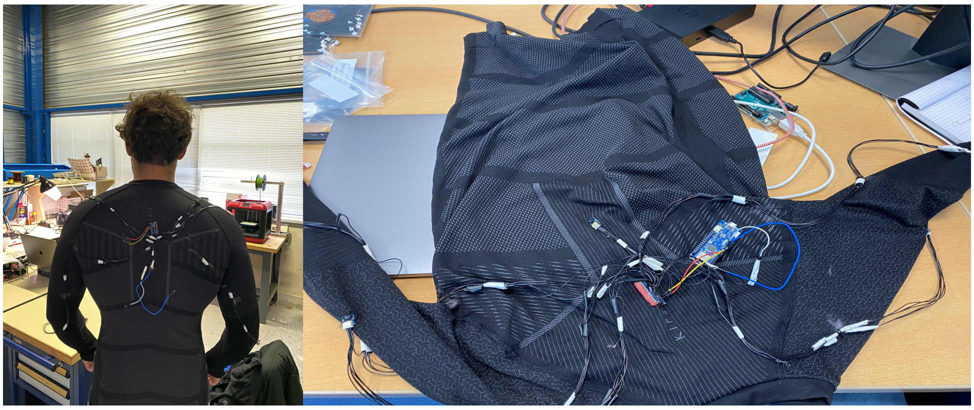

Figure 1 – Prototype de vêtement autonome pour la reconnaissance d'activité.

en évidence les difficultés d'intégration des capteurs dans un vêtement. Des perspectives sont envisagées, plus particulièrement sur l'utilisation de fils de couture conducteurs pour améliorer la robustesse des connexions.

Les contributions apportées lors de cette thèse ont permis de mettre en évidence les verrous existants quant à la conception d'un système autonome de reconnaissance d'activité humaine. Les difficultés de la reconnaissance d'activité mais aussi énergétiques sont abordées. Les limitations expérimentales sont les premiers obstacles vis-à-vis de la détermination des positions optimales. L'évaluation exhaustive des divers paramètres n'est pas faisable. La complexité numérique, ergonomique et temporelle réduit fortement les possibilité de manoeuvre. Cette thèse apporte également des outils pour apporter des réponses à ces verrous. L'utilisation d'un modèle biomécanique pour l'augmentation de données 'virtuelles' de centrales inertielles couplées aux algorithmes d'optimisations semblent être des candidats prometteurs pour répondre aux problématiques. La caractérisation des signaux d'accélérations peut servir à la conception des générateurs piezoélectriques afin d'optimiser l'énergie récupérable. Les méthodes présentées ont pour but de fournir aux lecteurs des lignes directrices illustrant d'autres types d'approches. Les cas d'études présentés pourront être investis plus en détail afin de proposer une application réelle. La conception d'un prototype plus avancé permettrait de tester les résultats obtenus numériquement mais également de mettre en évidence les contraintes réelles. Cette thèse est d'ores et déjà suivie d'une thèse sur la conception de capteurs flexibles portés.

INTRODUCTION

Watching the running time on a course with a stopwatch gives a good reference to improve next time, but what if one could now monitor the heart rate? the blood oxygen level? Information provided by sensors give objective measurements and allow the assessment of multiple parameters for improving human lives. Recent advances on sensors more specifically on wearable sensors offer possibilities of monitoring human parameters and their environment. Miniaturization and the development of new technologies allow the efficient integration of sensor networks in the most common things or in daily lives.

Among the most used wearable sensors, there are inertial measurement units (IMU) generally composed of accelerometers, gyroscopes and magnetometers. Using adapted signal processing, theses sensors can give kinematic and dynamic informations, useful to conduct motion analysis studies. The scope of application is wide: IMUs can be found in sport, health or ergonomic field. Sensor networks built from IMUs can give accurate measurement as their data fusion reduces the inherent measurements errors. Nevertheless, the information quality is dependent of the localization of the sensor on the human body. External factors such as parasitic movements (e.g., of the skin or flesh) and cloth artifact can also impact the measurements.

In human related application, collected data from IMU are mainly used in motion capture (MoCap) and human activity recognition (HAR). The Mocap application generally consists in using the data from the sensor network to calculate the joint angles and analyze the evolution of the human segments in space. HAR consists in using an adapted machine or deep learning algorithm (classical supervised method) to classify the different performed actions. The accuracy of the classification depends on various parameters and directly on the quality of the information coming from the sensor network and thus on their localization. In addition, learning algorithms require a large number of data to be efficient and show good results. However, to the best of our knowledge, there is no general method providing the best localization of IMUs on the human body to obtain the optimal accuracy for the designed application. Testing all combinations and locations of sensor networks are time consuming and are experimentally cumbersome.

The power consumption of sensors networks is also a field of interest. Multiplication of devices increases electrical energy needs, while recent low power sensors developments improve the energy efficiency. However, batteries are widely used in many applications and their design can be controversial. Another alternative investigates the harvesting energy capability from the human body. This solution can be more sustainable and limits the use of batteries. Kinetic energy harvesting is a promising candidate in motion analysis studies. Piezoeletric based harvester are commonly used as they provide good scalability and versatility. Notwithstanding, their positions and orientations impact the energy harvested. A detailed method does not exist for their optimal placement.

This thesis focuses on the analysis of human body information and energy sources for HAR using IMUs. The aim is to develop a general method to determine the optimal IMUs placement including classification hyperparameters aspects. In addition, described as an embedded system, available energy sources for wearable sensors powering are investigated.

The different parts are divided as follows:

- **Chapter 1**: This first chapter presents a general context on motion analysis applications, systems and methods. A more important focus is made on motion recognition. Moreover, energy aspects allowing the powering of portable systems are discussed, in particular the recovery of energy from the human body and its environment. Notions related to complex systems are introduced, especially optimization methods. The scientific positioning of this thesis closes this chapter, a more specific state of the art is associated with each beginning of chapter.
- **Chapter 2**: This chapter deals with the use of so-called synthesized data for the numerical evaluation of the positioning of inertial units in HAR applications. The use of this type of data allows to artificially increase the number of positions to be tested and thus limits the need for experiments.
- **Chapter 3**: This chapter addresses the energy aspects related to piezoelectric energy harvesters. An electromechanical model of a piezoelectric beam is simulated on human body accelerations. The optimal orientations as well as the characterization of the accelerations are performed.
- **Chapter 4**: This chapter is the prolongation of chapter 2 and 3, it deals with

the optimization of IMU and harvester configurations on the human body. Optimization algorithms like genetic algorithm or particular swarm optimization are implemented.

- **Chapter 5**: This chapter is based on more pratical aspects. Thanks to a collaboration with a research team based in Sweden, experiments have been carried out in order to evaluate the artifacts existing in a posture evaluation system integrating IMUs. The goal here is to evaluate the influence of the integration of IMUs in a garment. Moreover, a design aspect is introduced, the prototyping of an activity evaluation system is presented.
- **Chapter 6**: This chapter summarizes the results obtained in the various chapters and synthesizes them in the form of a conclusion. The scientific perspectives and challenges are discussed.

Chapter 1

STATE OF THE ART: ANALYSIS AND MONITORING SYSTEMS FOR HUMAN MOTION

This state of the art presents the contributions related to human activity recognition from an intelligent and autonomous system. First, the application fields and the tools used in motion analysis are introduced. The contributions in this field are more and more numerous and let appear new opportunities but also new problematics. We will mainly deal with motion analysis by activity recognition, which is a more and more fashionable method. Indeed, the use of artificial intelligence (AI) algorithms allows to classify or to recognize in an automatic way the actions performed by the human body by using various supports like IMU. In a second time, we will approach the energetic aspects, which is necessary to the realization of autonomous system. Then, by the use of engineering tools, optimization approaches are investigated. Based on the existing contributions, the objectives of this thesis will be introduced by our scientific positioning.

1.1 General context

The monitoring and analysis of human motion is becoming more and more efficient thanks to the emergence of new methods and technologies. It consists in the analysis of human biomechanics, translated by the analysis of the mechanical properties of living beings. Extraction of data of interest allow competent experts, such as physical trainers, clinicians or future users to have feedback for professional interpretation. The main applications can be found in health, ergonomic and sport related field. In addition, with the development of the wearable sensor market, application deployment is diversifying and providing new opportunities. The Figure 1.1 presents the wearable technology market size from 2021 to 2030.

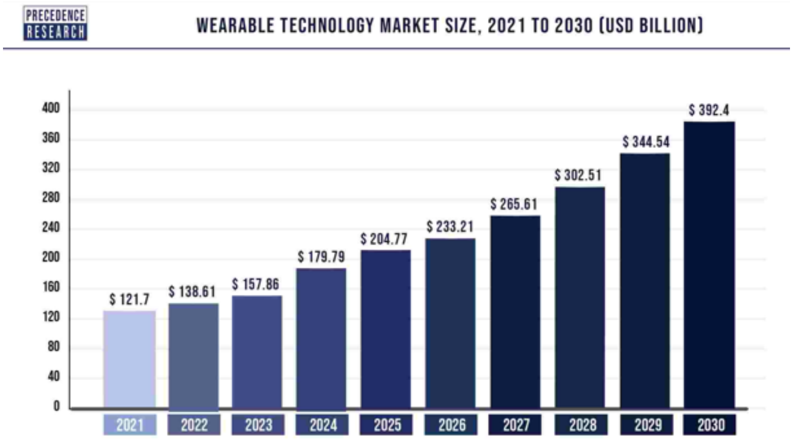

Figure 1.1 – World wearable technology market size, forecast 2022-2030 [10].

The market size was estimated at 121.7 billion USD in 2021 and is expected to reach around 392.4 billion USD by 2030. This highlights the interest in the wearable technology. In addition, the integration of these sensors adds flexibility and feasibility in the measurements. Homayoufar et al. [11] present some challenges related to motion analysis based on wearable sensors. Embedding sensors in garments could provide users with comfort and long-term applications. We find among these sensors the IMU, which are increasingly used. They are generally composed of accelerometers, gyroscopes and magnetometers. Figure 1.2 presents the IMU market size and the expected growth over 2027. From 2017 to 2023 a growth of 13.08 % is observed (Year-over-Year growth rate). In addition, IMUs represents the most part of the global sensors market. Figure 1.3 presents the evolution of the IMUs market size comparing to other technologies. Accelerometers and gyroscopes are also increasingly used, they are part of IMUs. Main applications are presented next, highlighting the challenges on different research field.

1.1.1 Ergonomics applications

Improved work environments reduce the risk of injury. Among the most common related diseases are musculoskeletal disorders. These disorders can be due to bad postures but also to bad working conditions, for example without adapted equipment, or the repetition of stressful tasks. Surveys such as [13] show a slight decrease of these disorders but they remain widely present, as presented on Figure 1.4.

Figure 1.2 – Inertial measurement unit market size, forecast 2017-2027 [3]. A compound annual growth rate (CAGR) of 14.59 % is estimated, additional 7761.28 USD Million is expected over 2027.

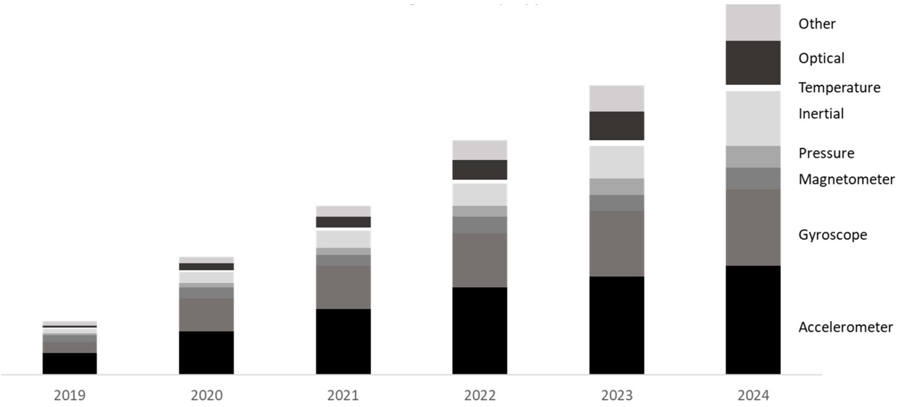

Figure 1.3 – Sensors market distribution [12].

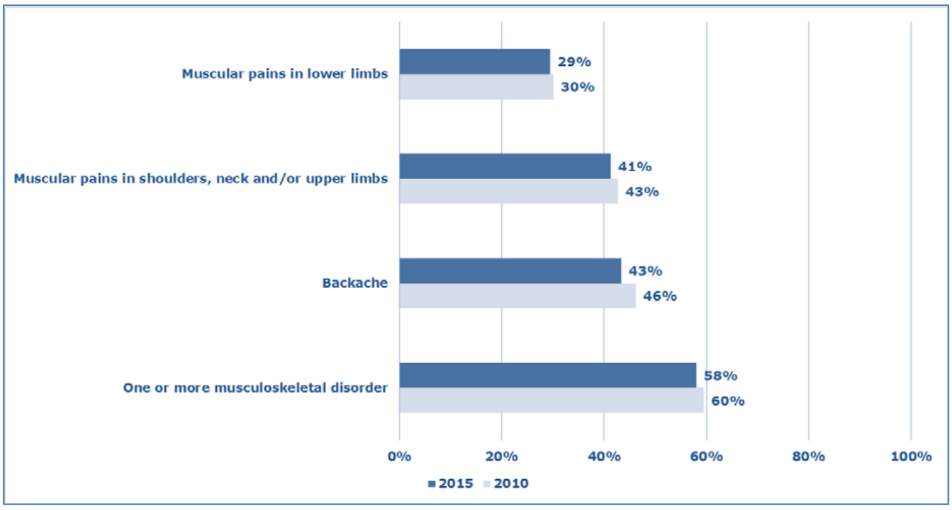

Figure 1.4 – Percentage of workers reporting different musculoskeletal disorders in the European Union [13]. Number of participant N = 33173 (2010); N = 31612 (2015).

Musculoskeletal disorders are up to 58 % (in 2015) highlighting the necessities to improve the working conditions. The analysis of movements and postures allows to evaluate the risks and thus to adapt these environments or working conditions [14]. The prevention of these risks can be carried out in real time and therefore limits the musculoskeletal disorders (Figure 1.5).

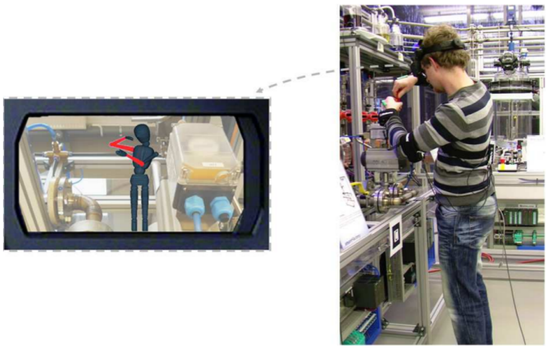

Figure 1.5 – Real-time visual ergonomic feedback system based on goniometers and IMUs [1].

1.1.2 Health applications

Other different disorders aspects are related to body movement. Some example of movement-related medical conditions are presented in Figure 1.6.

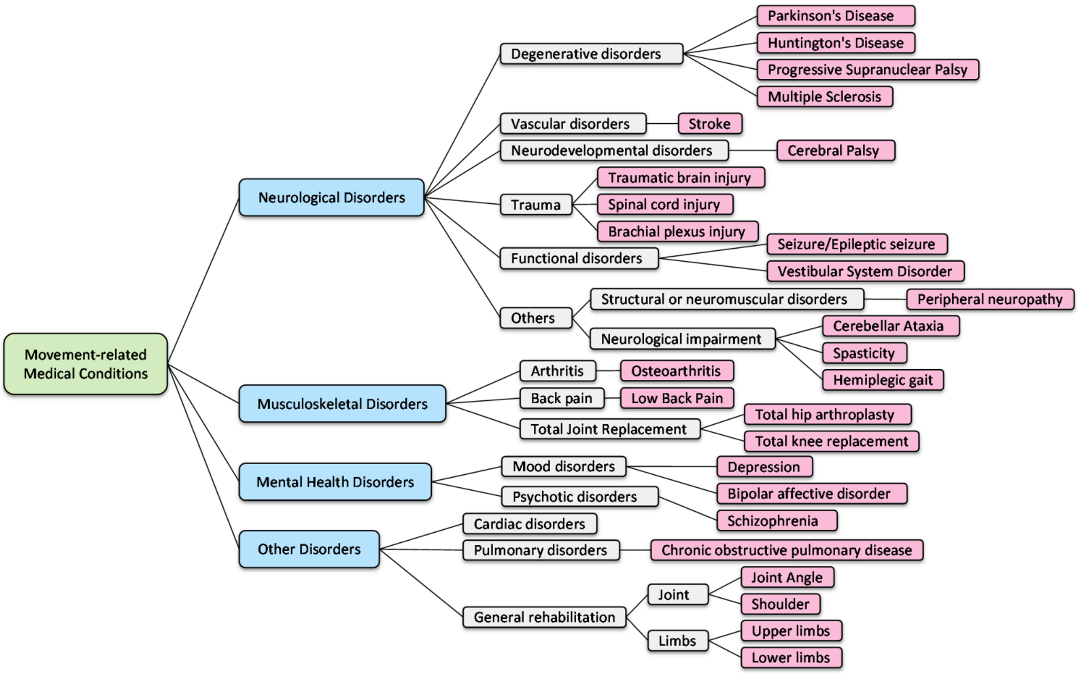

Figure 1.6 – Movement-related medical conditions (taxonomy of selected works extracted from [15]).

Human motion monitoring and analysis allow detection, evaluation and characterization of pathologies levels in patients. Thus, this improves the professional diagnostics to adapt the treatment or therapy. Figure 1.7 presents a sensing network system for health application based on wearable devices which can monitor environmental and physiological parameters. Movement analysis based on activity recognition implies less involvement of patients and can be very helpful for rehabilitation purposes [16]. Parkinson's disease severity level can be quantified by IMU based on classification algorithm [17].

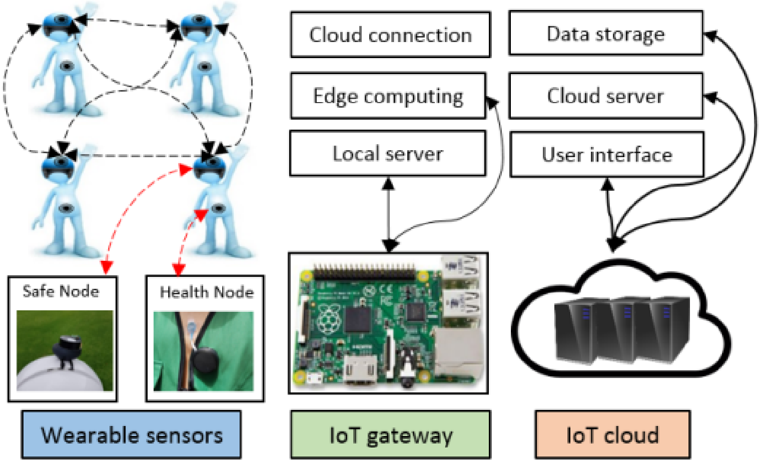

Figure 1.7 – Wearable sensor network system [18].

1.1.3 Sport applications

Continuous performance improvement is a real challenge in the sport field. The level of athletes is constantly increasing. New technologies bring new methods and approaches to continuously improve techniques and optimize training. Sports performance is at the heart of 4 major components as presented in Figure 1.8. The physical performance axis is directly related to the analysis of human movements.

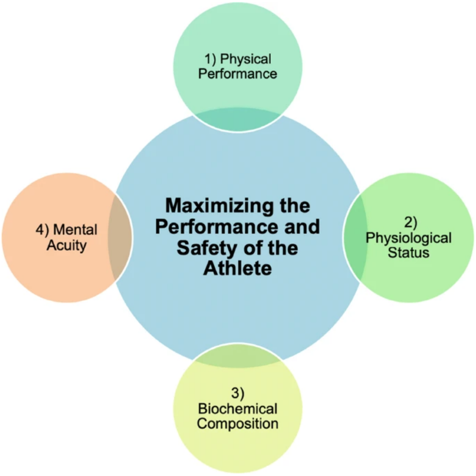

Figure 1.8 – Components of performance maximization and athlete safety [19].

Quantifying physical performance allows to adapt training, reduce the risk of injury or evaluate fatigue. This can be done in various ways and in different forms depending on the sport studied. In rugby, for example, it is interesting to study the acceleration and deceleration of players, which provides information on their energy expenditure. [20]. The tracking of the physical workload of the players is also an important aspect in order to adapt their training [21]. The recognition of actions allows to quantify the external load induced by the strikes in tennis players for example (Figure 1.9).

Figure 1.9 – Placement of an inertial measurement unit on the wrist for external load quantification [2].

In addition, localization and evaluation of the distance covered by team sport players allows the evaluation of movement patterns [22, 23].

1.2 Monitoring systems

There are many systems available to carry out motion analysis. The first step is to select the system to perform the desired measurement. Then, several physical quantities can be obtained as forces or speeds. In addition, there may be trade-offs between economic cost, accuracy, integrability and ergonomics of the systems. This section presents the most used systems for performing human motion analysis and monitoring.

1.2.1 Video cameras

Image frames acquired by video cameras give a lot of information. Motion capture can be performed using image processing. Vision-based algorithms are developed for HAR application. Cameras are mainly characterized by their resolution and sampling frequency. Systems such as Kinect cameras are widely used in research field. They are composed of RGB cameras and depth sensors (Figure 1.10).

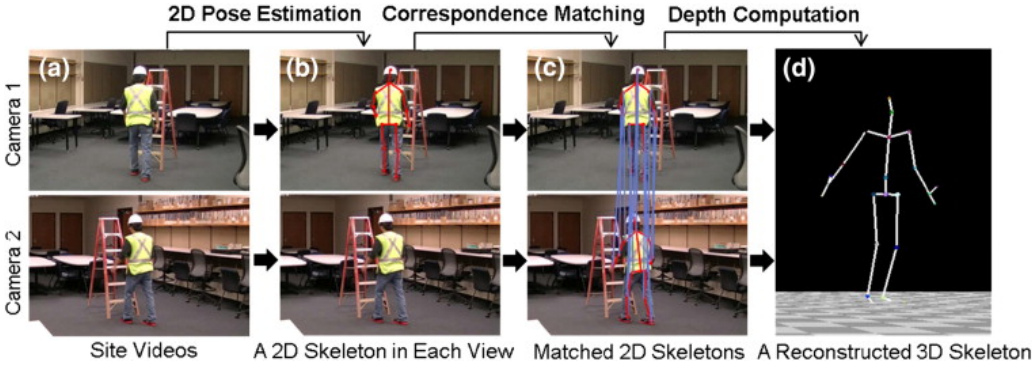

Figure 1.10 – Motion capture based on video camera [24].

These systems are markerless and therefore do not interfere with the actions performed by the monitored participants. Nevertheless, some drawbacks can not be overlooked:

- To obtain better results from video-based motion capture, it is necessary to increase the number of cameras and thus the cost [25].
- The performed activities should be in the field of view of the cameras. Brightness and ambient light can impact the measurements quality.
- The level of accuracy can not be sufficient for some applications [26],[27]. Taking joint angle estimation applications, errors can reach several dozen of degrees.

1.2.2 GPS/LPS

Based on the use of satellites, the global positioning system (GPS) allows to follow the position of a point on the surface of the earth in a very large area. Thus, we can study the movements of people in a defined environment. However, this requires a good coverage of the area by the satellites. Interference due to the environment or the atmosphere can reduce the accuracy. Thus, indoor applications are not feasible. Another method is the use of radio frequency transmitters to define a local position tracking perimeter,i.e., the local positioning system (LPS). Figure 1.11 presents the LPS Catapult[1] used in a football. The positioning system is located on the back of the individual and ultra-wideband radio frequency is used. This method offers more robustness and accuracy but is limited to a certain area, has a high cost (> 30 000 Euros for the whole system) and requires much installation.

---

[1] www.catapultsports.com

Figure 1.11 – Catapult system for local positioning. The device is located on the back of the players [28].

1.2.3 Optoelectronic Systems

1.2.3.1 Acquisition system

Motion capture of human body can be performed with optoelectronic systems like Vicon[2] or Qualisys[3]. Reflective markers are placed on the human body and are captured by infrared cameras (Figure 1.12).

Figure 1.12 – Vicon motion capture system [29].

The localization of each reflective marker are recorded in 3D space using triangulation at a fixed time rate. Experimental data are then processed to build a numerical

---

[2] https://www.vicon.com/

[3] https://www.qualisys.com/

biomechanical model of the human body. Optoelectronic systems are considered as gold standard for motion capture measurement as they provide very good accuracy (< 1 mm) [30]. Nevertheless, this system is sensitive to brightness and requires a dedicated space for its installation. Moreover, the cost of these systems are not negligible, it can reach a few thousand euros to equip a room.

1.2.3.2 Biomechanical model

Based on motion capture systems, a multibody mechanical model of the human body is constructed. Rigid segments are connected together with various joint combinations. This is called an osteoarticular model. Using a joint coordinate system, anatomical positions and orientations of the segments in space are estimated. As illustrated in figure 1.13, the anatomical points and the coordinate systems are extracted from the bone structures.

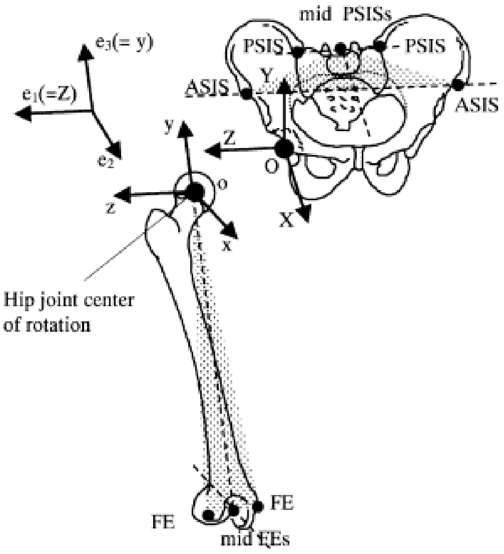

Figure 1.13 – Right hip joint coordinate system based on pelvis and femoral coordinate systems [31, 32].

The model generation consists in minimizing the difference between a motion capture system marker set and the osteoarticular model virtual marker set. Lu et al. [33] present a bone position estimation based on global optimization with joint constraints.

It consists in minimizing the function presented in eq. 1.1:

$$f(\xi) = [P - P'(\xi)]^T W [P - P'(\xi)] \tag{1.1}$$

where P is the measured marker set coordinates, W a positive-definite weighting matrix, ξ a set of generalized coordinates and $P'(\xi)$ the marker set coordinates calculated (i.e., of the biomechanical model). Figure 1.14 shows a possible distribution of the motion capture system markers.

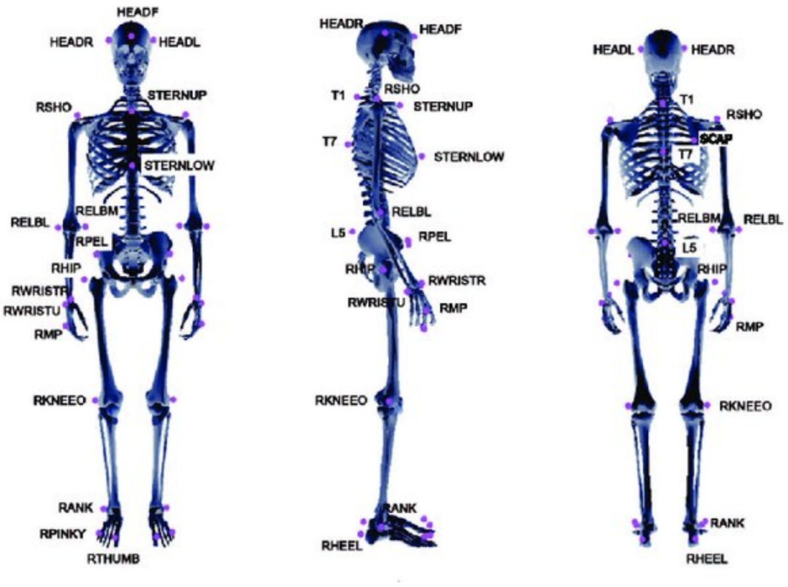

Figure 1.14 – Example of marker locations used for motion capture [34].

Therefore, segments positions and orientations in space can be monitored and data processing can be achieved. Additionnal features can be added to the model such as dynamic or muscular forces aspects.

1.2.4 Inertial measurement unit systems

The IMUs offer interesting characteristics, such as their small size and low cost. They can provide the position in the 3D space by the use of the adapted fusion algorithm [35]. IMUs are increasingly integrated into systems. They offer good accuracy with less constraints [36]. Accelerometers are micro-electromechanical systems (MEMS) that are typically in the form of a system-on-chip (SoC).

MEMS

Micro-electromechanical systems are made from mechanical elements using micro-manufacturing processes and powered by electrical sources. They are generally composed of semiconductor materials. They are most often used as sensors or actuators, they can be found everywhere, from the automotive industry to our smartphone.

1.2.4.1 IMU characteristics

Accelerometer

Accelerometers measure the global linear acceleration, composed of the sum of gravity and kinematic accelerations. The first one is oriented downwards, while the second ones is dynamic and depends on the motion. They are mainly characterized by their range, sampling frequencies, sensibilities and their measurement errors. Depending on the technologies and manufacturers these parameters differ. Nevertheless, they can be modeled by eq. 1.2a and eq. 1.2b [37]:

$$\widetilde{a(t)} = a(t) + b_a(t) + n_a(t) \tag{1.2a}$$

$$\dot{b_a} = n_{ba}(t) \tag{1.2b}$$

with $a(t)$ the current measured acceleration, $b_a(t)$ the accelerometers bias, $n_{ba}(t)$ and $n_a(t)$ the accelerometer noises.

The noise $n_a(t)$ can be modeled as an Additive White Gaussian Noise (AWGN) and the bias $b_a(t)$ as the integration of AWGNs. AWGN is characterized by a uniform distribution of the power spectral density across the frequency band and a zero-mean normal distribution in the temporal domain. Thus, obtaining the global position by integrating the accelerations is difficult as the noise and the gravity components impact the measurements.

AWGN

The additive white Gaussian noise follow the centered normal distribution. The probability density function is presented in eq 1.3:

$$f(x) = \frac{1}{\sigma\sqrt{2\pi}} e^{-\frac{1}{2}(\frac{x}{\sigma})^2} \tag{1.3}$$

with σ the standard deviation (or the noise power spectrum).

Gyroscope

Gyroscopes measure angular velocities and are also characterized by their range, sampling frequencies, sensibilities and their measurement errors. They can be modeled by eq. 1.4a and eq. 1.4b:

$$\widetilde{g(t)} = g(t) + b_g(t) + n_g(t) \tag{1.4a}$$

$$\dot{b_g} = n_{bg}(t) \tag{1.4b}$$

with $g(t)$ the current measured angular velocity, $b_g(t)$ the gyroscope bias, $n_{bg}(t)$ and $n_g(t)$ the gyroscope noises (AWGN).

Magnetometer

The magnetometer measure the magnetic field in T (Tesla). Generally in navigation system, the magnetometer is used as a compass to detect the magnetic field. This component is very sensitive. It can be heavily impacted by electromagnetic environment.

Motion capture based on IMUs

One can also found commercialized systems like Xsens[4]. As an example, the Xsens MVN suit products are based on IMUs and allows motion capture with good accuracy (Figure 1.15). Nervertheless, this kind of system may be constrained by the on-board mass of batteries and autonomy for long measurement sessions. The ergonomic aspect may be restrictive for several applications. The space requirements of such a system could

---

[4] https://www.xsens.com/

restrict or limit the user's movements. In addition, for the full system (i.e., hardware and software) the cost can reach few thousand euros.

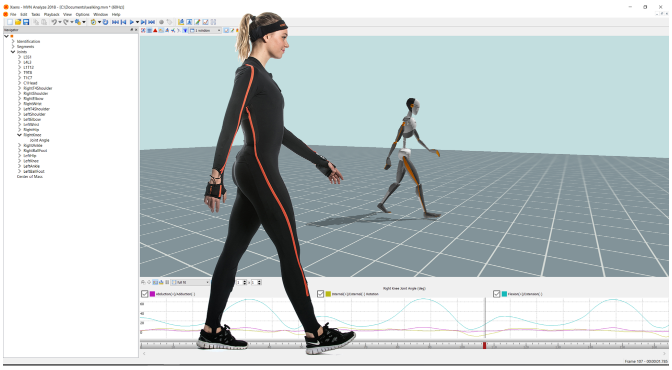

Figure 1.15 – Xsens MVN Link suit with Xsens MVN Animate software [38].

1.2.5 Complementary systems : Electromyography sensors, force platform and pressure sensors

Other systems allow the analysis of human movements. We find force platforms or pressure sensors [39], which allow to investigate the effort interactions between the human and his environment. The electromyography sensors (EMG) allow to detect the activity of the muscles by measuring small electrical signals generated during muscle contractions. These systems can be used in a complementary way to add reliable information on motion analysis.

1.3 Human activity recognition

Classification or recognition consists in qualifying by labels an individual from a set of given characteristics called features. For example, a car have different features such as its color, maximum speed, tire sizes etc. Using these different information allows us to discriminate the different individuals called classes of a group. In motion analysis, classification can be used to qualify the different performed activities. For example one can evaluate the number of passes or jumps in volleyball. To go further, after performing classification, additionnal processing can be used to quantify the performed activity. HAR based algorithms can classify the different performed activities using various methods. The algorithms take as input structured or unstrutured data and determine as outputs boundaries containing each activities or classes. The general existing methods are presented in this section.

Supervised learning

Generally, supervised learning is employed to train the classifier models. This require to label the input data according to its class. The most adapted classification method depends on the application, data type, format, and size. Among the widely used classification methods we found the supervised learning. It consists in predicting the output Y from the observation input X. Let denote the observation list as follows $\{(x_1, y_1), (x_2, y_2), ..., (x_N, y_N)\}$ with N the number of training sample, x_i the feature vector of the i-th observation and y_i the corresponding class or label. For example, the feature vector can correspond to the characteristics of an acceleration signal (i.e., maximum, minimum, average, standard deviation...) during a given time period. An activity or event is associated with this observation that will be used to train the classifier. We defined the function $h : X \rightarrow Y$ as an element of the hypothesis space H with X the input space (i.e., the feature space) and Y the output space (i.e., the label space). Supervised algorithm try to minimize the risk function R defined by $R(g) = \frac{1}{N}\sum_i L(y_i, g(x_i))$ with the loss function $L : Y \times Y \rightarrow \mathbf{R}^{\geqslant 0}$.

Among the different supervised classification algorithm we mainly found the decision tree, the Naives Bayes, the k-Nearest Neighboor (k-NN), the Hidden Markov Model (HMM), the Support Vector Machine (SVM) and neural network based algorithms [40] (Figure 1.16). Each algorithm offers different properties adapted or not to the desired application. As support vector machines and neural networks are the most prominent, we decided to add more details on their working principle.

Support vector machine

Decision parameters such as learning speed or tolerance to parity problems influence the choice of classification models. Nevertheless, the accuracy of the models is the most important. SVM models are generally more efficient than other models such as k-NN or HMM. Sen et al.[41] present the comparison between different classification algorithms. SVM shows the best result in term of overall accuracy. Abdullah et al.[42] show that SVM mainly outperformed other models in term of overall accuracy in some selected field of research.

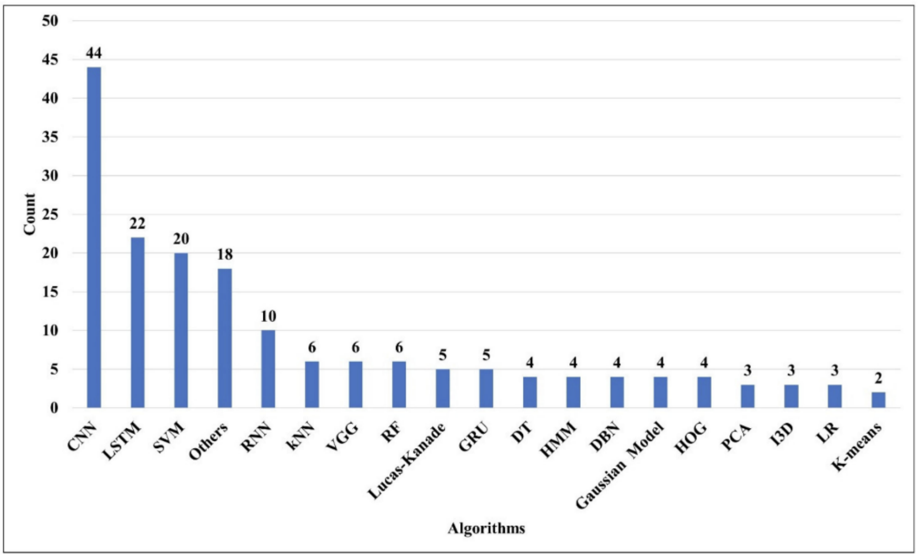

Figure 1.16 – Repartition of HAR algorithm used in literature. 95 articles were selected from Jan 2018 to May 2022 [40]. CNN: Convolutional neural network; LSTM: Long short-term memory; RNN: Recurrent neural network; VGG: Visual geometry group; RF: Random forest; GRU: Gated recurrent unit; DT: Decision Tree; DBN: Deep belief network; HOG: Histogram of oriented gradients; PCA: Principal component analysis; I3D: Inflated-3D; LR: Logistic regression.

SVM consists in minimizing a function $f(w,b) = \left[\frac{1}{N}\sum_{i=1}^{N} max(0, 1 - y_i(w^\top x_i - b))\right] + \lambda \left\|w\right\|^2$, with x_i the feature vector of the i-th observation, y_i the corresponding class or label, N the number of sample, λ, w and b the SVM model hyperparameters. The principle is based on the construction of an hyperplane maximizing the margin between the classes (Figure 1.17). In addition, SVM models allow nonlinear classification using the kernel trick. It consists in mapping the data in a higher dimensional space. Bhavsar et al. [43] present some basic kernel function such as linear kernel, polynomial kernel and radial basis function (RBF) kernel. Properties of kernels are discussed and highlight the limitations such as the need of developing methods for determining the optimal design.

Artificial neural network

Neural networks are very popular and can also be used for classification purposes. The principle is based on the use of a structure composed of artificial neurons linked by connections called synapse. Weights and biases are associated to each element (Figure 1.18).

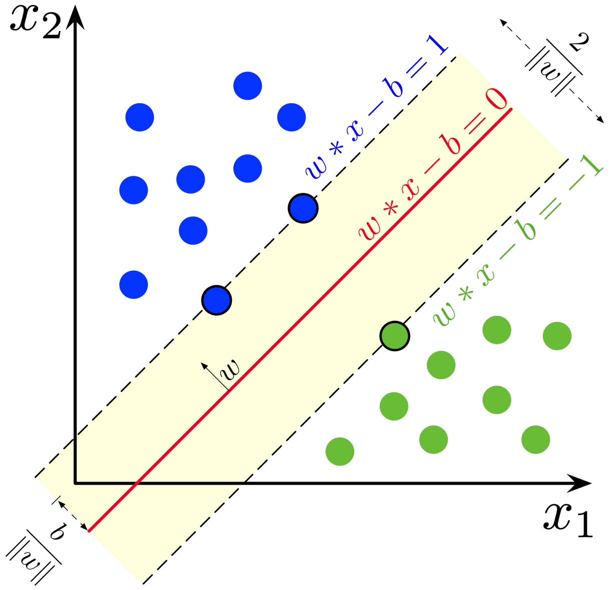

Figure 1.17 – Illustration of the SVM hyperplane for classes separation [44].

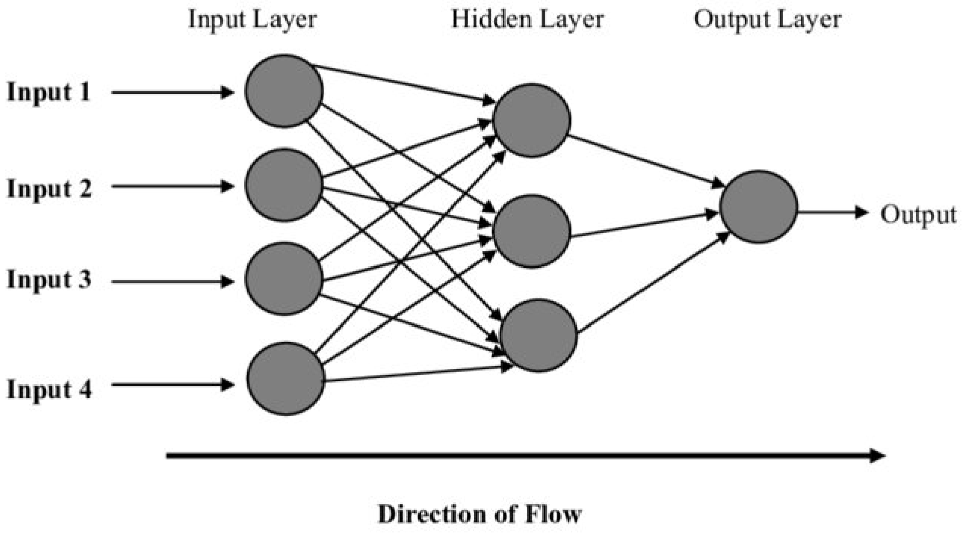

Figure 1.18 – Structure of feed forward ANN [45].

Each connected neuron k can be described by the following function $n_k = f(\sum_{i=1}^{N} w_i x_i + b_k)$ with N the number of input connections, x_i the inputs, b a bias and w_i the connection (synapse) weights. The function f is called activation function and represent how the neuron is activated. Sharma et al. [46] present various activation function used in deep learning field.

Deep learning

A recent work presents the definition of deep learning [47]. Thus, deep learning can be described as the process that establishes the relationship between two or more variables with the knowledge that governs and gives meaning to that relationship.

One of the most typical functions are the linear activation function, the sigmoid activation function, the hyperbolic tangent and the ReLU (rectified linear unit) activation function. The choice of the activation function is not trivial, it depends on the context. For example, in binary classification problems, the sigmoid activation function is widely used [48]. In addition, the number of neuron and the number of hidden layer must be determined. Various neural network structure exist in the literature. The most popular for classification problems are the convolutional neural network (CNN) and the long-short term memory (LSTM). The multilayer perceptron (MLP) can also be found for classification purposes.

1.4 Energy aspects

Wearable sensors offer new solutions for monitoring human parameters. Sensors integrated into accessories are becoming more common. Nevertheless, these embedded systems are facing some challenges: they need power supply to operate. The next sections present the common approaches to power supplied systems and the harvesting techniques.

1.4.1 Energy saving strategies

The development of new technologies has led to the design of less energy consuming systems. This limits the amount of energy storage to be embedded in autonomous systems. In order to have more integrated and ergonomic systems, operating strategies are investigated. Casamassima et al. [49] have investigated a power management layer that improves battery life by up to a factor of 5. Based on an activity recognition application, their approach consists in adapting the operating point of the sensors based on the user's activity. Gao et al. [50] proposed a power management system without batteries based on mechanical, thermoelectric and photovoltaic harvesters. Their power management circuit operates at ultra-low current and voltage (< 60 mV).

1.4.2 Batteries

Electrochemical batteries are the primary choice for meeting electrical energy needs. They provide good performance. Indeed, innovational materials and technologies like the most used lithium-ion batteries provide good characteristics such as the energy density (120-750 Wh.L^{-1}) [51]. Depending on the use, the battery life can reach a few hours. Despite the attractiveness of this type of energy storage, some drawbacks cannot be overlooked. The charging time can reach few hours and impact the application feasibility as it is necessary to extract and recharge the battery for the most integrated system. Moreover, batteries lifespan is not endless. The number of charging cycle of lithium-ion and zinc bromine batteries can reach respectively 5000 and 2000 cycles [51] but can be sufficient for the system lifespan. The life cycle analysis of these components highlights the environmental impacts and the need for a recycling process [52].

Life cycle analysis

The life cycle analysis (LCA) deals with the evaluation of the environmental impacts related to all phases of the life cycle of a product. The analysis is carried out from the extraction of the necessary materials through the manufacturing and use phases to the end of life. The 14000 series of the international organization for standardization (ISO) give the procedures to perform the LCA.

In addition, the use of single-use or replaceable batteries is widespread. Movesense[5] (Suunto, Helsinki, Finland) offers compact wearable sensors for medical and sports applications powered by a CR 2025 battery (Figure 1.19). This solution provides good compactity and energy density but requires periodic replacement (depending on the application)

---

[5] www.movesense.com

and can generate a large amount of waste. The presence of toxic heavy metals highlights the need to assess the polluting potential to reduce possible negative impacts. Moreno-Merino et al. [53] present a comparison assessment of button cells according to an energy-normalized polluting potential index. The results show in part that there is a margin for improvement in the reduction of environmental impacts by acting on the compositions of the materials.

Figure 1.19 – Movesense Medical sensor [54].

1.4.3 Energy harvesting

Studies present the different types of energy sources in the human environment for multi-source harvesting systems [6]. Among the different energy sources, there mainly are thermal energy, chemical energy, radio frequency energy, solar energy, and mechanical energy (Figure 1.20). Mechanical energy sources are dominant on the human body, the available power can be higher than 60 W due to body motions. Thermal energy harvesting depends on many parameters such as the ambient temperature or natural convection, available body heat power is less than 5 W. Thus, energy harvesting can also be a relevant solution to power wearable sensors.

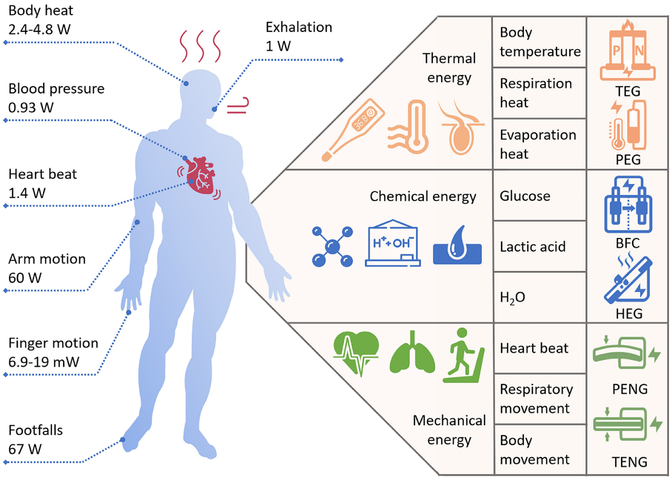

Figure 1.20 – Available energy sources on human body [55].

1.4.3.1 Piezoelectric generator

1.4.3.2 Working principle

The piezoelectric generators are based on the property of a material to generate electricity upon mechanical deformation. Linear piezoelectricity is modeled as an augmentation of elasticity and dielectric behavior according to two governing equations linking stress T, strain S, electric field E, charge density D, elastic flexibility s, permittivity ϵ, and piezoelectric coefficient d:

$$\{S\} = \left[s^E\right]\{T\} + \left[d^t\right]\{E\} \tag{1.5}$$
$$\{D\} = [d]\{T\} + \left[\varepsilon^T\right]\{E\} \tag{1.6}$$

1.4.3.3 Human application

This technology is widely used and many application exist. Among the different operating mode, we found the transverse mode (d_{33}), the longitudinal mode (d_{31}) and the piezotronic mode. Figure 1.21 presents two operating mode. Piezoelectric material can reach a peak power of 120 mW for a 2.2 cm^3 transducer volume [56]. Brenes et al. [57] developed piezoelectric and electrostatic mechanical systems. They proposed an electromechanical modeling of piezoelectric transducers and developed an electrical circuit to optimize the transducer output power flow. Piezotronic modes are becoming more and more common, Poulin-Vittrant G. et al. [58] developed on ZnO nanowire-based piezoelectric nanogenerator (Figure 1.22). The nanowire growth is obtained using a galvanic cell between aluminum and a conductive cathode surface. This solution is interesting as it is not based on heavy metals such as lead. Another example is presented in Figure 1.23. A cantilevered piezoelectric energy harvester operating in longitudinal mode is located on the hand.

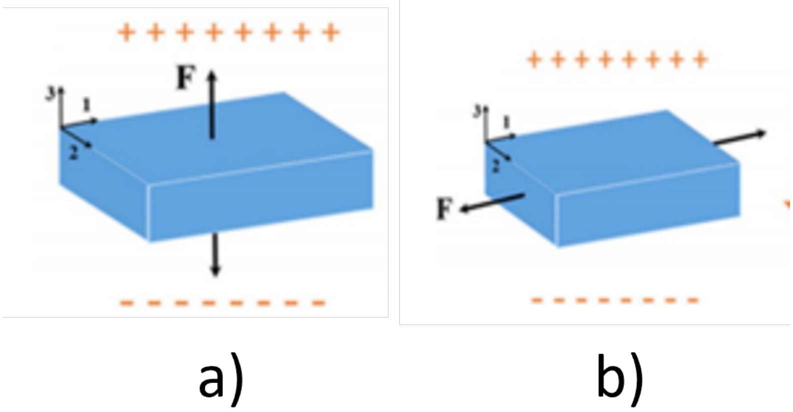

Figure 1.21 – Piezoelectric energy harvester operating modes. a) Transverse mode b) longitudinal mode [7].

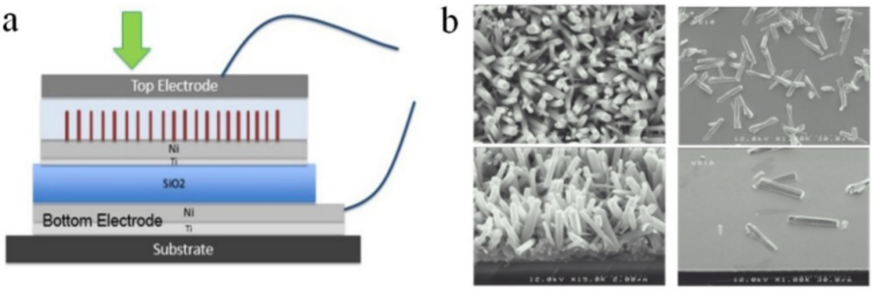

Figure 1.22 – ZnO nanowire-polymer composite [58]. a) Structure schematic b) scanning electron microscope images

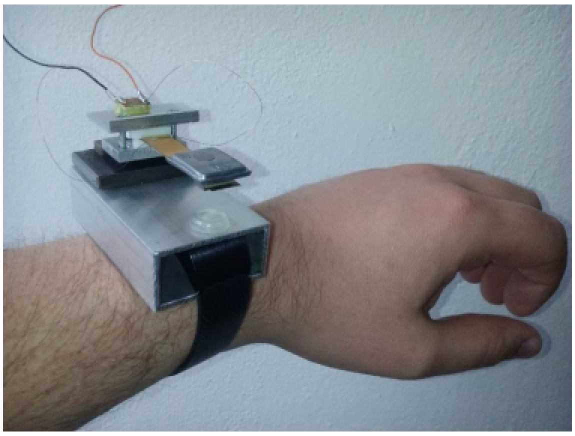

Figure 1.23 – Piezoelectric energy harvester for the hand motion [8].

1.4.4 Triboelectric generator

1.4.4.1 Working principle

The triboelectric generator is based on two major phenomena: electrification by contact and charge transfer by induction. During the contact of two different materials with dissimilar polarities, a creation of opposite charges on each side of the surfaces takes place due to the triboelectric effect. Connecting both surfaces through electrodes and repeating movement between both material produce a charge flow. The Figure 1.24 presents basics operational modes of triboelectric generators. We mainly found sliding and compressing structures.

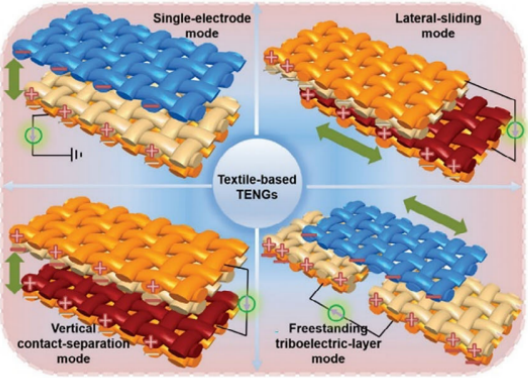

Figure 1.24 – Different basic operational modes of textile-based triboelectric generator [59].

In the general case, the produced voltage can be expressed by eq. 1.7.

$$V = -\frac{Q}{C} + V_{OC} \tag{1.7}$$

with V the voltage between the two electrodes, Q the amount of transferred charged between the two electrodes, C the total capacitance and V_{OC} the open-circuit voltage between the two electrodes. The expression of Q depends on the operating mode, one can found the various expression in [59].

1.4.4.2 Human application

Khalid et al. [7] present a comparison between various energy harvesting systems, the triboelectric generator can produce up to 4.67 mW and 392 V in open circuit with skin attached generator for exploiting human motion. The Figure 1.25 present a triboelectric generator integrated in a textile and operated by friction between the fabrics of the underneath arm and sleeve.

Figure 1.25 – Triboelectric generator integrated in textile [7].

1.4.5 Thermoelectric generator

1.4.5.1 Working principle

The thermoelectric generator is based on the Seebeck effect.

The Seebeck effect

The Seebeck effect is a thermoelectric effect. It is defined by the electric potential difference at the junction between two materials when they are subjected to a thermal potential difference.

It consists in using two connected dissimilar thermoelectric materials, the first material is an n-type (negative charges) and the second a p-type (positive charge) semiconductor. A classical model is the following equation (eq. 1.8):

$$J = -\sigma S \nabla T \tag{1.8}$$

with J the current magnitude, σ the electrical conductivity, S the Seebeck coefficient and ∇T the temperature gradient.

1.4.5.2 Human application

Hyland et al. [60] developed a thermoelectric generator that can produce up to 20 $\mu W.cm^{-2}$ on the upper arm at walking speed. The Figure 1.26 presents the developed thermoelectric generator taped directly to the skin.

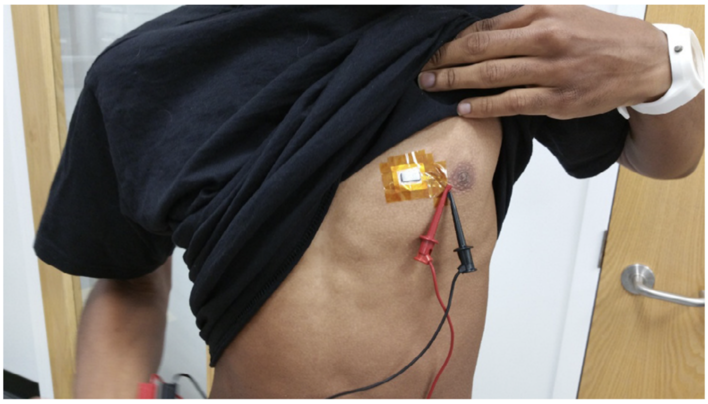

Figure 1.26 – Thermoelectric generator placed on the chest area [60].

Nevertheless, drawbacks like toxicity of the materials, mass of the system or ergonomic comfort limit its use [61].

1.4.6 Solar and radio frequency energy harvester

1.4.6.1 Working principle

Harvesting energy from solar radiation can be done by the use of photovoltaic (PV) cell. The Figure 1.27 illustrates the basic of working principle of PV.

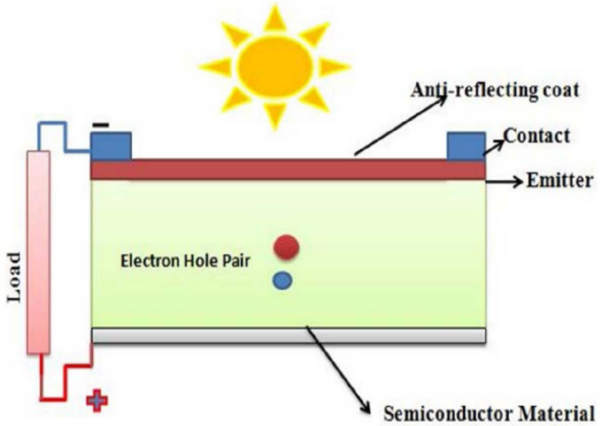

Figure 1.27 – Global overview of photovoltaic cell working principle [62].

The PV cell is based on semiconducting materials built into a p-n junction. The solar radiations are absorbed by the PV cell and the materials electrons are excited producing an electrical field and a charge flow [62].

The radio frequency harvesting technique consists in adapting an electronic circuit to collect power from some frequency bands. The Figure 1.28 illustrates the general operation.

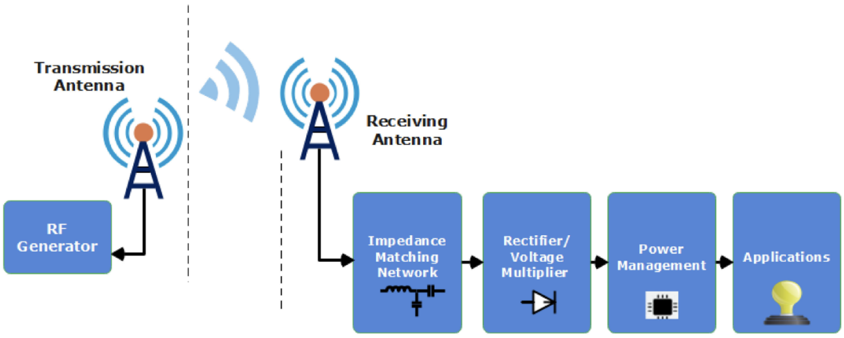

Figure 1.28 – Radio frequency energy harvesting principle [63].

In the far field, the obtained power P_r can be written as presented in eq. 1.9:

$$P_r = P_t G_t G_r (\frac{\lambda}{4\pi d_{rt}})^2 \tag{1.9}$$

where P_t is the power of the transmitted radio frequency signal, G_t is the linear transmitter gain, G_r is the sequential receiver gain and λ the wavelength.

Nevertheless, solar and radio frequency energy generators are highly dependent on the environment in which the activities are performed. Their production is not always certain.

1.4.6.2 Human application

Jokic et al. [64] developed a flexible solar energy harvester for long term monitoring. Preliminary results show an harvesting power of 16 mW in outdoor condition and 0.21 mW in indoor condition. The Figure 1.29 presents the developed system worn on a human wrist.

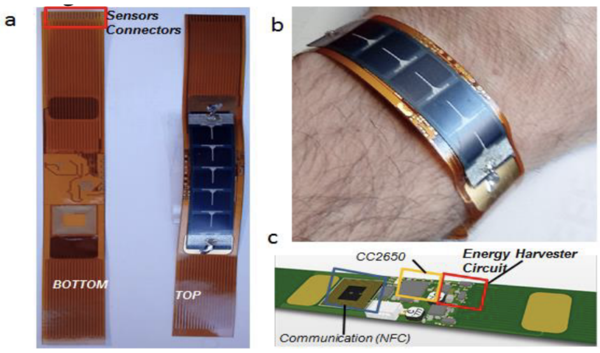

Figure 1.29 – Flexible solar energy harvester [64].

Radio frequency harvesting can be performed form different sources. We found smart monitoring or smart health application [63]. Vital et al. [65] developed a textile based RF-power harvester. They were able to harvest a DC-power of 600 μW at 10 cm from a boosted-Wi-Fi radio. Figure 1.30 presents the system integrated into a jacket.

1.5 Complex system: Optimization aspects

The optimal design of an autonomous HAR system depends on many parameters that can be difficult to tune. Indeed, the intrinsic characteristics of the HAR algorithms or

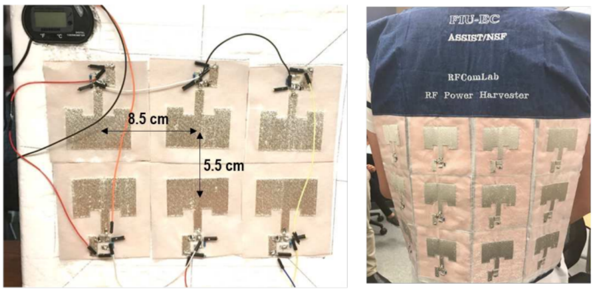

Figure 1.30 – Textile integrated patch antennas for RF harvesting [65].

the configuration of the sensors associated with their energy consumption lead to a dozen customizable parameters. The table 1.1 presents some of the customizable parameters.

Table 1.1 – HAR system customizable parameters.

	Customizable parameters
HAR	Training dataset Data segmentation Algorithm/Method
Sensors configuration	Sampling frequencies On-body locations Sensor type (accelerometer, gyroscope, magnetometer) Number of axes

Thus, the design of a wearable activity recognition system can be categorized as a complex system.

Complex system

Complex system can be defined in different ways [66]. In general, it is characterized by a large number of elements that exchange and interact with each other. The individual behavior of each element is not enough to characterize the properties of the system. Thus, it is necessary to consider the various degree of organization of these elements.

1.5.1 Concept of numerical optimization

Because of the different levels of interaction and the heterogeneous behaviors of the different entities, the best solution is not easily obtained. Nevertheless, engineering tools coming from applied mathematics can help us approach more easily the best or the so-called optimal solution: the numerical optimization methods.

The Figure 1.31 presents the general structure of an optimization process.

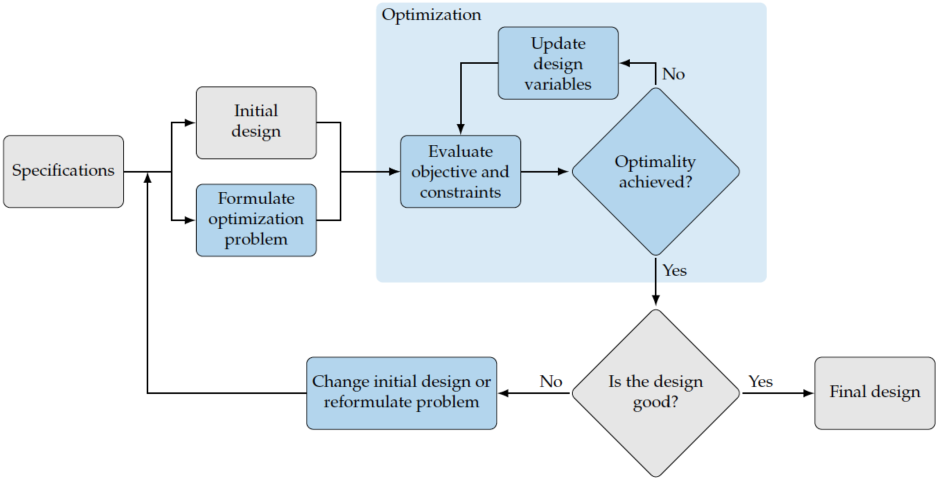

Figure 1.31 – Structure of optimization process [67].

The main features are the formulation of the problem and the specifications. First, the variables are initialized with starting points, and then, through an iterative process, the objectives are evaluated to obtain the best solutions.

For example, the Figure 1.32 illustrates the determination of an objective function optimum by the use of a gradient algorithm. The aim is to determine the minimum of the function $f(x)$. The problem can be expressed as $\underset{x=(x1,x2)}{argmin}\ f(x)$. To reach the optimum point x^* from the starting point x_0 four iterations were used. However, the exact solution is not always precisely obtained and it can take a lot of iterations to reach it. Thus, a stopping criterion has been introduced. It is defined for example by a maximum number of iterations or a minimum tolerance in the value difference of the last two solutions. In addition, the determination of the minimum number of iteration can be tedious if the objective function evaluations are numerically cumbersome.

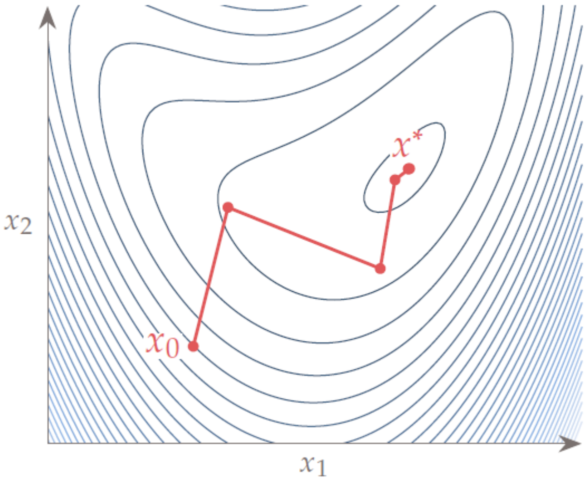

Figure 1.32 – Optimization method based on gradient [67]. x_0 is the starting point and x^* the optimum of the objective function.

1.5.2 Optimization algorithm choice

In order to perform optimization, it is first necessary to determine the optimization problem class according to the problem characteristics. Figure 1.33 presents an overview of the two main optimization aspects: problem-based and objective and constraint characteristics-based formulations. Depending on the attributes, the adapted optimization method varies. As illustrated in previous Figure 1.32, gradient-based methods rely on directional derivatives. Considering the example of a convex function, common gradient-based method, such as gradient descent, can solve unconstrained optimization problems with continuous design variables. This method assumes objective functions to be C^1. The gradient of a function f is obtained by:

$$\nabla f(x) = \left[\frac{\partial f}{\partial x_1}, \frac{\partial f}{\partial x_2}, ..., \frac{\partial f}{\partial x_n}\right] \tag{1.10}$$

with $x = [x_1, x_2, ..., x_n]$ the vector of design variables.

To determine the optimum (minimum), the following iterative process is computed:

$$x_{k+1} = x_k + \alpha p_k \tag{1.11}$$

$$p_k = -\frac{\nabla f_k}{\|\nabla f_k\|} \tag{1.12}$$

where x_k are the design variables, α is a positive constant which represents how far each iteration step goes in the direction p_k, p_k is the search direction method (here, the gradient descent).

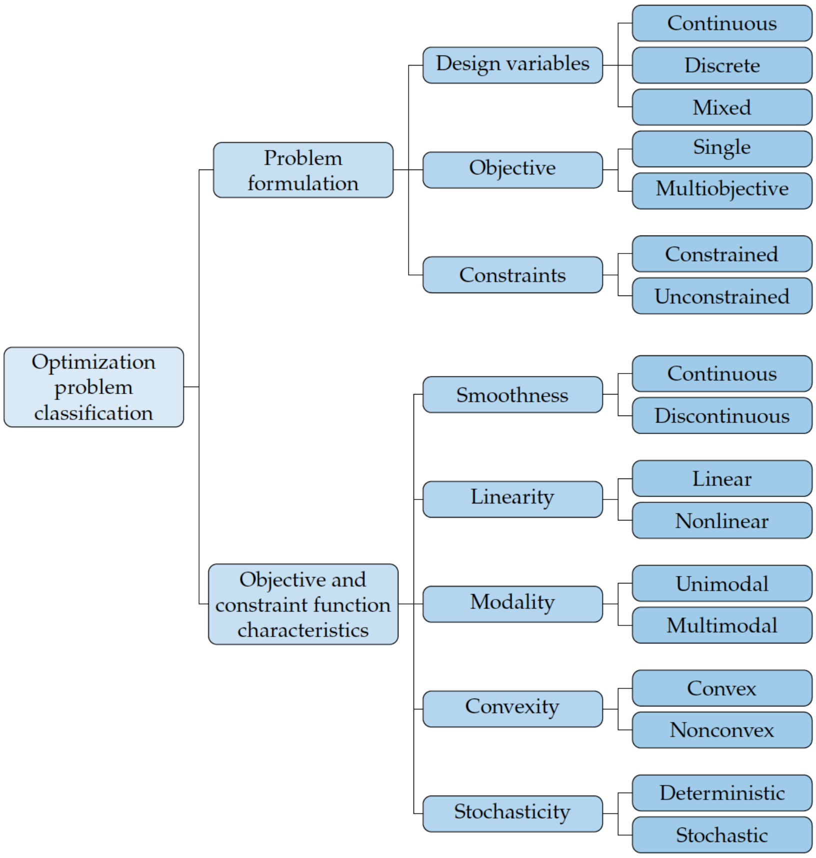

Figure 1.33 – Optimization problem classification attributes [67].

Other optimization methods based on gradient-free algorithms exist. They are useful when the objective functions can not be characterized, such as 'black box' systems. In addition, they do not assume function continuity. Figure 1.34 presents some of gradient-free optimization methods.

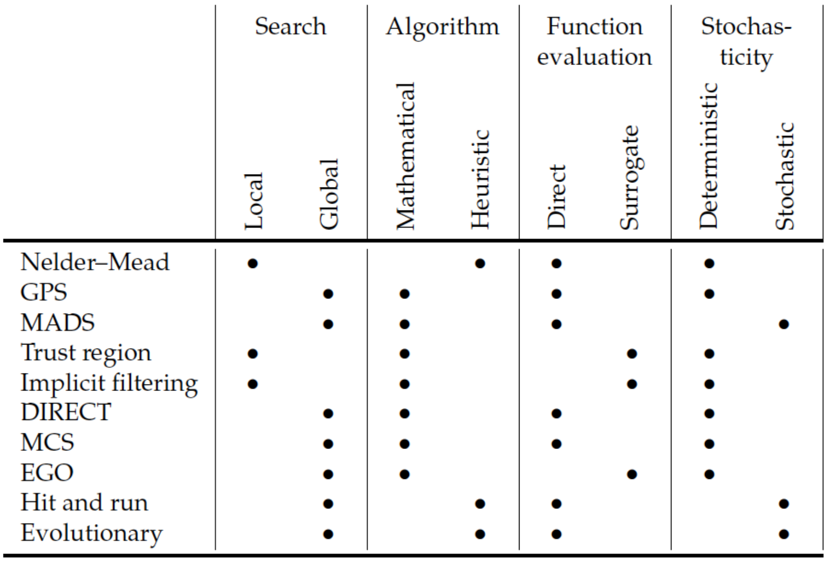

	Search		Algorithm		Function evaluation		Stochas-ticity	
	Local	Global	Mathematical	Heuristic	Direct	Surrogate	Deterministic	Stochastic
Nelder–Mead	•			•	•		•	
GPS		•	•		•		•	
MADS		•	•		•			•
Trust region	•		•			•	•	
Implicit filtering	•		•			•	•	
DIRECT		•	•		•		•	
MCS		•	•		•		•	
EGO		•	•			•	•	
Hit and run		•		•	•			•
Evolutionary		•		•	•			•

Figure 1.34 – Classification of gradient-free optimization methods [67]. GPS: generalized pattern search; MADS: mesh-adaptative direct search; DIRECT: divide a hyperrectangle; MCS: multilevel coordinate search; EGO: efficient global optimization.

1.5.3 Multi-objective optimization

It is convenient to discuss the multi-objective optimization in the case an autonomous monitoring system (objectives in power consumption and HAR accuracy for example). The problem can be characterized as nonlinear (non convex), multimodal and with discrete design variables. The system can be assimilated to a black box, therefore, the optimization is based on problem formulations. Taking into account the defined attributes, the use of heuristic methods seems relevant. Evolutionary algorithms provide good properties such as global optimum search, direct function evaluation and they are based on heuristic methods.

1.5.3.1 Genetic algorithm

Popular approach is based on the use of genetic algorithm (GA). The principle rely on the evolution of a population with individuals converging to the problem optimum solutions. Inspired by biological reproduction and evolution, the iterative process in based on selection, crossover and mutation. Figure 1.35 presents the iterative process of the GA.

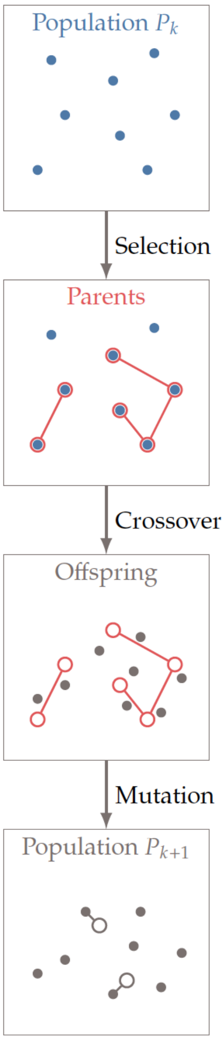

Figure 1.35 – Overview of genetic algorithm principle [67].

The starting population is first generated. Then, trough a selection process, individuals are selected as parents to build the children for the next population generation. The characteristics called chromosomes (for example the number of sensor locations, the sampling frequencies etc) of two selected individual are crossed. In addition, some individuals are selected for mutation. It means that a gene is mutated (corresponding to the modification of a chromosome value translated by a design variable value modification). Among the selection methods, one can find the widely used tournament selection process. It consists in the selection of random pairs of individuals and selecting the best one. Other selection methods exist such as the roulette wheel selection.

GA can perform multi-objective optimization, the problem can be written with the following formalism:

$$\underset{x}{argmin}\ f(x) = \begin{bmatrix} f_1(x)) \\ f_2(x)) \\ \dots \\ f_n(x)) \end{bmatrix},\ n \geqslant 2 \tag{1.13}$$

with n the number of objectives functions and f the objectives functions that depends on the parameters x to be optimized. Trade-offs between the objectives are established as it is difficult to satisfy independently each objective (dependence between the objectives). Thus, it is common to use the Pareto front [68] which builds the optimal frontier highlighting the trade-offs between each objectives. Hence, an algorithm developed by Deb et al. [69] called NSGA-II (Non-dominated Sorting Genetic Algorithm) coupling these 2 aspects of multi-objective optimization was born. As an example, the Figure 1.36 illustrates the Pareto front from computed solutions. To obtain the Pareto front, first 1) a non-dominated sorting is performed, then 2) a crowding distance sorting is performed. The non-dominated points correspond to the Pareto optimal. To compute non-dominated sorting, one can use Deb et al. [69] algorithm. The crowding distance sorting is used to evaluate the front spread to keep diversity in the solutions. Crowding distance can be computed using the Manhatten Distance or L1 distance.

1.5.3.2 Particle swarm optimization

One can find other optimization methods based on evolutionary algorithms, for example particle swarm optimization [70] (PSO) based on collaboration between individuals

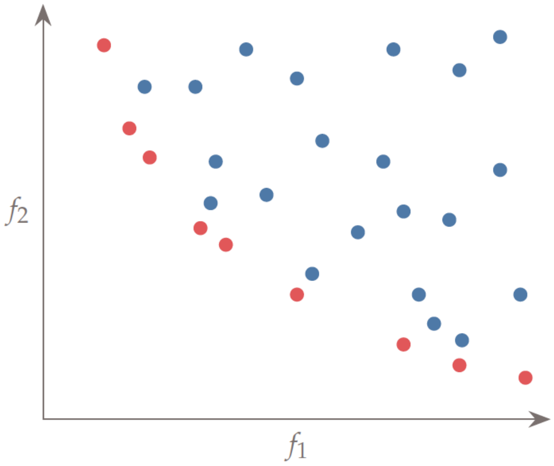

Figure 1.36 – Illustration of objectives functions evaluations (dots) and the Pareto front (red dots) [67]. f_1 and f_2 are objectives functions.

or ant colony optimization [71] (ACO) based on ants behaviour. The PSO consists in moving the individuals (particles) according to a velocity in a n-dimensional space by an iterative process [67]. Interactions between the particles lead to the determination of the best solution. Initially, the position of the particle are distributed randomly in the searching space. The position of a particle i for iteration $k+1$ is obtained in equation 1.14.

$$x_{k+1}^{(i)} = x_k^{(i)} + v_{k+1}^{(i)} \Delta t \tag{1.14}$$

Where Δt is a constant time step and $v_{k+1}^{(i)}$ the velocity of the particle i at iteration $k+1$. The velocity is obtained using equation 1.15.

$$v_{k+1}^{(i)} = \alpha v_k^{(i)} + \beta \frac{x_{best}^{(i)} - x_k^{(i)}}{\Delta t} + \gamma \frac{x_{best} - x_k^{(i)}}{\Delta t} \tag{1.15}$$

Where α is the inertia parameter, β the memory parameter, γ the social parameter, $x_{best}^{(i)}$ the best position found the particle (i) and x_{best} the best position found by the entire swarm. All these parameters act on the speed of convergence and on the influence of the best positions found by a particle and the swarm. The parameters β and γ are obtained randomly in order to introduce stochasticity in the algorithm resolution process. Figure 1.37 present the PSO components in a two-dimensional case.

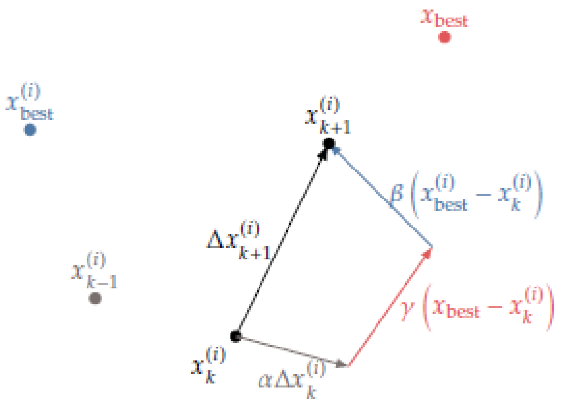

Figure 1.37 – Components of the PSO in a two-dimensional case [67]. The graph is obtained by multiplying eq. 1.14 by Δt.

One can observe how the best solutions found by the swarm and particle i influence the next position $x^{(i)}_{k+1}$.

1.5.4 Optimization applications for HAR and energy harvesters

Literature provides various optimization applications in numerous disciplinary fields. Problem can be formulated in different ways with different constraints. For example, Khaled et al. [72] investigate the influence of the shape of a cantilevered piezoelectric harvester using genetic algorithm optimization. They used the cantilever length, width, the active material thickness and the base material thickness as design variables. The optimization problem was constrained by the stress and frequency. The objective is to maximize the output power. Zhang et al. [4] investigated optimal SVM parameters using PSO to obtain the highest HAR accuracy. Results show better performance in accuracy and also in operating time for decision-making when using PSO.

1.6 Smart cloth systems for motion analysis: inherent measurement errors

Smart cloth can be seen as the interface between textile materials and technology. Progress in the different science fields led to the design of new multidisciplinary systems [73]. As an example, conductive yarns [74] enhance integration capabilities of wearable technologies in a garment, it offers more comfort and flexibility. Smart workwear systems allowing ergonomic risk assessment are emerging and are commercialized. Wergonic AB, Stockholm, Sweden (wergonic.se) offers a solution to monitor the ergonomic risk using a cloth with embedded sensors. Sensors are placed into pockets at three locations, i.e., both upper arms and the upper back. The data collection is performed using wireless communication with a smartphone, and real-time feedback is provided. However, it is appropriate to address the matter of existing errors in these smart cloths measurements, especially when motion sensors are embedded. As introduced before, IMUs are a widely used type of sensors for motion and posture applications, providing accuracy and ease of implementation [75]. Nevertheless, the information provided by IMUs depends on their placement and fixation. Cloth-embedded sensors face relative motion artefacts, which can impact the measurement quality [76, 77]. Improvements can be obtained by using tight-fitting clothing, and good agreement between skin-mounted and cloth-embedded sensors has been shown for temporal motion kinematics at C7 and T12 (anatomical location of the spine) locations [78]. Moreover, other external factors may impact the measurements, such as sensor fixation or other soft tissue artefacts like skin or muscles. Camomilla et al. [79] highlight the soft tissue artefact issue. Despite the recent improvements in motion capture methods, soft tissue artefact errors remain and impact the accuracy of the results. Thus it is necessary to consider their contribution according to the applications.

1.7 Scientific positioning of the present work

As presented before, thanks to the expansion of the wearable sensor market, the use of IMUs has been democratized and many applications have been developed. Motion recognition is very fashionable because it allows to automatically qualify and quantify the performed activities in an objective way. However, the accuracy of results based on the use of IMU depends on many parameters. The first criterion is the quality of the information measured by the IMUs which is influenced by their locations [12]. Other criteria related to the classification method bring out parameters and hyperparameters (e.g., segmentation, kernel...) to be optimized. There is currently no general method to determine the optimal positioning of these IMUs on the human body. Indeed, the literature presents several applications with different configurations. How to ensure the optimality of the result obtained? Power consumption aspects is also a valuable field of interest as some applications are conditioned by power constraints. In addition, sustainable developments and ecological stakes imply the reduction of pollutant wastes and the improvement of energy efficiency. Cantilevered piezoelectric harvester seems to be a good candidate as they are widely used. Several architectures and technologies on piezoelectric-based harvester exist in the literature [80]. Thus, this thesis aims to develop methods for determining the optimal position and configuration of IMUs and energy harvesters on the human body for HAR system design. Based on a systemic approach, weak and strong interactions between the various parameters are investigated.

Systemic approach

The systemic approach refers to the analysis and understanding of a complex system in a global perspective rather than an exhaustive study of individual elements.

In addition, it is relevant to consider optimization aspects as many parameters needs to be tuned. Thus, optimization of HAR accuracy with respect to energies aspects are conducted. Finally, measurement errors such as cloth artefacts induced by the embedding of sensors in a garment are investigated trough an ergonomic application.

The Figure 1.38 presents the general structure of the thesis. The first guideline (in blue) concerns the information sources on the human. The aim is to propose and use methods for determining the optimal IMUs location and configuration on the human body. This first guideline intersects with another one (in green), which focuses on the application aspect and system design. The last guideline deals with the energy sources on the human body to address the issues and challenges related to the autonomy of embedded systems. Each step on these lines represents the contributions made by this thesis, it shows the coupling between the various parts of the systemic analysis. Details on the scientific positioning related to this general description of this thesis are given next.

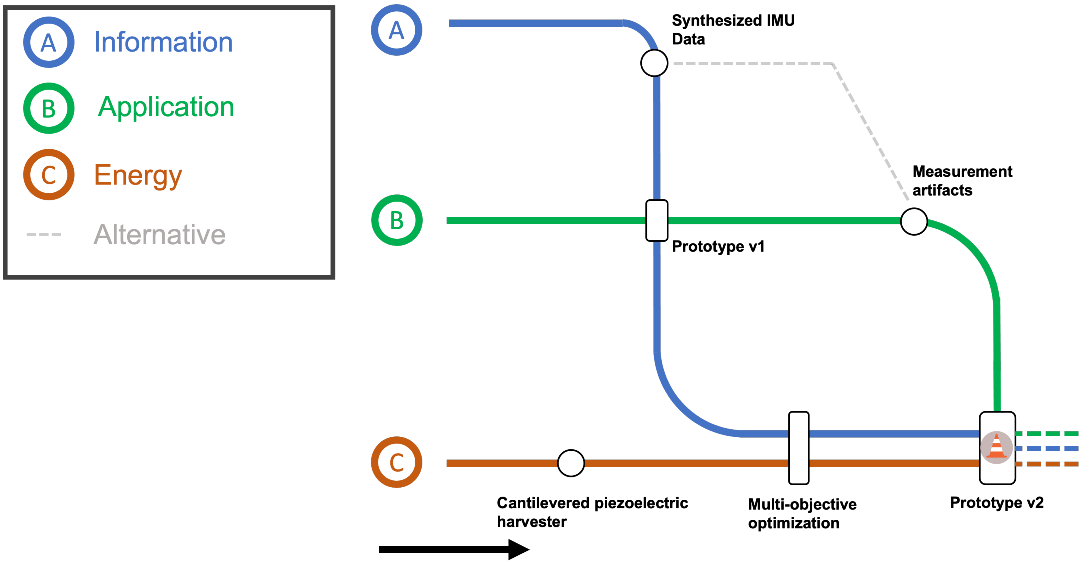

Figure 1.38 – Global presentation of the thesis.

1.7.1 Information sources on the human body: Inertial measurement unit

In the activity monitoring applications, the accuracy of the results obtained also depends on parameters such as classifier models, database, configuration of the sensors, data structuring and data quality. Thus, there is a relationship between the determination of the best positions and the choice of parameters for the HAR realization. Several studies present the classification accuracy obtained without knowing if this result is the most optimal. Of course, it may be sufficient to obtain a bounded and non-maximal result (i.e., 100 % recognition). Zhang et al. [4] proposed an HAR classification algorithms particle swarm optimization-based support vector machine (PSO-SVM). Results show 99.2 % accuracy in activity classification (10 classes) with the use of 2 accelerometers and 2 gyroscopes (located on wrist and elbow) sampled at 100 Hz. Their data were first filtered and segmented with 1 s window and 50 % overlapp and 8 common time-domain features were extracted (including mean, standard deviation, maximum, minimum, range, kurtosis, skewness, and quartile). Kautz et al. [5] proposed an HAR in beach volleyball using deep convolutional neural network. The study was based on a wrist accelerometer sampled at 32 Hz, results shows 83.2 % classification accuracy (10 classes). They extracted 39 features from event windows (based on their algorithm structure). However, the more complex the case is, the more difficult it is to obtain a good result (i.e., large number of classes, size of the database). Testing exhaustively all possible combinations of location of the human body could require an unreasonable amount of time and a too important installation. It is therefore necessary to evaluate the information sources in order to obtain an optimal placement and adjustment of these IMUs. We proposed to used data extracted from full body motion capture experiments to train HAR algorithms. The method is presented in chapter 2. Based on a biomechanical model, synthesized data are generated allowing numeric simulation on multiple sensors combinations with more ease.

Datasets

Our data are obtained by performing experiments in the M2S Laboratoty (ENS Rennes). Datasets composed of various human sport activities are created. Motion capture are conducted with the Xsens suit technology. Details are given in the next chapters.

In addition, the development of HAR algorithms can be greatly facilitated, depending on the desired application, by using the amount of data that already exists. Indeed, experiments are generally designed to highlight specific applications but online available dataset can be found. The chapter 4 (optimization) is based on an online availaible dataset. The first characteristic is the size of the database: the larger it is the more efficient the learning will be. A lack of data or a poor representation of the activities performed could lead to overfitting by the algorithms.

The balance of the dataset is also very important to be able to recognize efficiently each activity. Presence of dominant activities should limit the detection of other activities.

Finally, activities should be performed by various subjects to generalize the application to the target population. Individual characteristics such as movement execution techniques may impact the final result and must be generalized by the algorithms.

Overfitting

In machine learning, overfitting corresponds the poor generalization of the data. When overfitting occurs, data can not be reliably fitted or predicted [81].

1.7.2 Energy sources on the human body: Cantilevered piezoelectric harvester

The versatility and scalability of piezoelectric harvester allow them to be organized in various configurations to harvest energy from kinetic sources, making them good solutions to overcome the excessive use of batteries. Liu et al. [9] present a survey on the different technologies to harvest energy from human body. They show that the piezoelectric transducer is a promising candidate. De Fazio et al. [82] present a self-powered piezo-resistive smart insole based on the use of a Li-Po battery and a piezoeletric transducer. The harvesting subsystem provides the necessary energy requirement to operate the developed device. Cha et al. [83] developed a flexible piezoelectric energy harvesting from mouse click motions. They obtained a maximum harvested energy in the range of 1 - 10 nJ. The beam structure is very common and have a lot of application [84], the generator operation is based on vibrations. Li et al. [85] work on a wearable energy harvesters for human limb movement. Results show a harvested energy in the range of 0.56 - 0.69 μJ in the frequency range of 0.5 - 5 Hz. In addition, the generated output power is inherent to its localization and orientation on the human body. Izadgoshasb et al. [86] experimentally investigated the optimal orientation of a cantilevered piezoelectric harvester located on the leg of a person walking on a treadmill. Result show that the best configuration is an orientation of 70° with reference to a coordinate system attached to the leg. Nevertheless, as highlighted, it is difficult to directly measure the performance of piezoelectric harvester from human motion. The installation can limit the user movement and it is difficult to perform precise measurement without adapted devices. An alternative way to conduct the optimal orientation or position of piezoelectric harvester consists in the use of electromechanical model. Indeed, using the various existing models in the literature [87], one can predict the harvesting energy from measured acceleration data. Notwithstanding, there is no global method evaluating multiple locations and all orientations on the human body. Thus, we propose a method using measured acceleration data to evaluate the best cantilevered piezoelectric harvester configuration on the human body. The method is presented in chapter 3. Using a distributed parameters model and measured acceleration data from 17 sensors locations, the predicted energy is simulated. Characterization of acceleration data is also performed to extract qualitative and quantitative features for operating piezoelectic harvesters.

1.7.3 Optimization

The determination of the best IMUs locations for HAR applications or the best energy harvesters configurations on the human body is difficult. Indeed, as introduced before, high number of customizable parameters makes the determination of the optimal configuration challenging. Nevertheless, the implementation of engineering tools such as optimization methods allows to converge toward the optimum. Based on the chapter 2 and 3 materials, we designed two optimization problems for solving the optimal configurations. The coupling between information and energy sources is highlighted by evaluating the tradeoffs between HAR accuracy and energy consumption of an IMU sensor network. Increasing the number of IMU on the whole human body improve the HAR accuracy but increases the power consumption. Thus, it necessary to adapt the configuration of the IMU network to minimize the energy consumption while maximizing the accuracy of the HAR. In addition, the influence of the geometry of the cantilevered piezoelectric harvester is evaluated. Modification of its geometry or shape impacts its behavior and the harvested energy. Issues related to ergonomic and feasibility aspects are discussed. Hence, we proposed in chapter 4 a method based on NSGA-II for determining the best IMUs configuration according to an HAR application. Cantilevered piezoelectric harvester geometry influence on the predictable energy on the human body is evaluated, the methods used in Chapter 3 are reinvested and adapted.

1.7.4 Smart activity assessment system

In the field of ergonomics, smart workwear systems are developed and used for risk assessment of occupational activities. However, when motion sensors like IMUs are embedded, the measurement accuracy can be affected by potential cloth artefacts, which has not been assessed previously. Therefore, it is crucial to evaluate the accuracy of sensors placed in the workwear systems for research and practice use. Considering the balance of accuracy, comfort, and usability, such a system can be potentially a practical tool for ergonomic assessment for researchers and practitioners. Error compensation algorithms are investigated in the literature, previous work presented artificial intelligence-based algorithms for assessing errors between sensors in a loose garment and an optical tracking system [88]. However, in order to compensate for these potential errors in a smart workwear system, they must first be examined and quantified. Supported by the systemic approach of this thesis, it is interesting to investigate the cloth artefact issues in the design of an autonomous motion analysis system. Thus, in collaboration with Karolinska Institutet (Stockholm, Sweden), a study based on the impact of cloth artifact on IMU measurements has been conducted. To the best of our knowledge, almost no studies investigated the impact of IMU sensors embedded in cloth using pockets for measuring trunk and upper arm postures and movements. Hence, this study aimed to evaluate the performance of in-cloth sensors compared to on-skin sensors for measuring trunk and upper arm postures and movements during occupational activities. The study is presented in chapter 5 and is contextualized by an application in the field of ergonomics. Nevertheless, the results obtained can be generalized because they highlight the phenomena present in the process of cloth artifacts. In addition, design of a smart activity assessment system prototype has been conducted. The second part of the chapter 5 presents the materials and the preliminary issues that have emerged.

Chapter 2

SYNTHESIZED IMU DATA EVALUATION FOR DATA AUGMENTATION

This chapter is based on the published work entitled *Hoareau, D.; Jodin, G.; Chantal, P-A.; Bretin, S.; Prioux, J. and Razan, F.: Synthetized inertial measurement units (IMU) to evaluate the placement of wearable sensors on human body for motion recognition, The Journal of Engineering, 2022* [89] and presents an evaluation of virtual IMU data on the human body. Virtual IMU can evaluate a larger number of sensors combinations and locations on the human body for HAR application. Indeed, testing numerically multiple configurations becomes easier and offers more possibilities. Nevertheless, some aspects such as the reliability of these data need to be investigated.

2.1 Introduction

It is necessary to choose the number and location of IMUs on the human body to perform HAR. Generally, the configurations used are chosen by empirical approaches. The positioning of the IMUs is determined in accordance with the objective of keeping the external artifacts related to the soft bodies as low as possible [90, 91, 92]. Nevertheless, some works investigated the locations and the number of IMUs on the human body. N. S. Suriani et al. [93] investigated the optimal accelerometer placement for fall detection from three different body location (hip, thigh, and foot). Multiple activities were classified using k-NN and SVM models. Results show that the hip location was the best placement to classify activities and detect falls. S. Chung et al. [94] evaluated the best configuration of IMUs for HAR application. Their study was limited to four positions (left and right wrists, waist, and ankle). They extensively tested all combinations to find the better classification model accuracy. Based on a LSTM neural network, their results indicated that only 2 sensors located on right wrist and right ankle with 10 Hz sampling frequency can give reasonable performance. It is also relevant and intuitive to place the sensors on the parts of the body that are considered during the movements performed. Regardless, there is no general method to determine the best configuration. Furthermore, testing experimentally all combinations is not feasible, covering the entire human body with IMUs is too restrictive and is currently not possible. However, the use of data augmentation techniques offers the opportunity to reduce the cost and time constraints of data collection.

Data augmentation

Data augmentation techniques consist of artificially increasing the amount of data by generating new data points from existing data.

Our proposed method is based on the use of full body motion capture system. Indeed, motion capture system allow to measure human motion accurately (less than 1 mm error for optoelectronic systems [30]) and physical quantities such as accelerations and velocities can be extracted. The aim is to generate virtual IMU data called synthesized IMU data (SID) which is not based on direct measure from a biomechanical model. Extracted SID can then be used for training HAR algorithm and testing multiple configurations. The best candidates can then be evaluated with real IMUs. Nevertheless, these data were processed and some features may have been altered such as the frequency spectrum. Thus, the information provided by the signals may differ from the measurements of the actual sensor signals. In this study, soft tissues artifacts are not considered and the biomechanical model obtained from the motion capture is composed of rigid segments.

The first part presents SID on the whole human body based on a biomechanical model. SID are generated using the Xsens motion capture system. Then, to assess the viability of SID, a comparison with real IMU data (RID) is conducted, based on statistical and frequency approaches. Finally, a HAR application is implemented and performance of SID is illustrated.

2.2 Materials and Methods

2.2.1 Experiment design: Case study

Motion capture acquisition is performed with the Xsens motion capture suit (composed of 17 IMUs sampled at 240 Hz) and the Delsys IMUs set (14 IMUs sampled at 370 Hz). Data measured by the Xsens IMUs are used to generate a biomechanical model, synthesized data are then extracted from the model to be compare to the real data obtained from the Delsys IMU measurements. During the experiment, one participant with amateur level performed 10 repetitions of 3 types of activities:

- Countermovement vertical jump: The subject jumps on the spot trying to go as high as possible, the movement starts with a squat.
- Left-side sprint: The subject starts from a static standing position; at the start, he performs a sprint with great acceleration in the left lateral direction from his initial position.
- Right-side sprint: The subject starts from a static standing position; at the start, he performs a sprint with great acceleration in the right lateral direction of his initial position.

The final database is therefore composed of 30 trials. Both measurement systems are worn at the same time by the participant (Figure 2.1). The Delsys IMUs are located on hands, lower arms, upper arms, feet, lower legs, upper legs, pelvis and sternum. We used double sided tape to fix the sensors on the body and add extra white stripes to ensure the fixations. This system is used to measure real physical quantities called real IMU data

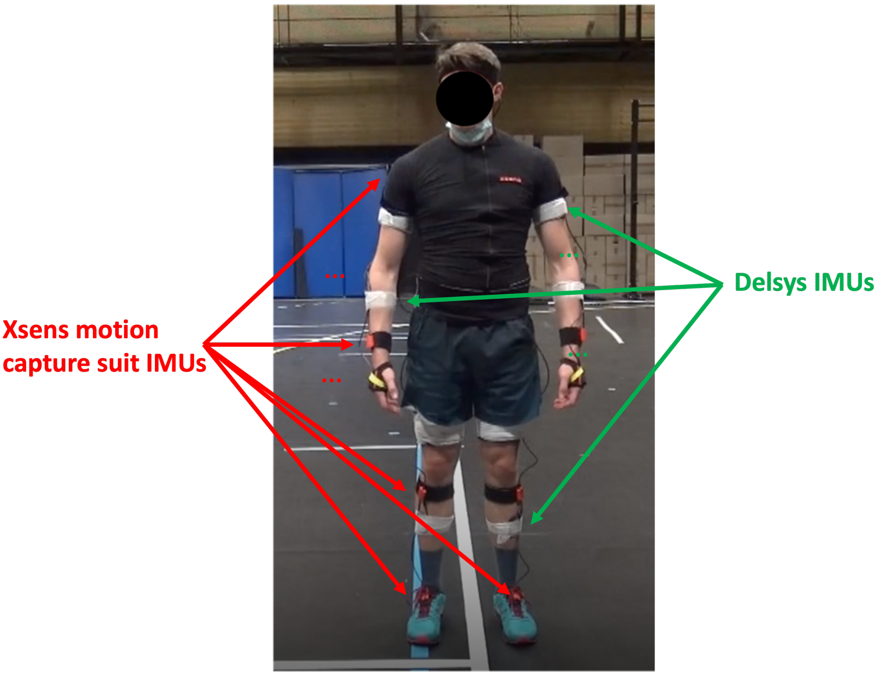

Figure 2.1 – Participant equipped with the Xsens system (IMUs in orange cases) and Delsys IMUs (under the white stripes).

(RID). The Xsens IMUs are fixed on the body thanks to self-gripping bands and the list of sensor locations is presented in Figure 2.2.

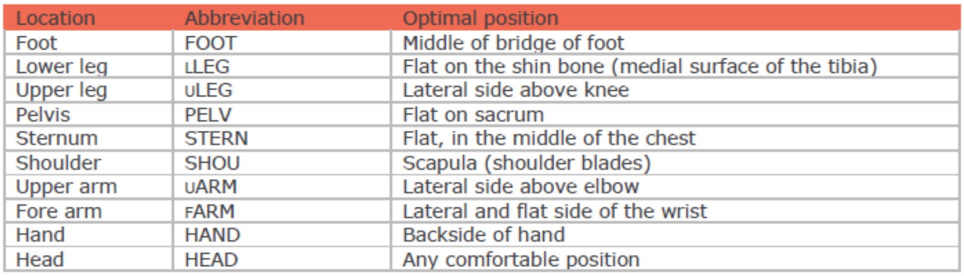

Location	Abbreviation	Optimal position
Foot	FOOT	Middle of bridge of foot
Lower leg	LLEG	Flat on the shin bone (medial surface of the tibia)
Upper leg	uLEG	Lateral side above knee
Pelvis	PELV	Flat on sacrum
Sternum	STERN	Flat, in the middle of the chest
Shoulder	SHOU	Scapula (shoulder blades)
Upper arm	uARM	Lateral side above elbow
Fore arm	FARM	Lateral and flat side of the wrist
Hand	HAND	Backside of hand
Head	HEAD	Any comfortable position

Figure 2.2 – Xsens sensor location. Extracted from the Xsens user manual.

Optimal positioning advice is given by Xsens to limit the influence of soft bodies artifacts like skin or flesh. These data are then processed by the Xsens MVN Animate software. Proprietary fusion and reconstruction algorithms allow for generating accurate numerical avatar motions at 240 frames per seconds. The model is composed of 23 rigid segments and 22 kinematic joints of 6 degrees of freedom. The Figure 2.3 shows a partial view of the global and local coordinates of the calculated joint angles.

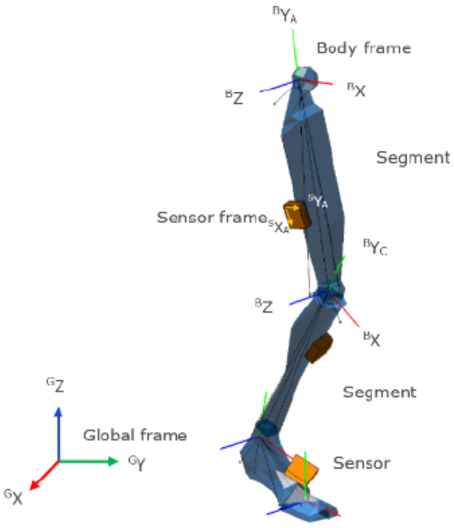

Figure 2.3 – Global and local coordinates of joint angles. Extracted from the Xsens user manual.

Once the biomechanical model is created, it is exported from the Xsens environment to be analysed and processed under CusToM (Customizable Toolbox for Musculoskeletal simulation) [95] developed by a local research team. The data extracted from the model is called synthesized IMU data (SID).

2.2.2 Custom library

The CusToM toolbox allows to visualize and analyze human motions from joint coordinates to muscle forces. An overview of CusToM functionalities are presented in Figure 2.4.

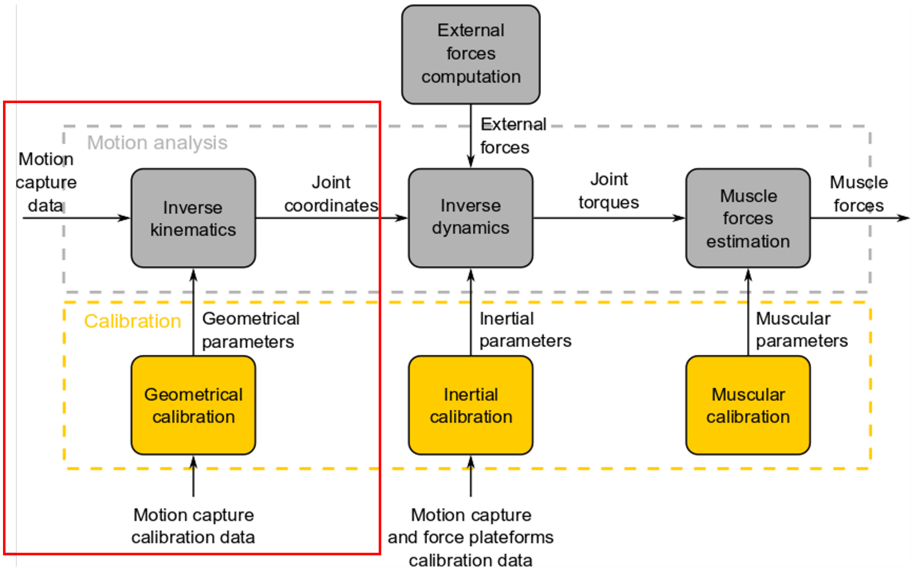

Figure 2.4 – CusToM pipeline [95]. In red the current study limitations.

Our study focuses on the inverse kinematics block. Motion analysis from joint coordinates is computed but, in order to have a better evaluation of the whole human body segment motions, the model needs to be discretized.

2.2.3 Generation of virtual sensors and synthesized data

Generated biomechanical model gives joint angles and positions in a 3D reference space. The segment lengths are defined by the calibration step, and each segments are connected to another by a kinematic joint (except for extremities). To evaluate the kinematic and dynamic parameters in new points on the segment (Figure 2.5) one can use the moment transport rule.

The dynamic and kinematic torsors ($\mathcal{D}(S/R)$ and $\mathcal{V}(S/R)$) are defined by:

$$\mathcal{D}(S/R) = \begin{Bmatrix} \overrightarrow{A}(S/R) \\ \overrightarrow{\delta}(B \in S/R) \end{Bmatrix}_{B/R} \tag{2.1}$$

$$\mathcal{V}(S/R) = \begin{Bmatrix} \overrightarrow{\Omega}(S/R) \\ \overrightarrow{V}(B \in S/R) \end{Bmatrix}_{B/R} \tag{2.2}$$

where S is the considered solid (or segment), R the reference frame, B the application point, $\overrightarrow{V}$ the velocity vector, $\overrightarrow{\Omega}$ the angular velocity vector, $\overrightarrow{A}$ the acceleration quantity and $\overrightarrow{\delta}$ the dynamic moment. To evaluate the moments from point A to B the torsors can be rewritten as:

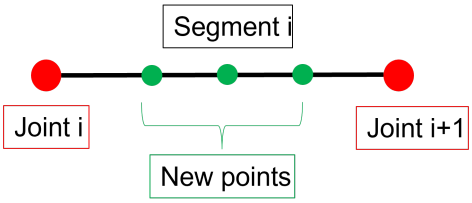

Figure 2.5 – Illustration of the segment and joint structure.

$$\mathcal{V}(S/R) = \begin{Bmatrix} \overrightarrow{\Omega}(S/R) \\ \overrightarrow{V}(B \in S/R) \end{Bmatrix}_{B/R} = \begin{Bmatrix} \overrightarrow{\Omega}(S/R) \\ \overrightarrow{V}(A \in S/R) + \overrightarrow{BA} \wedge \overrightarrow{\Omega}(S/R) \end{Bmatrix}_{B/R} \tag{2.3}$$

$$\mathcal{D}(S/R) = \begin{Bmatrix} \overrightarrow{A}(S/R) \\ \overrightarrow{\delta}(B \in S/R) \end{Bmatrix}_{B/R} = \begin{Bmatrix} \overrightarrow{A}(S/R) \\ \overrightarrow{\delta}(A \in S/R) + \overrightarrow{BA} \wedge m_E \overrightarrow{\Gamma}(S/R) \end{Bmatrix}_{B/R} \tag{2.4}$$

where m_E is the total mass.

The constructed biomechanical model is processed and discretized and corresponding locations of RID are kept for comparison as illustrated in Figure 2.6.

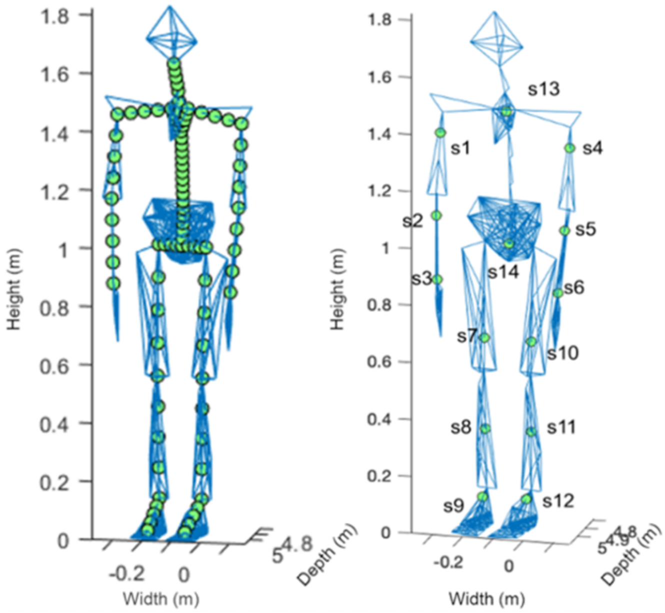

Figure 2.6 – Discretized biomechanical model. Left: Synthesized IMU Data (SID) positions where each green circle represents a virtual sensor location. Right: SID virtual locations corresponding to RID location.

2.3 Data analysis: Synthesized data reliability

2.3.1 Temporal domain

After temporally synchronizing both systems, only the signal norms are studied to get rid of the sensors orientations in space. The signal norm is obtained using eq. 2.5.

$$\|s(t)\| = \sqrt{x(t)^2 + y(t)^2 + z(t)^2}, \tag{2.5}$$

where s(t) represents the physical quantities measured as a function of time along the three axes $\vec{x}$, $\vec{y}$, $\vec{z}$. SID and RID are then compared using statistical and frequency features. We used the Bland-Altman plot to illustrates the difference between SID and RID samples. In addition, the considered features listed in Table 2.1 are extracted from SID and RID for extra comparison. This selection corresponds to the most widely used features in literature and will be used next in the HAR part. Bragança et al. [96] highlight in their study the common methodology used in HAR.

Table 2.1 – List of features used for signal characterization (PSD for power spectral density).

Number	**Feature**
1	Mean
2	Standard deviation
3	Root Mean Square
4	Max
5	Min
6	Skewness of PSD
7	Kurtosis of PSD
8	First Quartile
9	Second Quartile
10	Third Quartile
11	Mean Crossing Rate
12	Mean of PSD
13	Standard deviation of PSD

Features extraction from segmented data allow a high-level representation of the signals. In addition, overlapping in the segmentation process is used to overcome loss of information. Thus, 0.5 s window and a 50 % overlapping are selected for feature extraction. Equation 2.6 presents how the normalized relative error between SID and RID is calculated:

$$RMSE = \frac{\sqrt{\frac{1}{N}\sum_N (RID - SID)^2}}{\sqrt{\frac{1}{N}\sum_N RID^2}} \tag{2.6}$$

where N stands for the number of windows for all samples.

2.3.2 Frequency analysis

To perform the frequency analysis, we first used the classical fast Fourier transform (FFT) method. The FFT of a signal f can be obtained using the equation eq. 2.7.

$$\mathcal{F}(f) = \int_{-\infty}^{+\infty} f(x)e^{-ix2\pi t}dx \tag{2.7}$$

Nevertheless, acceleration data can be considered as a non-stationary signal or non-periodic signal, thus, we also used the continuous wavelet transform (CWT) [97]. The CWT of a signal f can be obtained using eq. 2.8a and eq. 2.8b.

$$g(s,t) = \int_{-\infty}^{+\infty} f(t)\psi^*_{s,t} dt \tag{2.8a}$$

$$\psi^*_{s,t} = \frac{1}{\sqrt{s}}\Psi(\frac{t-\tau}{s}) \tag{2.8b}$$

where s is the dyadic dilatation, τ the dyadic position and Ψ the wavelet function. The frequency of human motions is mainly between 4 and 26 Hz [98]. Therefore, according to the Nyquist-Shannon theorem, the sampling frequency must be at least 52 Hz.

Nyquist-Shannon theorem

In signal processing, the Nyquist-Shannon theorem establishes condition about the sample rate for the discretization of continuous-time signals. To capture all the information contained in the frequency band of the signals and avoid aliasing, the sampling frequency must be twice the frequency of the observed phenomenon. The condition can be written as:

$$f_m \leqslant \frac{f_s}{2} \tag{2.9}$$

where f_m is the maximum frequency existing in the frequency band of the continuous-time signal and $\frac{f_s}{2}$ is the Nyquist frequency (sampling frequency divided by 2) [99].

SID are sampled at 240 Hz and RID are sampled at 370 Hz, thus the Nyquist-Shannon condition is satisfied. Nevertheless, the impacts produced can not be perfectly captured by the measurement systems as they exist in a very short time.

2.3.3 HAR application

As a proof of concept, a very common and simple support vector machine (SVM) classifier with a second-order polynomial kernel is implemented. Training and evaluation of SVM models are performed in different ways, the Figure 2.7 presents the proposed workflow.

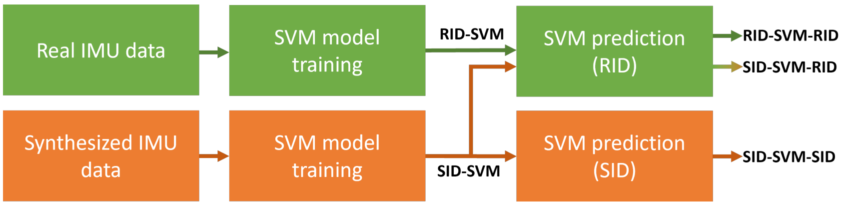

Figure 2.7 – Workflow for SVM models evaluation. 3 aspects are studied and are presented in the format 'Training - Model - Prediction'.

Two SVM models are trained, one on the SID and the other on RID. Each model is then evaluated on their respective data (RID-SVM-RID and SID-SVM-SID). To assess the possibility of using SID data to train SVM models for RID predictions the SVM model trained on SID is used to predict data from RID (SID-SVM-RID). The inputs are features of Table 2.1. The evaluation of the motion recognition is done by a 5-fold cross-validation. To determine the classifier accuracy, the classification score is computed, which is 1 minus the average classification loss overall folds (eq. 2.10). The classification loss is defined by the misclassification rate.

$$score = 1 - \frac{1}{K}\sum_{i=1}^{K}\sum_{j=1}^{N} w_j I\{\hat{y_j} \neq y_j\}, \tag{2.10}$$

$$\tag{2.11}$$

where $I\{.\}$ is the indicator function, w_j the weight for observation j, $\hat{y_j}$ the predicted class label, y_j the observed class label, N the number of observation and K the number of fold.

The data set is composed of 10 repetitions of three movements. For each sample consisting of a 0.5 s window of the norm of acceleration and norm of angular velocity, the 13 previously defined features are extracted, leading to a total of 26 features. So far, the dataset is composed of 702 samples with 226 samples for the countermovement jump, 234 samples for the left-side sprint and 242 samples for the right-side sprint. The duration of each movement differs, which is why we obtain a different number of samples after extraction of the features via the 0.5 s windowing. The classification models are evaluated on all locations.

2.4 Results

Temporal and frequencies studies focus on the entire signals. Features used for comparison and classification are then calculated on windowed signals.

2.4.1 Frequency domain

As a result of data fusion and optimization algorithms, data from SID are filtered. The Figure 2.8 presents the FFT of the norm of acceleration on the left hand for a jump.

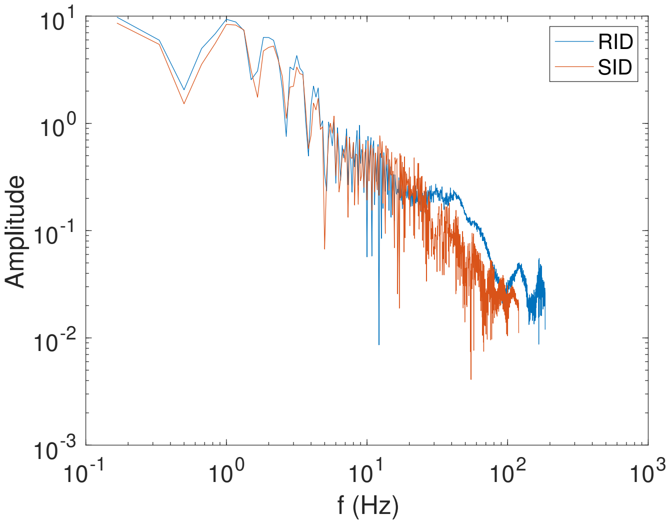

Figure 2.8 – Fast Fourier transform (FFT) of the norm of acceleration of an IMU on the left hand for a jump for synthesized inertial data (SID) and real inertial data (RID) for the entire signal.

While signals match at low frequencies (< 5 Hz), the RID signals have a larger frequency bandwidth than the SID signals (due to the higher sampling frequency - 370 Hz). In addition, in this example the magnitudes of RID signal are higher from 28 Hz to 185 Hz. Nevertheless, the result depends on the performed activity, thus, for better interpretation it is necessary to use another tool. To have a time-frequency representation of the frequencies, one can observe the CWT. Figure 2.9 presents the CWT of the norm of the acceleration for the right hand during a jump.

Under 10 Hz, both SID and RID are close but RID still has a higher amplitude. In addition, the frequency spectrum depends on the body location. Larger differences can be observed in whole frequency spectrum, the Figure 2.10 presents the norm of the acceleration for the right foot during a sprint.

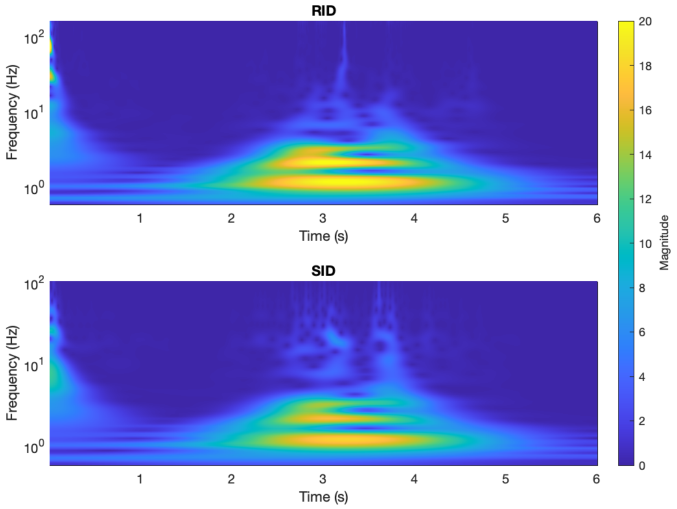

Figure 2.9 – CWT of the norm of acceleration of the right hand during a jump. The Morse wavelet was used.

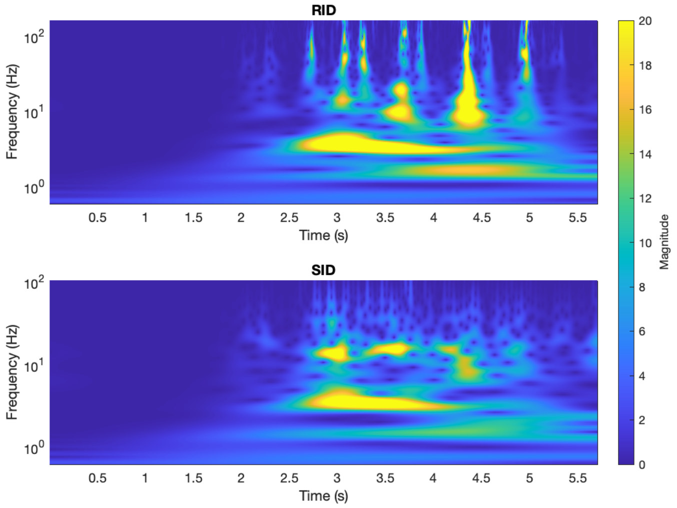

Figure 2.10 – CWT of the norm of acceleration of the right foot during a sprint. The Morse wavelet was used.

During performed activities, legs and foot are subject to high accelerations and impacts. Thus, as the SID data are filtered and not the RID, frequencies superior to 5 Hz can give different results.

2.4.2 Temporal domain

Figure 2.11 shows SID and RID temporal waveforms, the data correspond to the norm of the acceleration of an IMU located on the left hand during a jump.

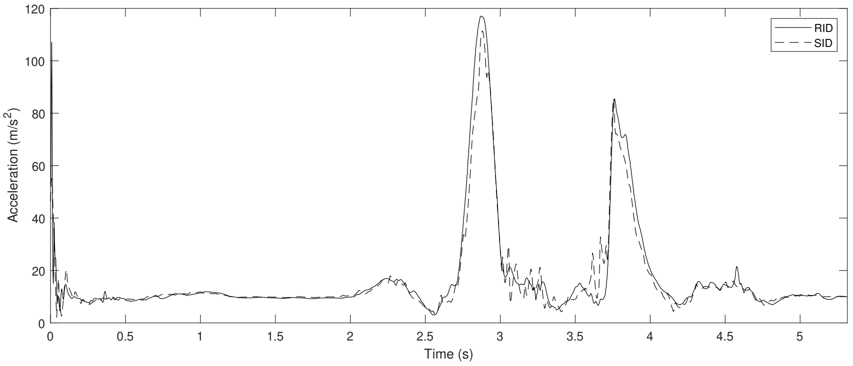

Figure 2.11 – Norm of acceleration of an inertial measurement unit (IMU) on the left hand for a jump for synthesized inertial data (SID) and real inertial data (RID).

The SID and RID acceleration match, however this is not a general result, some exceptions exist. Figure 2.12 presents the acceleration norm for SID and RID for an IMU located on the pelvis.

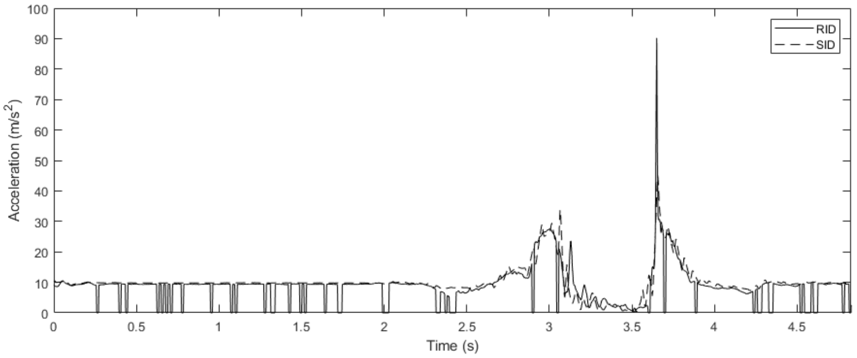

Figure 2.12 – Norm of acceleration of an inertial measurement unit (IMU) on the pelvis for a jump for synthesized inertial data (SID) and real inertial data (RID).

One can observe error in RID measurements, this could be caused by connection losses during acquisition. To compare temporally each sample of the two signals, RID and SID are filtered using a fifth-order Butterworth IIR 10 Hz low pass filter. Figure 2.13 illustrates the difference between temporal filtered RID and SID data with Bland–Altman plot.

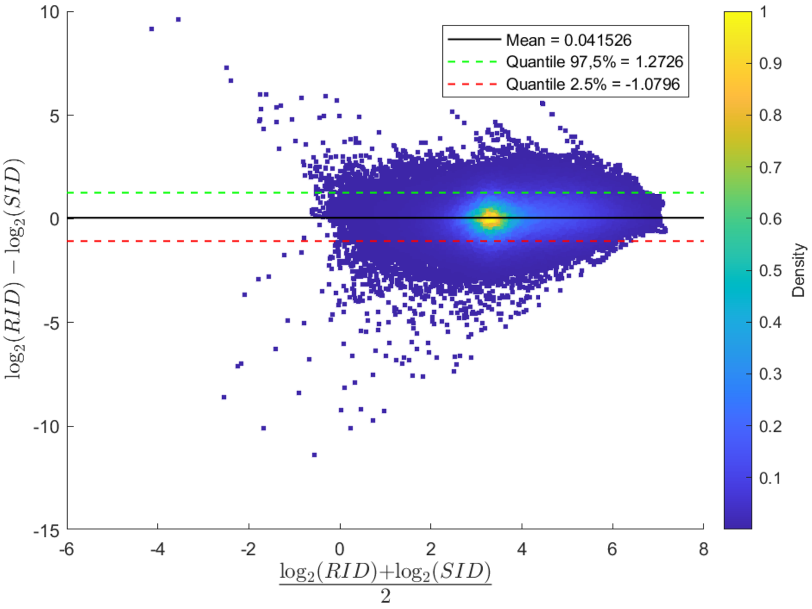

Figure 2.13 – Bland–Altman plot of the filtered RID and SID acceleration data. The observed distribution is not normal, the quantiles of 2.5 % and 97.5 % were calculated from data counting.

This plot presents in log scale the instantaneous temporal difference between RID and SID as a function of the averaged log value, for each time sample.

The average difference between RID and SID acceleration is about 0.1 g. We observe that for 95 % of the values, the error is <17% on the average acceleration of 1.4 g. The differences observed at each moment come not only from the oscillations linked to the different measurements but also from the temporal synchronization between RID and SID. To comfort these matching results, the following part focuses on the comparison between RID and SID via the use of features.

2.4.3 Features evaluation

The signals processed here are segmented into windows of 0.5 s. Statistical features introduced in Table 2.1 are extracted for the whole data set of RID and SID windows.

Figure 2.14 shows the relative normalized RMS error (RMSE) between the SID and RID data as a function of the features extracted.

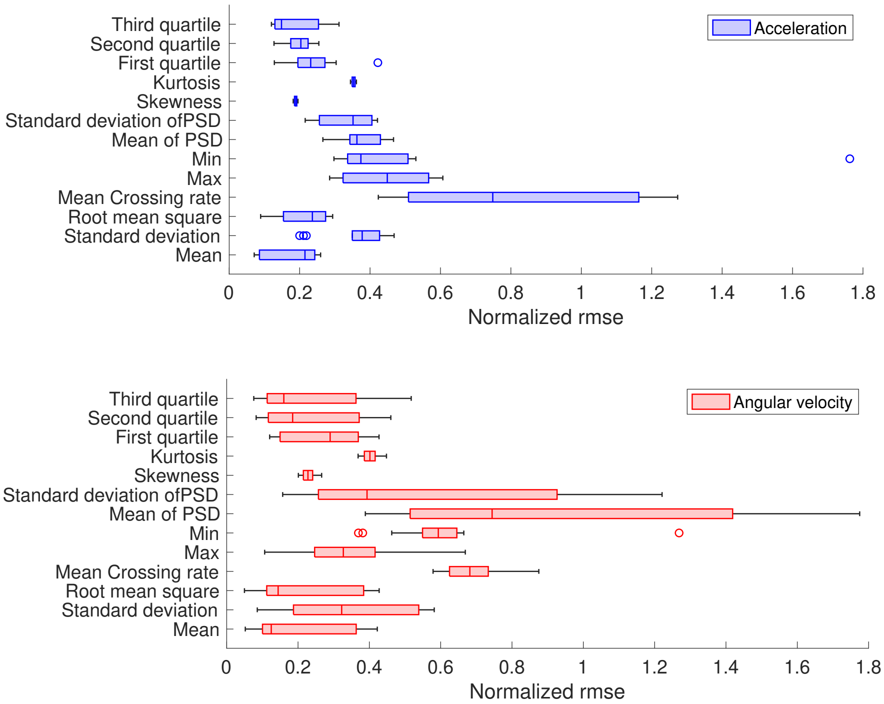

Figure 2.14 – Box plot of normalized error of the norm of acceleration (top) and angular velocity (bottom) between synthesized inertial data (SID) and real inertial data (RID) for all sensors versus features. The line inside of each box is the sample median. The left and right edges of each box are the upper and lower quartiles, respectively. Outliers are values that are more than 1.5. Interquartile range (IQR) away from the top or bottom of the box using an 'o' symbol. The whiskers are lines that extend above and below each box. One whisker connects the upper quartile to the non-outlier maximum (the maximum value that is not an outlier), and the other connects the lower quartile to the non-outlier minimum (the minimum value that is not an outlier).

The error is calculated on all accelerations and angular velocities for each sensors. The results are presented as boxplots. This presents the distribution of the error values according to the features. The 'Mean of PSD' presents a higher error than 'Skewness'. Focusing on these two examples, Figure 2.15a corresponds to the least relevant feature with an RMSE that has a third quartile below 250 % and 75 % for angular velocity and acceleration, respectively. On some outliers of the 'Mean of PSD' on sensor S1, the angular velocity has errors of >1000 %. Figure 2.15b shows a more relevant feature with errors below 20 %.

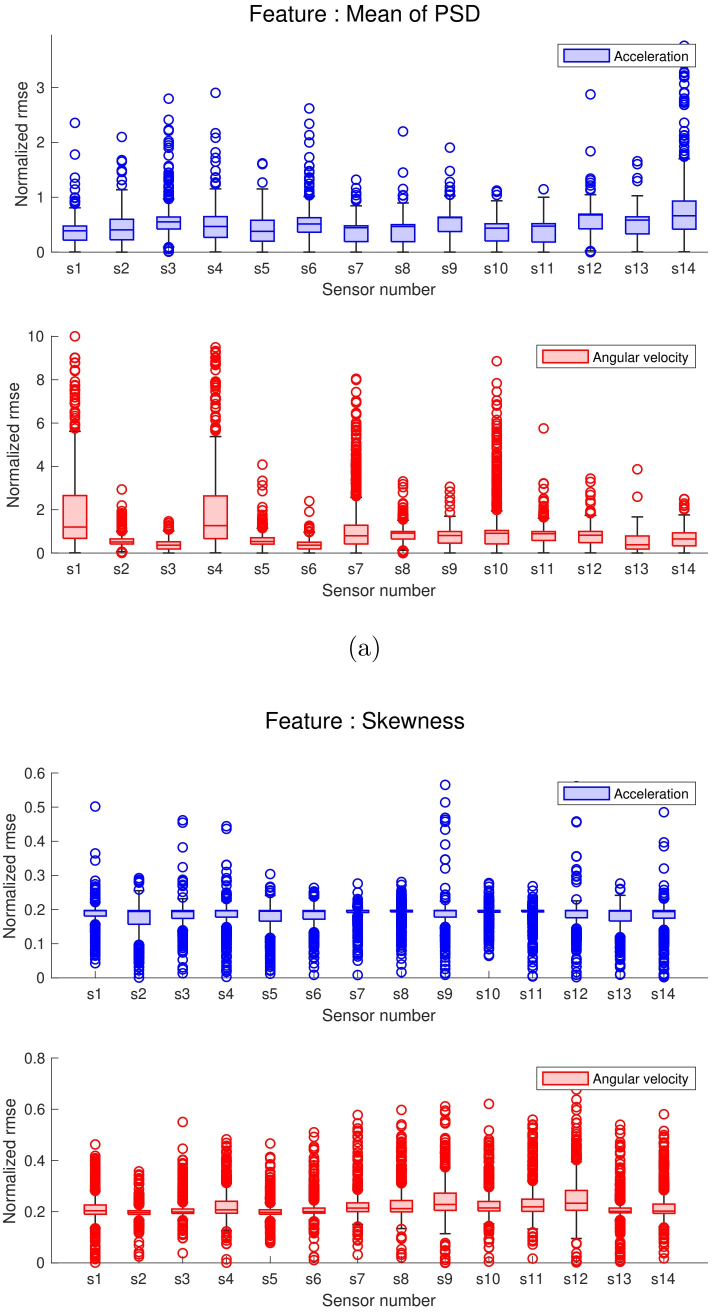

(a)

(b)

Figure 2.15 – Box plot of normalized error of the norm of acceleration (top) and angular velocity (bottom) between synthesized inertial data (SID) and real inertial data (RID). (a) Plot for a non-relevant feature (Mean of PSD, on all sensors). (b) Plot for a relevant feature (Skewness, on all sensors). Sensor numbering from Figure 2 applies.

2.4.4 Application to motion recognition

SVM classifiers have been trained on each SID position, using the previously mentioned features on velocity and acceleration amplitudes. Figure 2.16 presents the results of an avatar based on the biomechanical model.

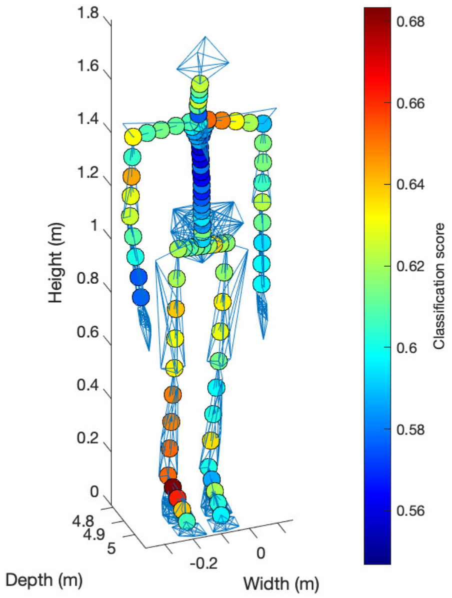

Figure 2.16 – Synthesized inertial data (SID) classification score on biomechanical model for 154 sensor locations.

The sensor locations are indicated by circles, which colors indicate the classification scores. Therefore, a classification score color map on human body is plotted. The classification scores of 154 synthesized IMU locations are represented, which assess a significantly larger number of locations compared to the only 14 real sensors. In this study, the sensors placed on the right leg are the best for motion recognition. SID and RID are also compared (Figure 2.17), the difference in classification scores for configurations SID-SVM-SID and RID-SVM-RID for each sensor is calculated by Equation 2.12, which stay below 16.7 % (Figure 2.17b).

Equation 2.12 computes the absolute errors, it is related to Equation 2.6 through Equation 2.13:

$$RMSE_C = \sqrt{\frac{1}{N}\sum_{N}(RID - SID)^2} \tag{2.12}$$

$$RMSE = \frac{RMSE_C}{\sqrt{\frac{1}{N}\sum_N RID^2}} \tag{2.13}$$

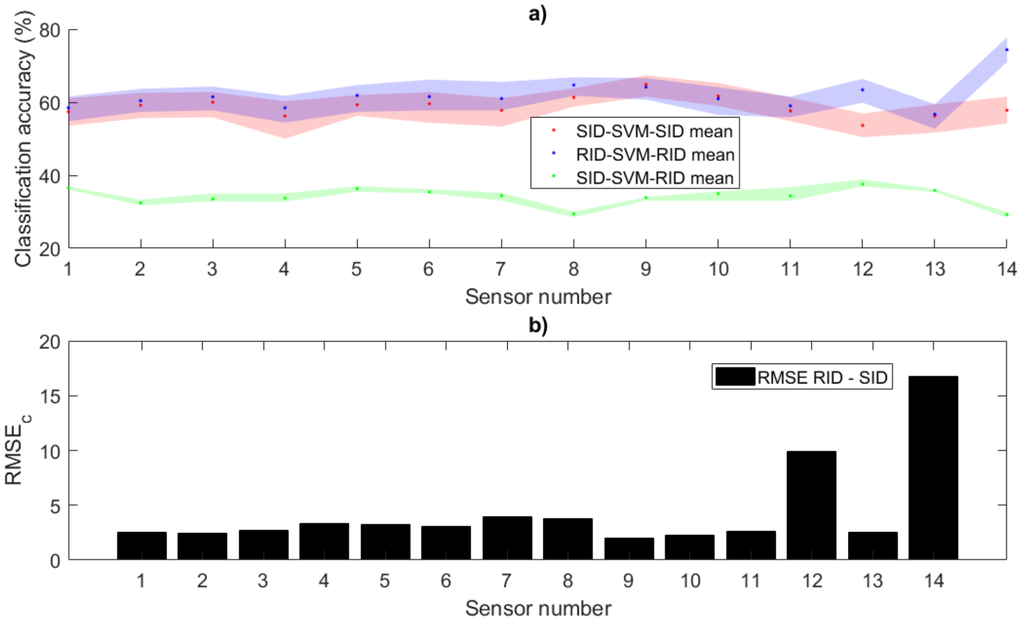

Figure 2.17 – a) Classification accuracy obtained for each configuration, we used a number a 50 evaluations to obtained the mean value. b) Difference between SID-SVM-SID and RID-SVM-RID configurations using eq. 2.12.

Regardless of the quality of the motion recognition, the trends on SID-SVM-SID and RID-SVM-RID are similar (Figure 2.17a). Nevertheless, the configuration SID-SVM-RID show low accuracy, thus SVM model trained on SID can not be relevant for RID predictions.

2.5 Discussion

The alignment between the axes is assumed constant during the experiments, the norm does not consider the possible misalignment between the SID and RID reference frames. The differences between synthesized data and real data can be explained by elements of biomechanics, signal processing, machine learning and measurement acquisitions. First, recorded data may have suffered from connectivity problems and result in data loss. As illustrated in Figure 2.12 the RID signal shows values equal to zero. Thus, the comparison study is impacted, these particular cases can lead to localized errors. Figure 2.7b shows higher rmse value for sensor number 14 corresponding to the pelvis location which appears to be correlated with measurement errors.

Second, the method is based on a numeric biomechanical model relying on assumptions. Indeed, the model does not consider soft bodies. This may explain the differences on the thigh as skins and flesh lead to artefacts as well as sensor misplacement. Soft tissue can add up to 50 % additive noise on acceleration and orientation measurements compared to actual bone motion [100]. Some joints are approximated by combinations of kinematic joints, as it is an osteo-articular model. For instance, shoulders are described by two rotations while their kinematics are much more complex [101]. The pelvis is the first kinematic node, it defines the global location of the body. It is sensitive to digital noise coming from the solver that minimizes distances between real and virtual markers for the whole body. So, these locations require special attention if selected as targets for real sensors.

Third, the biomechanical model computations imply errors. While signals match at low frequencies, the RID signals have a larger frequency bandwidth than the SID signals. This is caused by various filters stabilizing and smoothing trajectories of the biomechanical model, which are generally low pass filters. This is responsible for differences in features dynamic-sensitive like minimum, maximum, standard deviation as well as power spectral density (PSD) based features like Kurtosis or Skewness. One should keep in mind that highly dynamic-sensitive features are useful to discriminate motions, while they present a poor suitability between SID and RID. Finally, the selected classifier used in this chapter for motion recognition is chosen to be simple. Therefore, the results can be improved significantly, but this is out of the scope of this chapter. SVM classifier with the second-order polynomial kernel is selected because it is a classic and mostly used algorithm. The modeling of the motion, that is, considering statistical features on 0.5 s window, is not the best fit to describe motions that can last several seconds decomposed in multiple substeps. The results may benefit from considering multiple sensors or from more advanced classification algorithms like Markov Chains considering data history or from the latest artificial intelligence algorithms such as deep artificial neural networks. Other limitations that could be discussed in more detail are that only one sensor is considered at a time, the kernel bias, or the unbalance database with the small number of data and motion diversity.

The results of the SID classification (SID-SVM-SID) follow the same trend as those of the RID classification (RID-SVM-RID) (Figure 2.17), validating their use for numerical evaluation of optimal IMU locations. Most of the sensor locations show an rmse value inferior to 5 % highlighting the relevance of SID. Nevertheless, SID can not be use to train SVM models and predict classes from RID. Indeed, results show classification score inferior to 40 % for the SID-SVM-RID configuration ((Figure 2.17)a). Future studies can investigate more in detail this aspect by limiting the possible sources of errors.

2.6 Conclusion

Sensors such as IMUs are increasingly used to assess the physical activity of the human body. Finding the optimal placement of sensors is an important issue. In this chapter, a new method based on motion capture providing synthesized IMUs is proposed. This numerical model is applied to a classification algorithm for HAR application. A score classification colormap on human body has been realized for 10 times more synthesized sensors than the real available IMUs. The HAR is also done on real data for comparison; it validates the use of synthesized IMUs data for motion classification based on statistical features. Most of the evaluated human body locations give a maximum rmse of 5 % (same trend between RID and SID classification performance on 14 body locations) and open many perspectives for the future. Higher error values can be explained by special conditions such as data loss. This method avoids many experiments necessary to evaluate the optimal placement of sensors for the design of wearable systems.

Chapter 3

Kinetic energy sources on the human body: Cantilevered Piezoelectric harvesters

---

This chapter is based on the published work entitled *Hoareau, D.; Jodin, G.; Laaraibi, A.-r.A.; Prioux, J.; Razan, F.: Available Kinetic Energy Sources on the Human Body during Sports Activities: A Numerical Approach Based on Accelerometers for Cantilevered Piezoelectric Harvesters, Energies, 2023* [102] and discusses the optimal placement of cantilevered piezoelectric harvester on human body. Accelerations extracted from IMUs located on the human body provide information capable to simulate cantilevered piezoelectric energy harvester voltage responses. A distributed parameter model is implemented to identify the best locations and orientations. These best locations are then used to optimize the energy predictions of this kind of harvester on the human body.

3.1 Introduction

Harvesting energy on the human body is a great opportunity to operate electrical wearable system and can limit the use of batteries. The miniaturization of these devices makes it very challenging to design them for optimal response to the human body (maximum energy production). Human movement operates mainly at low frequency and are essentially nonperiodic [103, 98]. Indeed, the design of harmonic devices for non-stationary signal is complex, especially for signals with high dynamic like sport actions. In addition, the harvested energy depends on the localization and orientation of the piezoelectric generator (PEG) on the human body. Nevertheless, experimental measures for PEG optimal placement assessment can be tedious and the combinations of possible localization and orientation are cumbersome. The required experimental setup is neither trivial nor ergonomic. The actions performed by the athletes will be restricted, and accurate measurement of the PEG output voltage requires high-impedance devices. Alternatively, an approach based on electromechanical models can be used, as this method offers more flexibility. Various models exist in literature, one can found the lumped parameter model [104], the Rayleigh–Ritz model [105] or the distributed parameter model [106]. Nevertheless, there are trade-offs between computational time and model accuracy. For example, the distributed parameter model is accurate but computationally cumbersome, in contrast to the lumped parameter model which is simplest but has lower accuracy.

Thus, the aim of this chapter is to give guidelines and propose a method for determining the optimal placement of cantilevered PEGs on the human body. The proposed method is applied to the sports field and is based on real accelerometer data and simulations from a electromechanical models. Features of interest are extracted from acceleration data to analyze the available kinetic energy sources from cantilevered PEGs. The first part deals with the numerical implementation of the harvester model. The second part discusses the acceleration characteristics and features which participate the most in the system's operation. The last part is dedicated to the harvester power prediction with respect to the performed human activities.

3.2 Materials and Methods

3.2.1 Experiment design: Case study

A (right-handed) subject performed a 13-minute circuit of simulated sports actions, where classical actions related to basketball, volleyball, and handball were represented. Raw acceleration data was recorded and then manually labeled; the acquisition was performed using Xsens MVN Link. The system was composed of 17 IMUs with 9 degree-of-freedom (3-axis accelerometer, 3-axis gyroscope, 3-axis magnetometer) located on both hands, both forearms, both upper arms, both shoulders, both feet, both lower legs, both upper legs, pelvis, head, and T8 (sternum). The sampling frequency was 240 Hz. The attachments and protocol provided by Xsens were used to place the sensors on the body. Extra sport straps were used to increase the robustness of the attachment. Soft tissue artifacts were not considered. The sensors were placed close to the bones to limit these undesirable effects. Consequently, the results of the studied harvesters are valid if the attachment method is similar. The x-axis of the sensors was aligned with the length of the segments; the y-axis was aligned with the thickness of the segments; and the z-axis was aligned with the outgoing normal direction.

3.2.2 Cantilevered Piezoelectric Harvester model

Newton's second law illustrates, according to the following formula (eq. 3.1), the fundamental principle of dynamics:

$$\sum \vec{F_i} = m.\vec{a} \tag{3.1}$$

where $\vec{F_i}$ is the external force applied to a system, m is the system mass in motion, and $\vec{a}$ is the acceleration of the system.

Piezoelectric materials are characterized by their capacity to transform mechanical stress into electric charge. Thus, the acceleration is related to the electric charge displacement into the material. We recall the equation of the linear piezoelectricity in eq. 3.2a and eq. 3.2b.

$$\{S\} = \left[s^E\right]\{T\} + \left[d^T\right]\{E\} \tag{3.2a}$$

$$\{D\} = [d]\{T\} + \left[\varepsilon^T\right]\{E\} \tag{3.2b}$$

where T is the stress, S is the strain, E is the electric field, D is the charge density, s is the elastic elastic flexibility, ϵ is the permittivity, and d is the piezoelectric coefficient. Our study focuses on cantilever beam-based piezoelectric harvesters. As illustrated in Figure 3.1, this kind of harvester can be represented as a beam clamped at one end and free at the other.

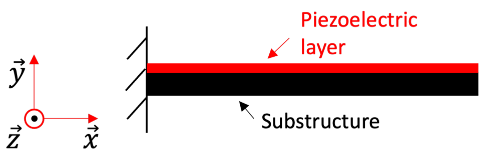

Figure 3.1 – Schematic of a clamp-free unimorph beam.

Many parameters can be adapted, such as the shape, the material, and the structure, and tip mass can be added to modify the beam behavior. Input acceleration amplitude and frequency are the main criteria to be evaluated. Thus, generally the generator is designed according to its application. However, sports movements also possess many action-induced impacts. Running, sprinting, striking, and similar actions cause many impacts. These signals present a wide frequency spectrum and can also operate generators. The appearance of the different actions performed during a circuit can be biased. Indeed, basic training, competition training, and competition conditions are different. Movement frequencies and intensities are also dependent on the observed sport [107].

We decided to conduct our study on the unimorph structure in the absence of tip mass, as it offers greater simplification for the analysis method. Nevertheless, it still illustrates the general method procedure. The distributed parameter model offers the best predictions, as it is based on the analytical solution of the coupled electromechanical system equations [106, 87]. This model considers modal analysis with Euler–Bernoulli assumptions: the shear deformation and rotatory inertia is neglected, this assumptions is valid under small deflections.

The resulting equations range from equation 3.3a to 3.6c. They are presented and explained in the following:

$$\frac{d^2\eta_r(t)}{dt^2} + 2\zeta_r\omega_r\frac{d\eta_r(t)}{dt} + \omega_r^2\eta_r(t) - \chi_r v(t) = f_r(t) \tag{3.3a}$$

$$Z\frac{dv(t)}{dt} + \frac{v(t)}{R} - \sum_{1}^{\infty}\varphi_r\frac{d\eta_r(t)}{dt} = 0 \tag{3.3b}$$

$$\varphi_r = -Y_p d_{31} b h_{pc}\left.\frac{d\Phi_r(x)}{dx}\right|_{x=L} \tag{3.3c}$$

where $v(t)$ is the voltage response to a resistive load R, $\eta_r(t)$ is the modal coordinate for the r-th vibration mode, ζ_r is the mechanical damping ratio of the r-th vibration mode, ω_r is the undamped natural frequency of the r-th vibration mode, χ_r is the modal electromechanical coupling term for the r-th vibration mode, and $f_r(t)$ is the modal mechanical forcing function. Equation 3.3a is the mechanical equation of motion in modal coordinates, and equation 3.3b is the governing electrical circuit equation.

In the absence of tip mass and by neglecting the small base rotation of the beam, the modal mechanical forcing function can be written as:

$$f_r\left(t\right) = -m\frac{d^2g\left(t\right)}{dt^2}\int_0^L \Phi_r\left(x\right)dx \tag{3.4}$$

where m is the mass per unit length, $g\left(t\right)$ is the transverse displacement of the beam base, and $\Phi_r\left(x\right)$ is the mass-normalized eigenfunction of the r-th vibration mode:

$$\Phi_r\left(x\right) = A_r\left[cos\frac{\lambda_r}{L}x - cosh\frac{\lambda_r}{L}x + \sigma_r\left(sin\frac{\lambda_r}{L}x - sinh\frac{\lambda_r}{L}x\right)\right] \tag{3.5}$$

where λ_r, A_r and σ_r are obtained as:

$$1 + cos\lambda_r cosh\lambda_r = 0 \tag{3.6a}$$

$$A_r = \sqrt{\frac{1}{mL}} \tag{3.6b}$$

$$\sigma_r = \frac{sin\lambda_r - sinh\lambda_r}{cos\lambda_r + cosh\lambda_r} \tag{3.6c}$$

The various necessary parameters are listed in Table 3.1.

The single-mode voltage response function can be written in the Laplace domain using equations 3.3a and 3.3b.

$$V\left(p\right) = \frac{pR\varphi_r f_r\left(p\right)}{\left({\omega_r}^2 + p^2 + 2p\zeta_r\omega_r\right)\left(1 + pRZ\right) + pR\chi_r\varphi_r} \tag{3.7}$$

Table 3.1 – Parameters of the harvester model

Parameter	**Description**
L	Beam length
b	Beam width
h_p, Y_p, ρ_p, e_{31}, ε_{33}^S	**Piezoceramic layer:** thickness, elastic modulus, mass density, piezoelectric constant, and permittivity constant
h_s, Y_s, ρ_s	**Substructure layer:** thickness, elastic modulus, and mass density
YI	Bending stiffness of the composite
χ_r	$-\frac{Y_p d_{31} b\left(h_c{}^2-h_b{}^2\right)}{2h_p}\left.\frac{d\Phi_r(x)}{dx}\right\vert_{x=L}$
h_{pc}	$\frac{nh_s(h_p+h_s)}{2(h_p+nh_s)}$
N	$\frac{Y_s}{Y_p}$
h_b	h_c-h_p
h_c	$\frac{h_p{}^2+2nh_sh_p+nh_s{}^2}{2(h_p+nh_s)}$
ω_r	$\lambda_r{}^2\sqrt{\frac{YI}{mL^4}}$
M	$b(\rho_s h_s+\rho_s h_p)$
Z	$\frac{\varepsilon_{33}^S bL}{h_p}$

Laplace transform

The Laplace transform of a function $f(t)$ the function $F(p)$ which is a unilateral transform defined by:

$$\mathrm{F}(p)=\mathcal{L}\{f\}(p)=\int_{0^-}^{+\infty}\mathrm{e}^{-pt}f(t)\,\mathrm{d}t \tag{3.8}$$

where p is a complex number . The function f must be locally integrable on $[0,\infty]$.

The modal mechanical forcing function can be rewritten as

$$f_r\left(p\right)=-mp^2g\left(p\right)\int_0^L\Phi_r\left(x\right)dx=-A\left(p\right)m\int_0^L\Phi_r\left(x\right)dx \tag{3.9}$$

where $A(p)$ is the base acceleration. Thus, the resulting transfer function can be written as $\frac{V(p)}{A(p)}=H\left(p\right)$. Mathworks Matlab software was used to simulate the model. Specifically, the

Matlab LSIM() function was used; it discretizes the continuous transfer function ($H(p)$) to a recurrence equation and converts the sampled acceleration data ($a(t)$) with a first-order hold. The output was then computed using the recurrence equation applied on the samples as a digital finite-response filter. This numerical method is fast. For simulation purposes, the acceleration data were upsampled. This operation does not add information to the signal and allows smaller time steps computations to be performed for better precision.

The resampling factor was evaluated using the relative error (RE) in the simulated energy:

$$RE = 100\frac{E_N - E_i}{E_N}, i = 1...N \tag{3.10}$$

where i is the resampling factor and E is the simulated energy obtained from the model using the according upsampled acceleration data. Finally, passive control was assumed with a constant resistive load R_c at the harvester output, and the energy of the simulated harvester model was calculated as

$$E_p = \int \frac{v\left(t\right)^2}{R_c} dt \tag{3.11}$$

where v is the harvester model voltage response.

To simulate the harvester model response, the data extracted from [106] were used, the characteristics are reported in table 3.2.

Table 3.2 – Materials properties of the unimorph cantilever.

Parameter	Piezoceramic	Substructure
Material	PZT	Composite
L (mm)	100	100
b (mm)	20	20
h (mm)	0.4	0.5
Tip mass	-	-
ρ_p, ρ_s (kg/m^3)	7800	7165
Y_p, Y_s (GPa)	66	100
Damping coefficient (ζ_1)	0.01	
External load (R_c)	5e6 Ohm	
d_{31} (pm/V)	-190	-
ε_{33}^S (nF/m)	15.93	-

High value of load resistance (~10^6 Ohms) can be assimilated as open circuit behaviors: the harvester output voltage is less sensitive to the variations in the load resistance [106]. However, it is interesting to visualize the influence of the load resistance in the voltage prediction, thus, the variation of R_c is investigated.

3.2.3 Hardware and software configurations

The computations were performed using Matlab R2022b (Math-Works, Inc., USA) on Windows 10 (Microsoft Corporation). The hardware system was built on AMD Ryzen 5 2600 Six-Core 3.4 GHz (CPU) with 16 Go RAM memory. Computations were performed in less than 1 second for 992290 samples of temporal data.

3.2.4 Data characteristics

Acceleration data can be mathematically categorized as finite energy signals, as they are non-stationary and have a finite time span. $L^2\left(R, C\right)$ is the space of finite energy signals. The mathematical signal energy, E_{signal}, is obtained using equation 3.12.

$$E_{signal} = \|s\|^2 = \int_{-\infty}^{+\infty} x(t)^2 dt \tag{3.12}$$

where s is the finite energy signal. Moreover, sport-related actions can be manifold, and high-velocity interactions between the body and the environment are observable. Feet come into contact with the floor during running and jumping, and there are ball interactions during hits and passes; all of these cause high acceleration and deceleration magnitudes, translated as abrupt changes. To perform a detailed time–frequency analysis, it is not possible to use a common tool such as the Fourier transform, because it does not allow one to precisely locate the transients of the signal. Thus, here, the wavelet transform was used [97]. For the precise representation of the different frequencies present in the acceleration, the continuous wavelet transform (CWT [108]) was computed (using the CWT() function in Matlab). And for signal decomposition or reconstruction, the maximum overlap discrete wavelet transform (MODWT [109]) was computed (using the MODWT() function in Matlab). As discussed in the above paragraph, acceleration data contain impacts. This is related to quick and abrupt changes in the signal transients. Depending on the width of the impacts, the frequency spectrum can be very wide or even present all frequencies, as in the theoretical Dirac delta distribution. Nevertheless, the whole dynamic is only observable if the sampling frequency is at least two times greater than the maximum frequency of the impacts according to the Nyquist–Shannon theorem [110]. In practice, the sampling frequency must be 5 or 10 times greater.

3.2.5 The influence of the orientation of the harvester

The harvested energy is inherently related to the location of the harvester on the human body. Positions with periodic and highly dynamic motions are the most suitable ones. Moreover, the orientation of the harvester impacts the potential energy harvested. The structure of the harvester allows voltage to be generated from unidirectional stress only in correspondence with the deflection axis (DA) of the beam. To assess the influence of the orientation, the harvester model was simulated for multiple angular rotations from the IMU reference frame. Nevertheless, to avoid redundancy in the results, the range of angular variation was restricted. The Cartesian space is defined by 3 axes ($\overrightarrow{x}, \overrightarrow{y}, \overrightarrow{z}$); thus, 3 rotations could be introduced, and $R_x(\theta_1), R_y(\theta_2), R_z(\theta_3)$ are the rotation matrixes for the x-axis (which rotates the y-axis to the z-axis), the y-axis (which rotates the z-axis to the x-axis), and the z-axis (which rotates the x-axis to the y-axis), respectively. The general orientation in space can be obtained by multiplying $R = R_z(\theta_3)\, R_y(\theta_2)\, R_x(\theta_1)$, i.e., the Cardan angles. The number of possible rotations for one vector can be represented by a sphere (Figure 3.2); however, depending on the harvester structure, this space can be reduced:

- — The harvester has a single degree of freedom. Therefore, it has rotation invariance around the DA, which does not change its direction;
- — The harvested energy is independent of the voltage sign (i.e., the acceleration sign). Therefore, it has symmetry invariance, as shown in equation 3.13.

$$E_p = \int \frac{v(t)^2}{R_c} dt = \int \frac{(-v(t))^2}{R_c} \tag{3.13}$$

The space of possible orientations is now contained in a semi-sphere. Assuming that the DA is equal to the $\overrightarrow{x}$ axis, every possible rotation in 3D space can be obtained with $R = R_z(\theta_3)\, R_y(\theta_2)\, R_x(\theta_1)$ in the general case. With space reduction we obtain $\begin{cases} R_x(\theta_1) = I \text{ (Rotation invariance)} \\ \theta_3, \theta_2 \in \left[\frac{-\pi}{2}; \frac{\pi}{2}\right] \text{ (Symmetry invariance)} \end{cases}$ where I is the identity matrix.

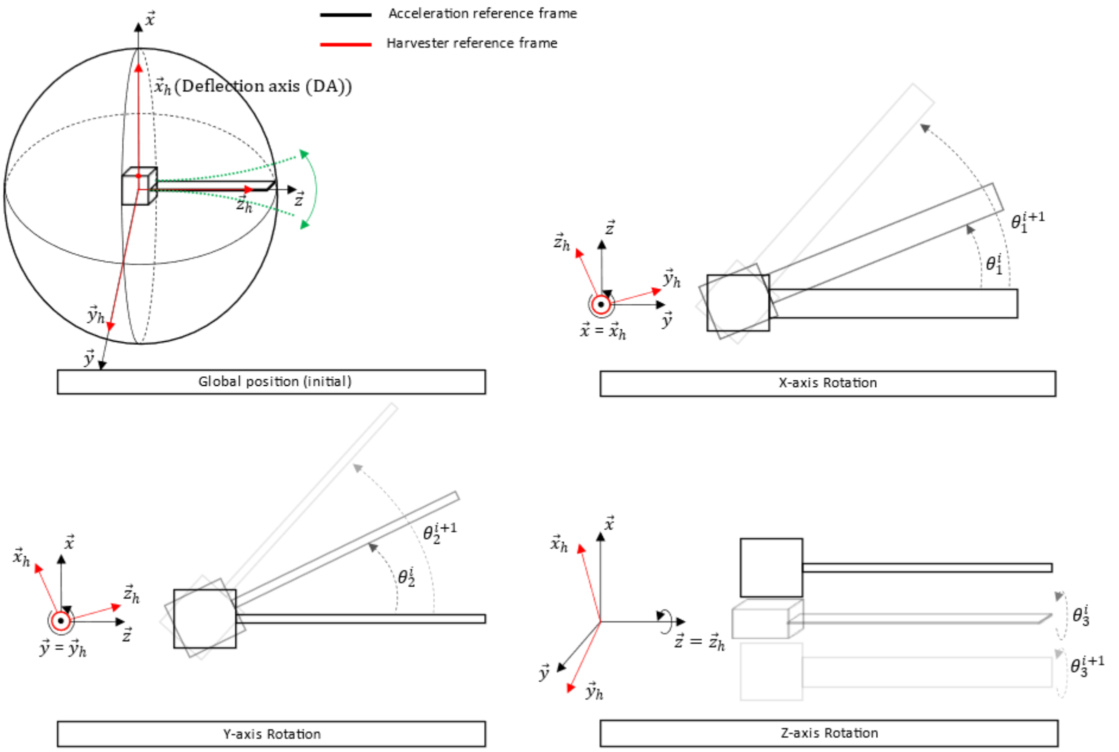

Figure 3.2 – Harvester orientation in Cartesian space. The rotation around the $\vec{x}_h$ axis (deflection) does not impact the deflection direction. The harvested energy is not impacted.

3.2.6 Most relevant features (MRFs)

As the input signals of the model are not stationary, it is interesting to analyze the features offering optimal harvesting. Depending on the quality factor, the best efficiency is obtained when the harvester operates in its bandwidth. Impulses are relevant to the power harvester because of the large frequency spectrum. They are highly present in sports. To determine if impulses were part of the MRFs, they were extracted from the acceleration data and compared to both the total signal energy and the harvested energy of the simulated model. The method is described in Figure 3.3.

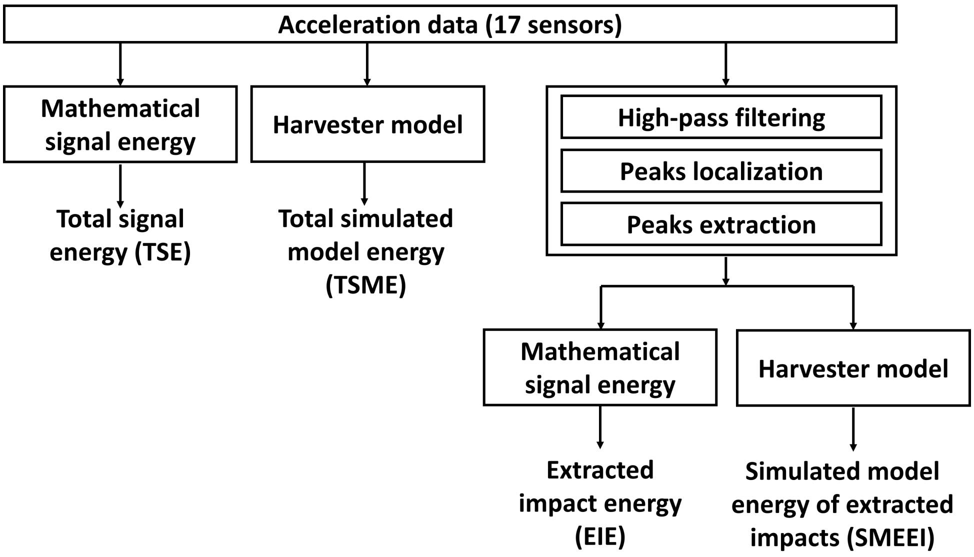

Figure 3.3 – Flowchart of impact evaluation method. The first step consists in calculating the mathematical signal energy and simulating the harvester model energy using the total acceleration data. The second step consists in extracting the impacts from the acceleration data and then calculating the new mathematical signal energy and simulating the new harvester model energy.

To extract the impacts from the acceleration data, the first step was performing high-pass filtering using MODWT and inverse MODWT to keep the high-frequency components.

This method is relevant for non-stationary signals and has the advantage of being automatic in the sense that a classical digital high-pass filter would need to set an order, a cut-off frequency, ... Then, peak localization was performed with the Matlab FINDPEAKS() function, which gives the local maxima in a sliding window. Finally, using the corresponding peak localization on the acceleration data, the impacts were extracted with an adapted time window.

3.2.7 Influence of human activities in energy prediction

The conducted study discusses the energy prediction for the whole performed circuit. As the circuit is composed of various qualified activities, it is possible to evaluate their contribution. Thus, the energy prediction is computed for each location and for each activities. The acceleration data is first segmented according to activities execution time. For each activity the optimal orientation for the harvester will be investigated using a particle swarm optimization (PSO) with the Matlab function PARTICLESWARM().

The optimization problem can be written as:

$$\underset{\theta\ =\ \{\theta_2,\ \theta_3\}}{minimize}\ f(\theta) \tag{3.14}$$

$$f(\theta) = -\int \frac{v(t,\theta)^2}{R_c}\mathrm{d}t \tag{3.15}$$

$$\begin{bmatrix} \frac{d^2g(t)}{dt^2} \\ - \\ - \end{bmatrix} = R(\theta) \begin{bmatrix} a_x(t) \\ a_y(t) \\ a_z(t) \end{bmatrix} \tag{3.16}$$

$$\frac{-\pi}{2} \leqslant \theta \leqslant \frac{\pi}{2} \tag{3.17}$$

where R_c is the load resistance, $\frac{d^2g(t)}{dt^2}$ is the harvester base transverse acceleration corresponding to A(p) in Laplace domain, $R(\theta)$ is the rotation matrix obtained with the Cardan angles, $a_x(t), a_y(t)$ and $a_z(t)$ are the accelerometer measurements in the local frame and the product A(p)H(p) leads to V(p) (v(t) in temporal domain) obtained in equation 3.7. We used a swarm size equal to 20, other parameters are set to Matlab default values. For better interpretation and because the performed activities are not well balanced, we will visualize the mean of the predicted power.

3.3 Results and Discussion

3.3.1 Simulation of harvester model

The resonant frequency of the first vibration mode of the simulated model was equal to 48.8 Hz in open circuit condition (47.8 Hz in short circuit condition) with a phase of -90 degrees.

The Bode diagram is shown in Figure 3.4. Here, only the first vibration mode was considered, as the second mode (301.5 Hz) was far from the Nyquist frequency of the acceleration data (120 Hz). To accurately simulate the temporal voltage responses, the acceleration data were upsampled using a resampling factor, where the value was chosen to obtain a relative error (RE) inferior to 1 %. Figure 3.5 presents the RE for each axis of each sensor.

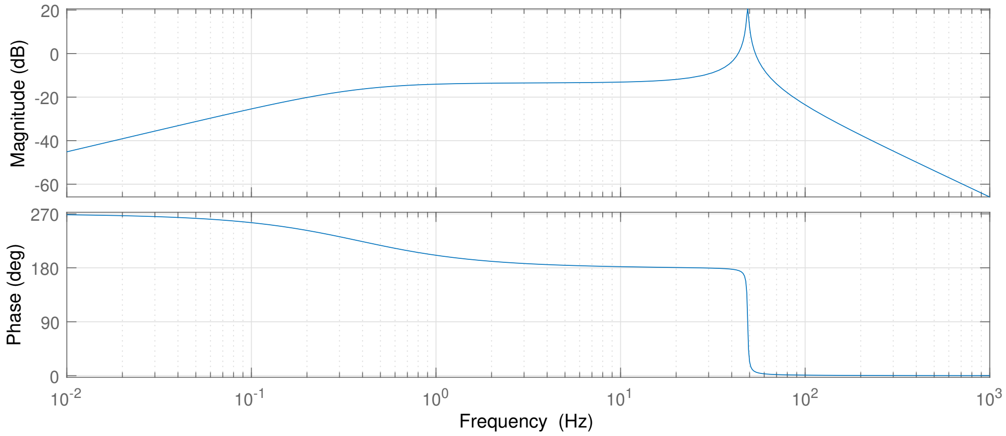

Figure 3.4 – Bode plot of the harvester model. Peak resonance is observed at 48.8 Hz.

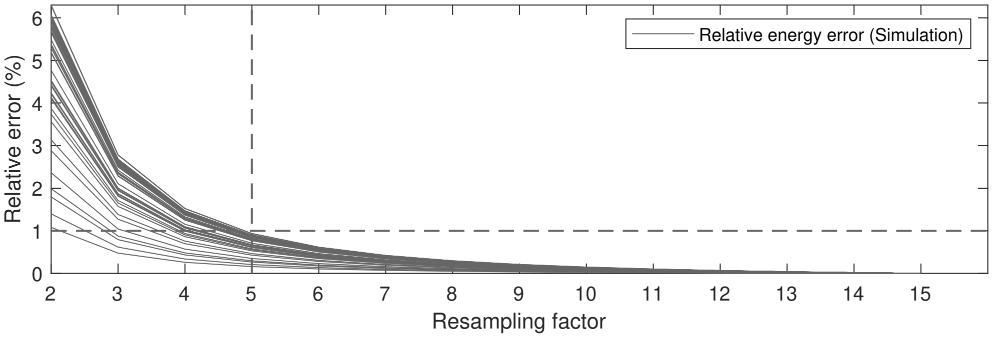

Figure 3.5 – Relative error in energy simulations according to the resampling factor of the acceleration data. One line is drawn for each sensor (17).

It is suitable to increase the resampling factor to reduce the simulation artifacts, but high values impact the simulation time. Subsequently, the value of the factor was fixed to 5. The resampled acceleration data were used as inputs to the harvester model.

Figure 3.6 presents the predicted voltage response using the acceleration data on the y-axis of the left-foot IMU. Observing the temporal response highlighted that a brief impact of high acceleration magnitude gave higher voltage generation. Indeed, impacts present large frequency spectra, which can operate the harvester in its bandwidth. The observed pseudo-periods in the voltage transients were equal to the resonance frequency of the harvester.

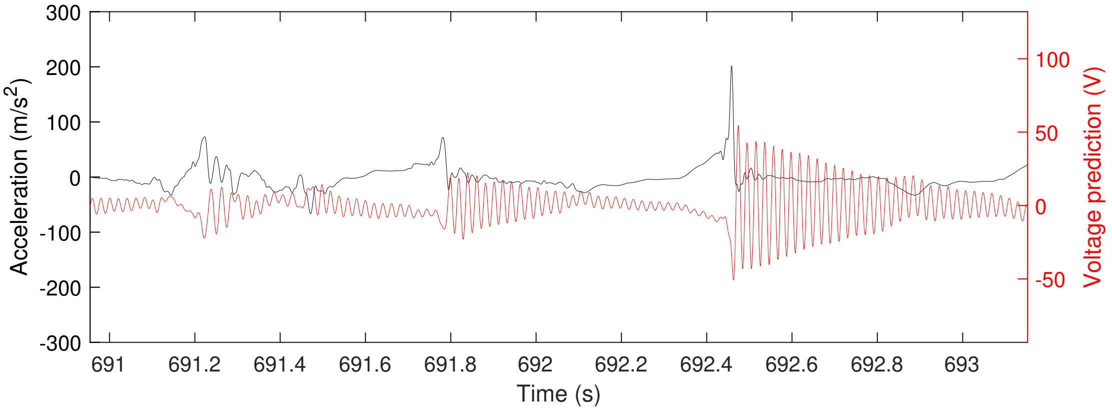

Figure 3.6 – Acceleration data of the left foot on the y-axis (black) and model voltage response (red). The original data were clipped for illustration purposes.

The value of the load resistance impacts the output voltage and thus the output power. Figure 3.7 illustrates the voltage variation for different value of load resistance.

When the load resistance is close to 1e6 Ohms, the voltage variation decreases, the system is close to open circuit conditions. In contrast, when the value of the load resistance is low, the voltage variation increases, it is assimilated to short circuit conditions. In practice, when impedance matches with the interface circuit, there is an optimal resistance that maximizes the output power.

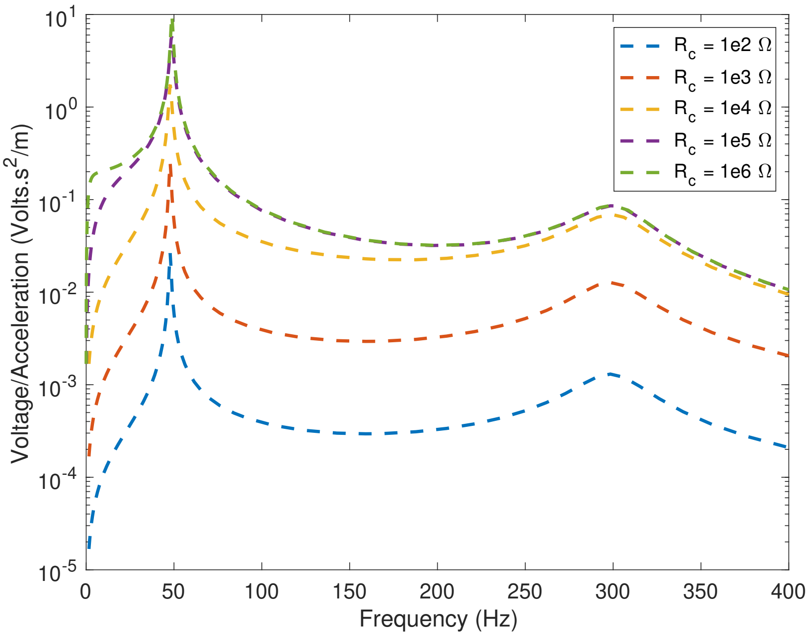

Figure 3.7 – Influence of load resistance R_c variation on output voltage.

3.3.2 Orientation of the harvester

Not all sensor locations experienced the same acceleration profiles nor impacts related to the physical activity of the subject. Depending on the original fixations of the IMUs on the body, optimal DA orientation was obtained by rotating the local reference frame according to two axes of rotation. Assuming that the DA was aligned with the IMU x-axis, Figure 3.8 presents the orientation influence on energy simulation for the right hand found by investigating y- and z-axis rotations (results for all evaluated locations are presented in appendix A3).

Taking the results for the right hand, optimal DA orientation was obtained with rotations of -88° around the y-axis and 4.5° around the z-axis (Figure 3.9). In this case, it approximately represented the direction normal to the surface of the hand. In the same way, the optimal DA orientation was obtained for each location.

By extracting the best orientation for all locations, the optimal placement for harvesting energy based on the simulated actions was evaluated. Figure 3.10 presents the normalized simulated energy at the 17 sensor locations for optimal DA orientation.

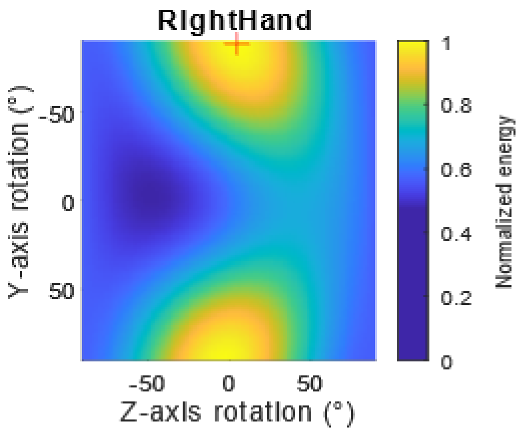

Figure 3.8 – Influence of orientation on harvester normalized energy simulation for the right hand from IMU local reference frame. Optimal orientation is indicated by a red cross. Xsens location labels are used.

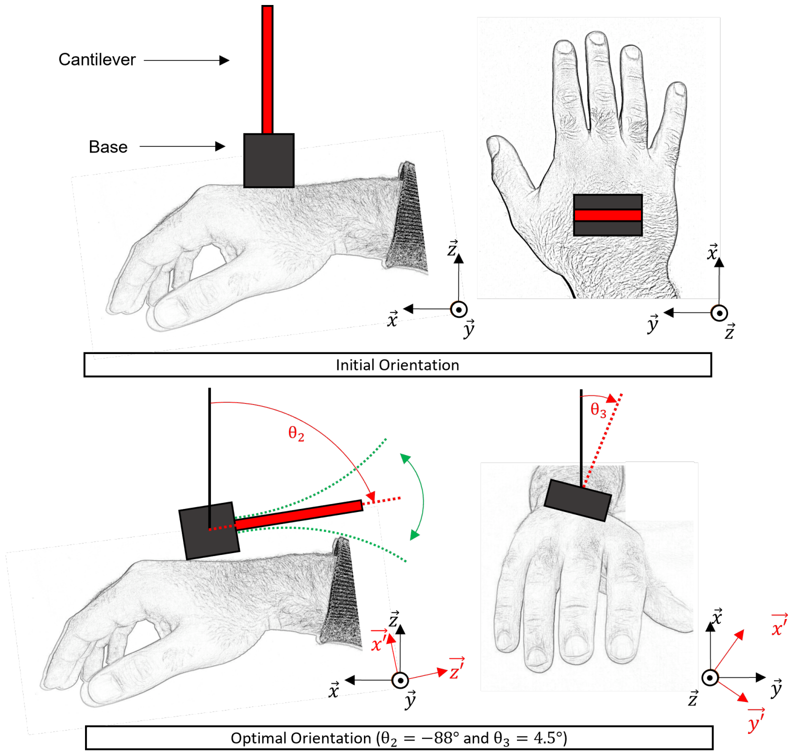

Figure 3.9 – Initial and optimal orientations of the harvester on the right hand. On the top, the initial fictive placement of the harvester is presented. This position corresponds to the IMU orientation with the DA aligned with $\overrightarrow{x}$. On the bottom, the optimal orientation according to Figure 3.8 is presented with rotation around $\overrightarrow{y}$ and $\overrightarrow{z}$.

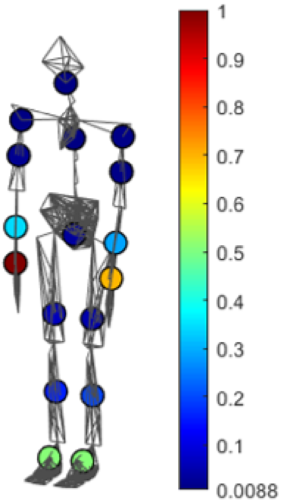

Figure 3.10 – Normalized energy simulation of the different sensor locations mapped on the biomechanical model constructed using Xsens. In this case, with a right-handed subject, the best location is the right hand.

Body extremity segments were found to be suitable for energy harvesting. In this study, the best placement was found to be located on the right hand. Hands and feet were both mainly used and showed various impacts related to the performed sports actions. Shoulders, sternum, head, and upper legs were less relevant. Moreover, differences between left and right body parts were caused by the non-symmetrical nature of the performed actions and by the fact that the subject was right-handed.

3.3.3 Impact distribution

To better understand the energy simulation results of the harvester model, a time –frequency analysis of the acceleration data was conducted. Figure 3.11 shows the CWT of the acceleration data of one IMU location using the Morse wavelet. Frequencies were mainly between 1 Hz and 120 Hz. As mentioned above, frequency band observation was limited by the value of the IMU sampling frequency. For the left foot, magnitudes were higher when the frequency was superior to 10 Hz. Vertical lines corresponding to impacts related to the subject’s jumps can be observed. One can observe that the frequency band of the impacts was relatively large, and the maximum value reached was 52 Hz. To assess the influence of impacts on the simulated energy, the method presented in Figure 3.3 was used.

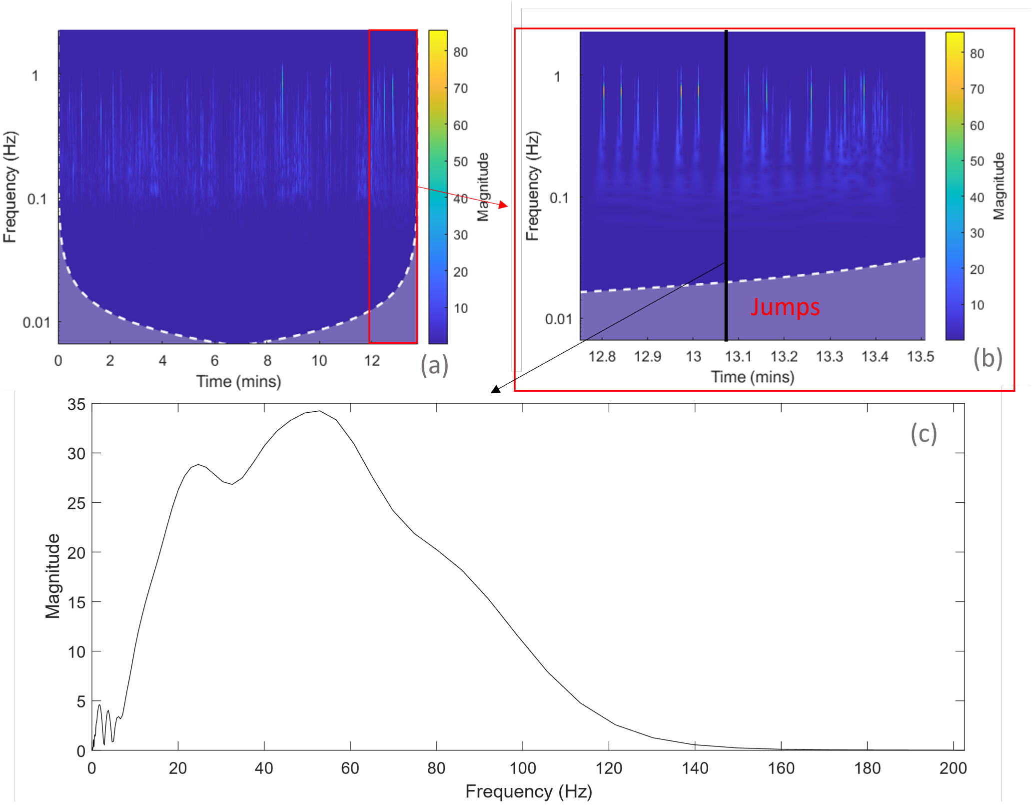

Figure 3.11 – (a) CWT of acceleration data of the left foot for optimal DA orientation. The Morse wavelet was selected for visualization. (b) Partial visualization of the CWT for illustrating the frequency components present in jumps. (c) Temporal frame of the frequency spectrum of an impact caused by a jump. This figure shows the frequency spectrum repartition for a fixed time.

The acceleration data were filtered using the first four frequency bands of MODWT with the Sym4 wavelet, which corresponded to frequencies between 75 Hz and 1200 Hz (due to resampling). The minimum peak value detection was set to 30 m/s^2, and the minimum space between peaks was set to 50 ms. Localized peaks were extracted from a centered window of 50 samples (about 41 ms). Figure 3.12 presents the original data and their reconstructed signals based on impacts only. The mathematical energy of the original acceleration data was compared to the simulated energy of the harvester model. The table 3.3 recalls the different quantities used and their expression. Figure 3.13 shows the different energy values for raw acceleration data (TSE) and harvester model simulation (TSME) according to each location. To focus on qualitative comparisons, the energies have been normalized to get maximum value of 1.

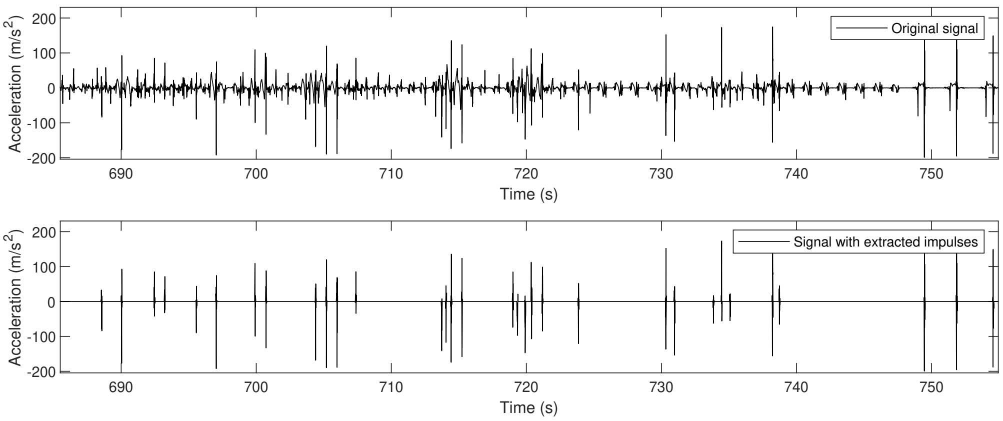

Figure 3.12 – The graph on the top shows the original resampled acceleration data. The graph on the bottom shows the same signal with the extracted impacts only.

Table 3.3 – Reminder of quantity definition

Quantity	**Definition**	**Expression**
TSE	Energy of the original acceleration signal (s)	$\|s\|^2$
TSME	Simulated energy of the harvester model from the original acceleration signal	$\int \frac{v(t)^2}{R_c}$ with s as input
EIE	Energy of the impacts in the acceleration signal ($s_{filtered}$)	$\|s_{filtered}\|^2$
SMEEI	Simulated energy of the harvester model from impacts in the acceleration signal	$\int \frac{v(t)^2}{R_c}$ with $s_{filtered}$ as input

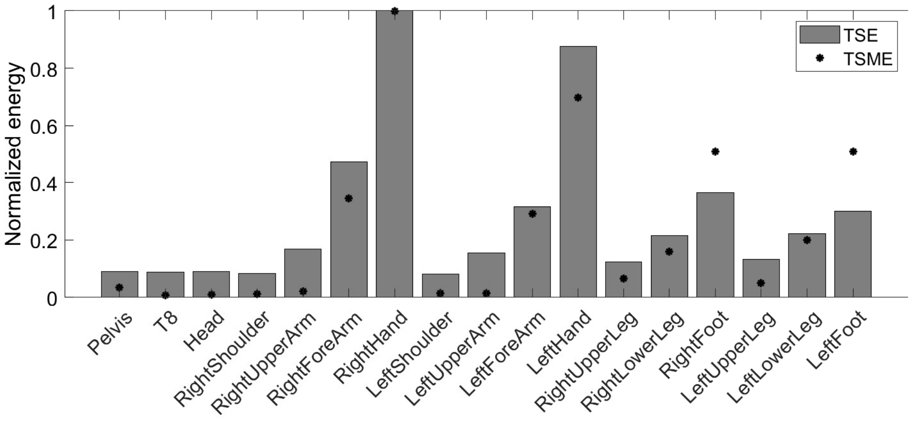

Figure 3.13 – Normalized energy of acceleration data (TSE) and simulated harvester model (TSME) at different body locations.

Overall, the trends of TSE and TSME were similar. A great value of simulated energy in the harvester model can be translated as a high mathematical signal energy value. TSE can be seen as a meta-indicator that indicates the presence of suitable locations to harvest energy. Nevertheless, this indicator only allows qualitative observations to be conducted. This observation was then performed for the extracted impacts. Figure 3.14 presents the energy ratios obtained from the original acceleration data and the extracted impacts.

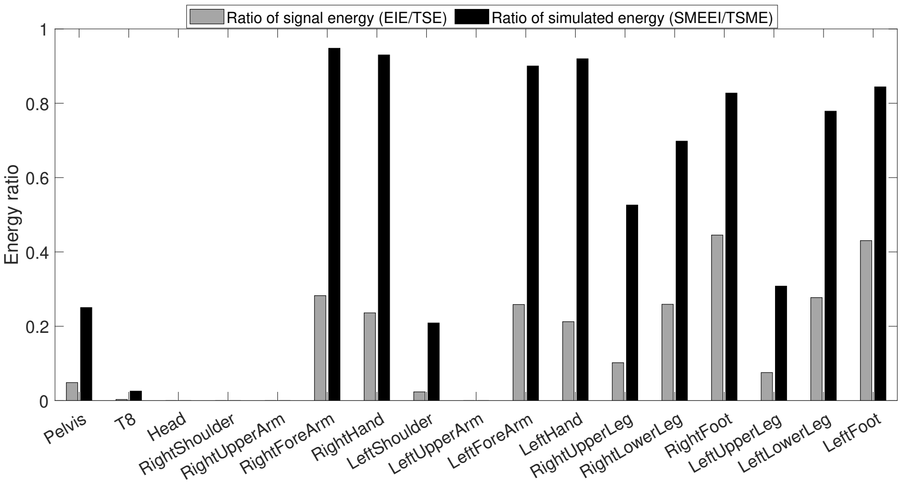

Figure 3.14 – Ratios of energy from extracted impacts only and original data. The signal energy was obtained using the mathematical energy (equation 12), and the simulated energy was obtained using the harvester model simulation.

In locations such as hands and forearms, the impacts caused more than 90% of the simulated energy. The extracted impacts caused less than 30% of the mathematical energy of the original data. More than 70% of the simulated energy for feet and lower legs was caused by impacts. The extracted impacts caused less than 50% of the original mathematical energy. Some locations such as upper arms, head, T8, and shoulders were not affected by impacts, since they had very few detected peaks. Overall, a high simulated energy value was caused by impacts, which could then be considered MRFs. Impact number, period, and amplitude for each location are summarized in Table 3.4.

Table 3.4 – Impact characteristics for each body location. Mean and standard deviation (SD) are shown for period and amplitude features (mean ± SD).

Location	Right Hand	Left Shoulder	Left Upper Arm	Left Forearm	Left Hand	Right Upper Leg
Number of impacts	201	8	0	119	184	35
Period (s)	3.4 ± 4.1	66.6 ± 149.9	0 ± 0	5.7 ± 9.8	3.7 ± 7.7	19.7 ± 31.9
Amplitude (m/s2)	138 ± 70.2	77.8 ± 14.6	0 ± 0	138.1 ± 60.3	134.4 ± 72.2	76.2 ± 31.5
Location	Pelvis	T8	Head	Right Shoulder	Right Upper Arm	Right Forearm
Number of impacts	22	1	0	0	0	133
Period (s)	35.1 ± 37.3	0 ± 0	0 ± 0	0 ± 0	0 ± 0	5.1 ± 7.7
Amplitude (m/s2)	76.6 ± 30.3	92.4 ± 0	0 ± 0	0 ± 0	0 ± 0	139.1 ± 65.2
Location	Right Lower Leg	Right Foot	Left Upper Leg	Left Lower Leg	Left Foot	
Number of impacts	91	247	20	98	221	
Period (s)	8.7 ± 17	3.3 ± 5.6	35.1 ± 78.9	8 ± 14.2	3.5 ± 6.6	
Amplitude (m/s2)	96.8 ± 49.7	93.9 ± 53.4	70.8 ± 41	91.7 ± 47.5	93.7 ± 49.5	

3.3.4 Performed activities contribution

The contribution of activities in the model power prediction is evaluated for each locations using the best orientation for the harvester (optimized by PSO). Figure 3.15 presents the mean power prediction for some body location and the according performed activities, for clarity purposes, the other studied locations are presented in Figure A1 and A2 located in the appendices.

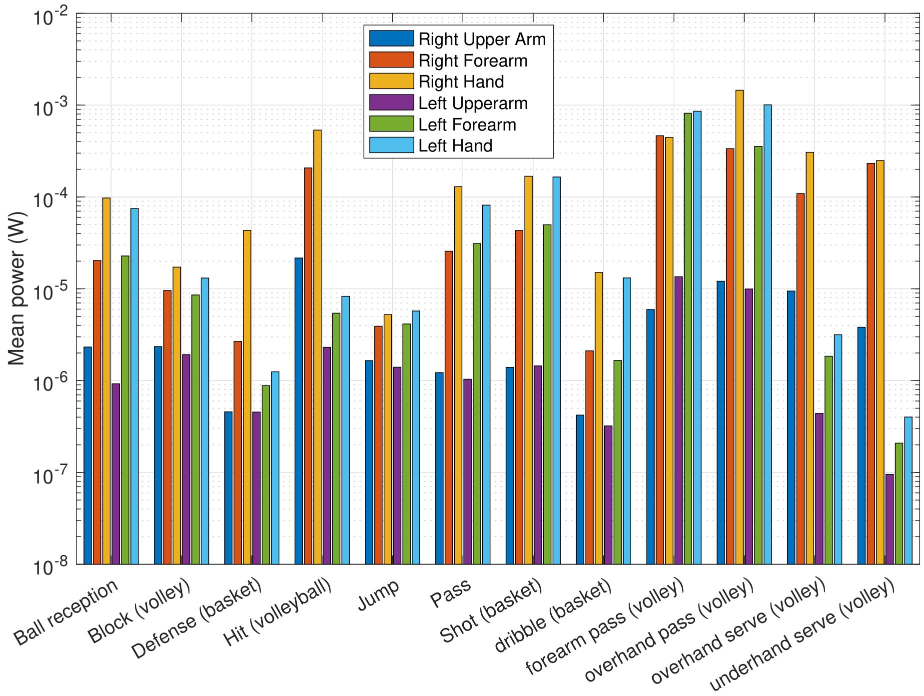

Figure 3.15 – Mean power prediction in logarithm scale for some body locations according to performed activities.

The logarithm scale allows a better representation of the lowest values. One must keep in mind that some activities produce 1000 more power than others. For example, on the right hand, the harvester model predicted 100 times more power production for the overhead pass (volley) than for the jump. In addition, it is shown that the best power prediction is obtained for the activity 'overhand pass (volley)' for the right hand (value used for normalization). Regarding the overall result, the best power prediction is obtained for limbs extremities and for activities that induce large impacts. In addition, for each location, one can observe the optimal orientation according to the performed activities. Figure 3.16 presents the orientations of the harvester for the right hand according to the performed activities. Depending on the activity, the optimal orientation of the harvester differs. The rotation angles are expressed in the accelerometer local frame, for each location the sensor are placed in the same way, we recall: the x-axis of the sensors was aligned with the length of the segments; the y-axis was aligned with the thickness of the segments; and the z-axis was aligned with the outgoing normal direction.

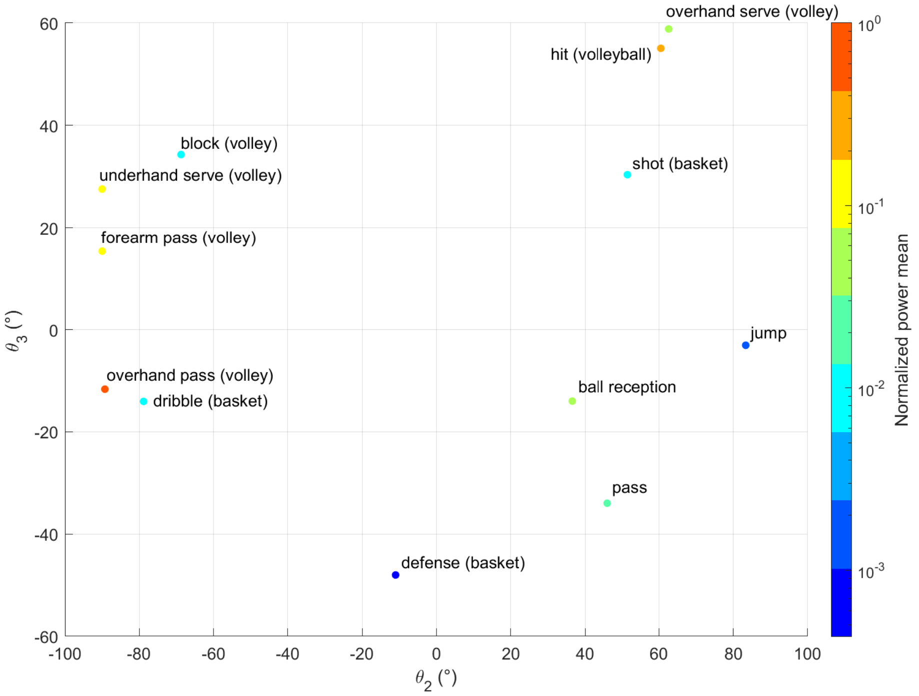

Figure 3.16 – Optimal harvester orientation for the right hand according to performed activities and normalized mean power prediction.

3.3.5 Limitations & Future Studies

The performed actions could have impacted the results, as the results were based on accelerometer data and harvester parameters. However, identifying impacts as MRFs is relevant, as they are representative of sports activity. Some aspects, such as IMU sampling frequency, can give a better interpretation of the optimal placement. It was seen that impacts can present many frequencies. Thus, increasing the sampling frequency could make a better acquisition of the possible dynamics. In addition, it enables the model to be simulated with smaller time steps and prediction precision to be improved. The method could be used to quantify the available power using the model to design sensors for various applications. Additionally, the number of vibration modes to simulate the model must be considered, especially if the acceleration frequencies are close to the mode frequencies.

Acceleration data can be biased due to soft tissue artifacts. Indeed, skin or muscles can add relative movement, depending on the robustness of the fixations. Moreover, impacts can be slightly absorbed or dampened by these tissues. However, the experiments were conducted with acquisition devices mounted on a real person in the way harvesters could be. The generators can be attached in the same way as the IMUs. Indeed, they have the same mass and a similar size. Typically, in the Xsens MVN Link combination used to generate data, the IMUs are in plastic cases attached to the human body by self-gripping strips. Thus soft tissue artifacts and other defects in the transmission of motion from the human body to the sensor or the energy recovery device are similar.

Concerning the harvester, the mechanical limits of the beam were not considered. An excessive acceleration value could induce a very large deflection in the beam, causing damage that could lead to loss of performance and eventually to the destruction of the device. Some applications defer the use of casings designed to mechanically limit deflection. Thus, the maximum voltage could be deducted and used in the method as a constraint.

Ergonomics aspects were not studied in this chapter. In addition, the labelling of the performed activities may be not accurate leading to errors in the activities contribution results. Nevertheless, the proposed method allows to determine the optimal configuration and to map the distribution of the energy prediction accordingly to the acceleration measurements. Tradeoffs could be drawn to obtain the best configuration under ergonomic and practical constraints. Future studies should be directed towards the ergonomic and practical validity aspects trough experiments.

In addition, the output control strategy of the harvester can be modeled to be representative of the reality. Indeed, in this study a passive control was assumed with only the use of a load resistance. Some literature discusses harvesting strategies using electrical interfaces, as an example, Morel et al. [111] present in their work a comparative study on electrical interfaces for vibrational piezoelectric harvesters.

3.4 Conclusion

This study presents a method for determining the optimal placement of cantilevered PEGs using a numerical model and experimental acceleration data from sports movements. The assumptions and materials used are listed, which could later help other similar studies to be performed under the desired application conditions. The optimal placement and orientation of a cantilevered PEG were assessed. The results show that in the current application, the axis normal to the surface of the right hand was the optimal placement. Extremity segments such as the feet, hands, and upper lower arms were identified as better energy sources. The predicted energy for the foot locations is about 50% of the predicted energy for the right hand location. In general, upper arm and leg locations correspond to less than 20% of the predicted energy of the right hand location.

Impacts, among the acceleration data, were identified as relevant features for operating the harvester. Indeed, for the most promising locations, at least 80% of the predicted energy is due to the impacts. They can be highly representative of the available energy sources. The MRFs can be good indicators to quickly determine the variables of interest for qualitative energy source assessment. This method offers more flexibility and ease for the determination of energy sources. There are many databases composed of inertial data (i.e., acceleration), which offer the opportunity to conduct studies on various applications in an easier way. However, when it comes to accurately quantifying simulated values, it is necessary to consider the experimental conditions to evaluate the quality of the measured acceleration data.

Future studies could focus on the experimental analysis of energy sources. The experimental method is challenging and cumbersome, because it requires high-precision instruments (high-impedance analyzers) and body instrumentation. As opposed to the use of IMUs, the range of possible actions and flexibility are reduced.

Chapter 4

OPTIMIZATION: IMU POSITIONING AND GEOMETRY OF CANTILEVERED PIEZOELECTRIC HARVESTER

This chapter discusses the optimization of the parameters from the previous studies' introduced in chapters 2 and 3. The first part is dedicated to the optimal positioning of the IMUs on the human body to perform HAR. We proposed an optimization problem formulation based on the IMUs configuration, considering the HAR accuracy and the overall power consumption. The results are illustrated by Pareto fronts, trade-offs exist between HAR accuracy and IMUs power consumption. The second part on this chapter focuses on the optimization of a cantilevered piezoelectric harvester dimension. This study emphasizes the relation between the geometry of the harvester, its positioning on the human body and the optimal energy harvesting.

4.1 Part 1: Optimization of IMU positioning

4.1.1 Introduction

There are multiple parameters to setup and optimize to obtain the best HAR accuracy and the minimum power consumption when using IMUs. First, we consider that an IMU is composed of 3 different sensors (accelerometer, gyroscope and magnetometer). Each sensor can measure their physical quantities along 3 axes (x-axis, y-axis and z-axis). Let us define P the maximal number of equipped IMUs. Considering that the sensing network can be composed of a set of 1 to P on-body IMU locations with different sensor configuration (i.e., activation or not of the sensors axis with the according sensor sampling frequency).

The number of existing combinations is defined by eq. 4.1.

$$Combinations = \left[\sum_{n=1}^{S} \binom{S}{i} \left[F \sum_{k=1}^{A} \binom{A}{k} \right]^{n} + 1 \right]^{P} - 1, \tag{4.1}$$

where S is the number of sensor in an IMU (S = 3), A is the number of axis of one sensor (A = 3), P the total number of locations (i.e, same as Xsens IMU set, P = 17) and F the total number of sampling frequencies (i.e, each sensor can be set to 4 different sampling frequencies, F = 4). Calculating this equation gives a number of combinations approximatively equal to $3.8e^{74}$ (larger than the estimated number of grains of sand on earth according to Howard C. McAllister). Depending on the hardware configuration, the evaluation of all combinations by the objective functions is time consuming (i.e, for 1 second evaluation more than $1e^{67}$ years is necessary to test every possibilities). In addition, other variables such as HAR algorithm parameters can be tuned (i.e, the SVM kernel, the data segmentation method, features characteristics etc), leading to an higher number of possible combination.

The network power consumption depends on the IMU configuration, when all axis and high sampling frequency value are used the power consumption increases. Thus, it is relevant to limit the hardware energy needs before investigating energy saving and energy storage strategies.

Hence, we proposed a multi-objective optimization using an heuristic method based on evolutionary algorithm. Firstly, the problem formulation and the different parameters are described leading to the choice of the heuristic method. HAR are performed using both SVM and ANN classifiers. A power consumption model is established using a commercialized IMU characteristics. Finally, using Pareto fronts, various IMU configurations are obtained.

4.1.2 Materials and Methods

4.1.2.1 Problem formulation

The problem design variables are discrete. As the problem is based on non-linear classifiers with training based on stochastic properties the problem can be considered as non-linear. In addition, we do not have access to the analytical formulation (i.e. the problem can be seen as a black box), we do not have access to derivatives, it is necessary to adopt a gradient-free method. Thus, it is natural to adopt a problem-based formulation

[67]. Popular approach is based on evolutionary algorithms. Thus, within the constraints and parameters of the problem, the genetic algorithm is selected.

To reduce the problem dimensionality some of the variables will be defined as fixed hyperparameters. The selected design variables are listed in Table 4.1.

Table 4.1 – Problem design variables.

	Type	**Description**
P	Variable	Number of selected IMUs in the sensor network (and their corresponding location).
F	Variable	Sampling frequency of the IMUs sensors. For each selected IMU, 4 sampling frequencies is defined for all the three sensors individually (accelerometer, gyroscope and magnetometer)
As	Variable	Axis selection of the IMUs sensors. For all axis of the three sensors of the IMUs (9 in total), The axes of the 3 sensors of each IMU can be activated or not.

Thus, the problem can be written as:

$$
\begin{aligned}
\underset{P,Fs,As}{minimize}\ f(P,Fs,As) &= \begin{bmatrix} f_1(P,Fs,As) \\ f_2(P,Fs,As) \end{bmatrix} \\
f_1(P,Fs,As) &= \begin{cases} \text{errorSVM}(P,Fs,As), & \text{if SVM} \\ \text{errorNN}(P,Fs,As), & \text{if NN} \end{cases} \\
f_2(P) &= \sum_{i=1}^{P} p^i_{imu}(Fs,As)
\end{aligned} \tag{4.2}
$$

where ERRORSVM() and ERRORNN() correspond respectively to the error evaluation function of SVM and ANN classifiers presented in the next section. $p_{imu}()$ is the function giving the power consumption of the selected IMU network according to its configuration.

In addition, it is interesting in multi-objective optimization to visualize the optimal Pareto front distribution. The proposed resolution workflow structure is shown in Figure 4.1. It consists in evaluating IMU networks distributed over the human body. The multi-objective optimization will evaluate IMU networks using their power consumption through a model and their relevance for HAR through classifiers performance. For each selected IMU network, the corresponding data are extracted from the dataset and then processed to feed the classifiers.

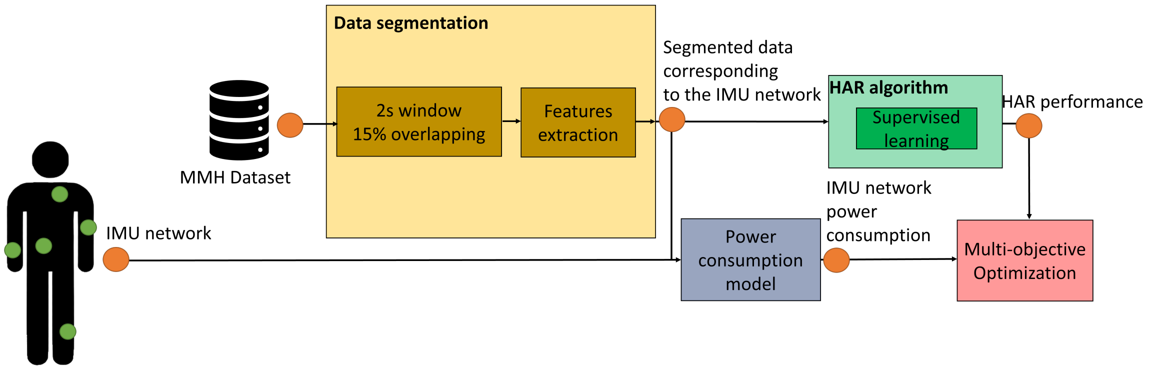

Figure 4.1 – Workflow of the multi-objective optimization approach.

4.1.2.2 Database

The evaluation method is based on the online available dataset entitled "Manual Material Handling Dataset for Biomechanical and Ergonomics Analysis" [112]. The dataset is composed of Manual Material Handling (MMH) and isokinetic activities [113]. Data were captured by the Xsens motion capture system (Xsens Technologies B.V) [114] and electromyography devices. To conduct this study, only the bimanual trials and Xsens motion capture data of MMH activities for all subjects are considered (1.7 GB of data with 8 bytes precision). 14 participants were involved, the activities are carried out with handled loads of 2, 8 and 12 kg, there are 3 trials per load. The labels of performed activities and the total number of repetitions are presented in Table 4.2.

Table 4.2 – Activities labels and description according to the MMH dataset. The activities consist in moving a box.

Label	**Activity description**	**Total number of repetitions**
N	N-pose	717
LF	Lift from the floor	353
K	Keep Lifted	126
PT	Place on the table	353
LT	Lift from the table	242
W	Carry	242
PF	Place on the floor	242

Xsens motion capture system

The Xsens motion capture system is based on 17 IMUs located at the head, sternum (T8), both shoulders, both upper-arms, both forearms, both hands, pelvis, both feet, both upper-legs and both lower-legs. The system sampling frequency was set to 240 Hz and the range of the accelerometers and gyroscopes were respectively ± 160 m/s^2 and ± 2000 °/s. Data provided by the MMH dataset and the Xsens output files give the sensors free acceleration, the sensors magnetic field and the sensors orientation quaternion. To obtain the angular velocities (i.e., values from the gyroscopes), the quaternions are expressed in the corresponding Euler sequences derivated from the angles. The free acceleration, the angular velocity and the magnetic field data are used. Raw values from sensors are not used directly but still this limitation allows to demonstrate the multi-objective approach with high-dimensional evaluation space. Future studies will focus more on synthesized data from skeleton model with soft tissues artifacts or rigid body segment assumptions.

4.1.2.3 HAR algorithm

To perform HAR, both classical SVM and ANN approaches are investigated [115, 116]. This illustrates the possibilities of using different types of classification methods. First of all, the data are normalized by the sensors full range of measurement (respectively ± 160 m/s^2 and ± 2000 °/s for accelerations and angular velocities) to obtain an equal contribution for future features extraction. Using a sliding window method, data are segmented by a 2 s window with 15 % overlapping. Then, features are extracted from the segmented data using the **hctsa** Matlab software package [117]. 22 features are used corresponding to the hctsa features set called "catch22" (CAnonical Time-series CHaracteristics, extracted from [118]). Temporal data are not directly used as they increase the complexity of classifiers and their processing time will take longer as the dimensionality is higher. The HAR algorithms' inputs consist in arranging the axes (2 s of data window or extracted features for each axis) of each sensor of each IMU one after the other and respecting the following order: accelerometer, gyroscope and magnetometer. The arrangement sequence remains the same independently from selected configurations (i.e., if the axes are activated or not). The Figure 4.2 illustrates the HAR input data structure with such arrangement. The dataset is divided into a training and validation set. Training data is randomly selected using a ratio of 0.8. Thus, validation data represents 20 % of the dataset. To average the prediction errors, HAR algorithms are trained 10 times[1] (here a training consists in training and evaluating the classifier on a randomly divided data set.).

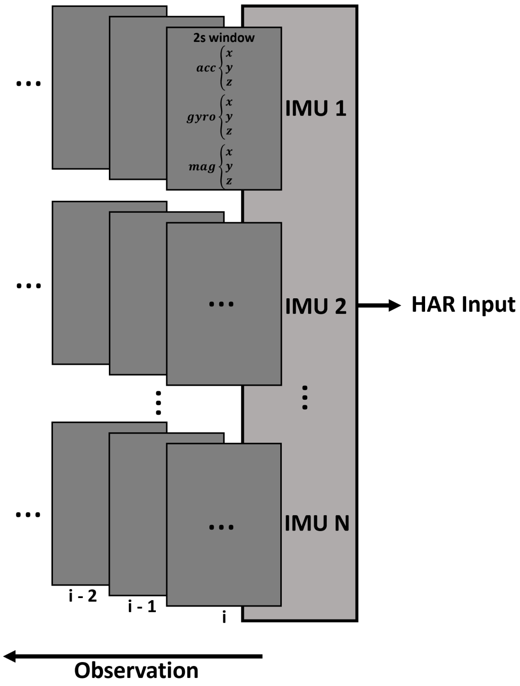

Figure 4.2 – Input data structure for one HAR algorithm training. Observations correspond to 2s window of extracted features for each sensor axis. N represents the number of selected IMUs and i the number of observation.

Suport Vector Machine (SVM)

We defined the SVM models kernel as a second order polynomial kernel. To evaluate the classifier performance, the missclassification rate is computed using:

$$\text{errorSVM}(x) = \sum_{j=1}^{N} w_j I\{\hat{y_j}(x) \neq y_j\}, \tag{4.3}$$

where w_j is the weight for observation j, $I\{.\}$ is the indicator function, y_j is the observed class label, $\hat{y_j}$ is the predicted class label, N is the number of observation and x the design variables.

---

[1] Increasing the training number will limit the prediction 'noise' but increase the computation time.

Artificial neural network

To perform HAR using neural network, the structure presented in Figure 4.3 is used.

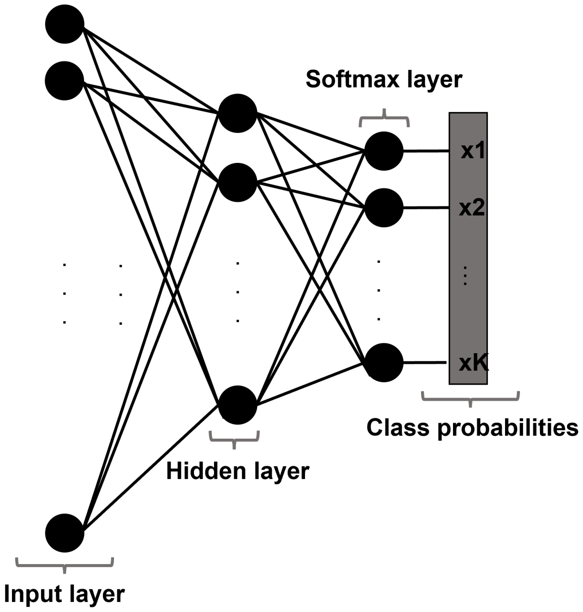

Figure 4.3 – Neural network structure for data classification. The input layer size depends on the selected IMU network configuration. The unique hidden layer contains 10 neurons and the softmax layer 7 neurons corresponding to the number of classes (K). The network is fully connected.

The artificial neural network is build on Matlab R2022b with the function PATTERNNET() [119]. The performance of the neural network is computed using the crossentropy defined by:

$$\text{errorNN}(x) = -\frac{1}{N}\sum_{n=1}^{N}\sum_{k=1}^{K} T_{nk}\ln(Y_{nk}(x)), \tag{4.4}$$

where N is the number of observation, K is the number of classes, T_{nk} is the corresponding target class value to Y_{nk} and x the design variables.

4.1.2.4 Power consumption model

To established a power consumption model of the IMUs, electrical characteristics of commercialized devices are employed. The studied power consumption model is based on the LSM9DS1 [2]. The Table 4.3 presents the power consumption for the different operating modes (IMU voltage supply = 3.3 V).

Table 4.3 – Power consumption of the IMU sensors for different operating modes

Power consumption (mW)	**Sampling frequency (Hz)**			
	14.9	***59.5***	***119***	***240***
Accelerometer	0.99	0.99	0.99	0.99
Gyroscope	5.28	6.93	9.24	13.2
Magnetometer	0.99	0.99	0.99	0.99

In addition, to adapt the operating point of the sensors, data are resampled before the segmentation step accordingly to the choosen sampling frequency using the Matlab function RESAMPLE().

4.1.2.5 Multi-objective optimization

Trade-offs between HAR performance and IMU network power consumption are illustrated by the Pareto front using the Matlab function GAMULTIOBJ(), it is based on the NSGA-II algorithm [69]. This function computes a genetic algorithm multi-objective optimization. Defaults parameters are used and the population size is set to 200. As a reminder, genetic optimization principle is presented in chapter 1.

Population generation

Individuals are composed of multiple characteristics such as the location of the IMU set on the human body, the activation of the sensor axes and the sampling frequencies. Table 4.4 gives an example of a potential individual who has 5 IMUs.

Characteristics are initially chosen with an uniform distribution probability. Table 4.5 presents the number associated to the body locations.

---

[2] iNEMO inertial module `https://cdn.sparkfun.com/assets/learn_tutorials/3/7/3/LSM9DS1_Datasheet.pdf`

Table 4.4 – Example of a potential individual in the population. The location number corresponds to a body location (see table 4.5). Acc: accelerometer; Gyro: gyroscope; Mag: Magnetometer.

Location	**Axis activation**			**Sampling Frequency**		
	Acc. xyz	***Gyro. xyz***	***Mag. xyz***	***Acc***	***Gyro***	***Mag***
1	1 1 1	0 1 0	1 0 0	240	59.5	119
4	0 0 1	0 1 0	1 0 1	119	59.5	119
10	1 0 1	0 1 0	0 1 0	119	119	119
16	0 0 0	0 1 0	1 0 0	240	59.5	14.9
17	0 1 1	1 1 1	1 0 1	14.9	59.5	240

Table 4.5 – IMU locations on the body with their associated number.

Number	**Body location**
1	Pelvis
2	T8
3	Head
4	Right Shoulder
5	Right Upper Arm
6	Right Forearm
7	Right Hand
8	Left Shoulder
9	Left Upper Arm
10	Left Forearm
11	Left Hand
12	Right Upper Leg
13	Right Lower Leg
14	Right Foot
15	Left Upper Leg
16	Left Lower Leg
17	Left Foot

Cross-over

Cross-over creates children from parents for the next population generation. In this framework, cross-over is computed by merging two individuals characteristics chosen randomly. The next population is composed of 80 % of children from the cross-over. Thus, some locations and their associated configurations from selected parents are merged. This is illustrated in table 4.6.

Table 4.6 – Example of generated child. In green, the first parent characteristics and in red the second. Parent characteristics are selected randomly.

Location	**Axis activation**			**Sampling Frequency**		
	Acc. (xyz)	***Gyro. (xyz)***	***Mag. (xyz)***	***Acc***	***Gyro***	***Mag***
5	1 1 1	0 1 0	1 0 0	119	59.5	119
4	0 0 1	0 1 0	1 0 1	119	59.5	119
10	1 0 0	0 1 0	0 0 0	119	119	240
16	0 1 0	0 1 0	1 1 1	240	59.5	119
12	0 0 1	1 1 1	1 0 1	14.9	59.5	14.9

Mutation

The mutation consists in altering some characteristics randomly. Following a uniform probability distribution, one characteristic are altered with a new value. For example, the location, a sensor sampling frequency or an axis activation. The next population is composed of 20 % of children from the mutation.

4.1.2.6 Trivial extremum investigation

Power consumption are easy to estimate, thus, the extreme values are investigated. The obtained results will be used as comparison references. The following configurations are evaluated:

- (C1) Maximal power consumption: All IMUs with maximum resolution mode (240 Hz);
- (C2) Minimal power consumption: One sensor with only one axis with minimal resolution mode (14.9 Hz). There are P.S.A ($17 \cdot 3 \cdot 3 = 153$) possibilities, they are all exhaustively evaluated, we keep the configuration with the best HAR accuracy. There are 1-axis sensors that consume less power than a 3-axis sensor, so we consider that for the C2 configuration the power consumption is less than 0.99 mW.

4.1.3 Results

4.1.3.1 Trivial extremum configurations

Using the introduced HAR algorithms, the extremum configuration are investigated. Figure 4.4 presents the confusion matrices obtained for one training for the configuration C1.

Confusion matrix

In supervised learning, the confusion matrix corresponds to the performance evaluation of a classification problem. The rows (output class) correspond to the class predicted by the classifier and the column corresponds to the true class (target class) of the classification problem.

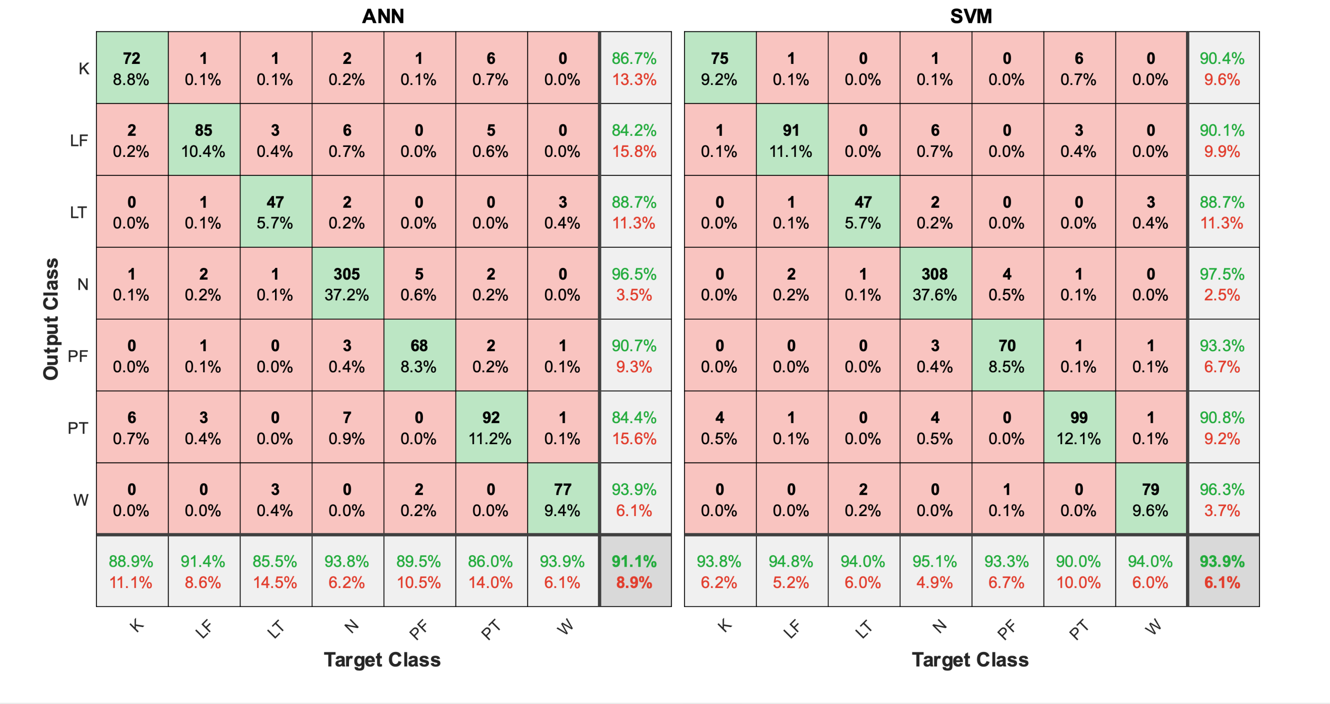

ANN

Output Class \ Target Class	K	LF	LT	N	PF	PT	W	
K	72 8.8%	1 0.1%	1 0.1%	2 0.2%	1 0.1%	6 0.7%	0 0.0%	86.7% 13.3%
LF	2 0.2%	85 10.4%	3 0.4%	6 0.7%	0 0.0%	5 0.6%	0 0.0%	84.2% 15.8%
LT	0 0.0%	1 0.1%	47 5.7%	2 0.2%	0 0.0%	0 0.0%	3 0.4%	88.7% 11.3%
N	1 0.1%	2 0.2%	1 0.1%	305 37.2%	5 0.6%	2 0.2%	0 0.0%	96.5% 3.5%
PF	0 0.0%	1 0.1%	0 0.0%	3 0.4%	68 8.3%	2 0.2%	1 0.1%	90.7% 9.3%
PT	6 0.7%	3 0.4%	0 0.0%	7 0.9%	0 0.0%	92 11.2%	1 0.1%	84.4% 15.6%
W	0 0.0%	0 0.0%	3 0.4%	0 0.0%	2 0.2%	0 0.0%	77 9.4%	93.9% 6.1%
	88.9% 11.1%	91.4% 8.6%	85.5% 14.5%	93.8% 6.2%	89.5% 10.5%	86.0% 14.0%	93.9% 6.1%	91.1% 8.9%

SVM

Output Class \ Target Class	K	LF	LT	N	PF	PT	W	
K	75 9.2%	1 0.1%	0 0.0%	1 0.1%	0 0.0%	6 0.7%	0 0.0%	90.4% 9.6%
LF	1 0.1%	91 11.1%	0 0.0%	6 0.7%	0 0.0%	3 0.4%	0 0.0%	90.1% 9.9%
LT	0 0.0%	1 0.1%	47 5.7%	2 0.2%	0 0.0%	0 0.0%	3 0.4%	88.7% 11.3%
N	0 0.0%	2 0.2%	1 0.1%	308 37.6%	4 0.5%	1 0.1%	0 0.0%	97.5% 2.5%
PF	0 0.0%	0 0.0%	0 0.0%	3 0.4%	70 8.5%	1 0.1%	1 0.1%	93.3% 6.7%
PT	4 0.5%	1 0.1%	0 0.0%	4 0.5%	0 0.0%	99 12.1%	1 0.1%	90.8% 9.2%
W	0 0.0%	0 0.0%	2 0.2%	0 0.0%	1 0.1%	0 0.0%	79 9.6%	96.3% 3.7%
	93.8% 6.2%	94.8% 5.2%	94.0% 6.0%	95.1% 4.9%	93.3% 6.7%	90.0% 10.0%	94.0% 6.0%	93.9% 6.1%

Figure 4.4 – Confusion matrices of NN and SVM models for configuration C1. The average value of error using 10 training is respectively 0.0747 and 0.0494 for SVM and NN.

The IMU network power consumption is equal to 123.42 mW. ANN model shows 91.1 % accuracy and SVM model show 93.9 % accuracy.

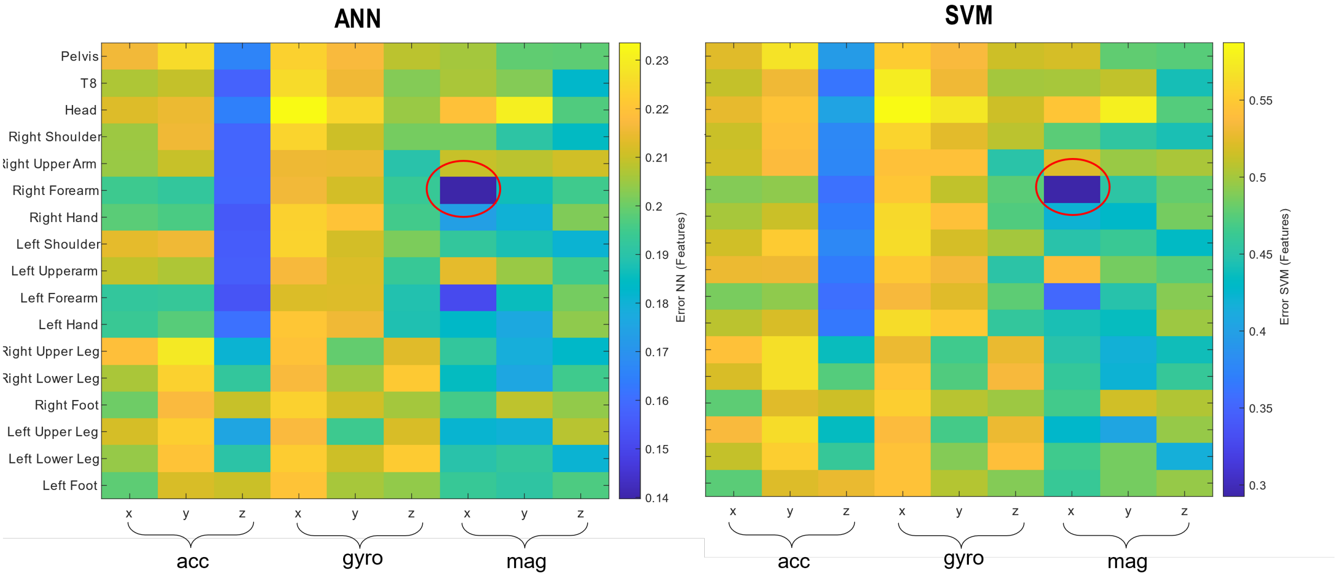

Figure 4.5 – Error of NN and SVM models for the configuration C2. Error values were computed using an average of 10 training. In the red circles are the best candidates for the configuration C2: IMU located on the right forearm and using only the x-axis of the magnetometer.

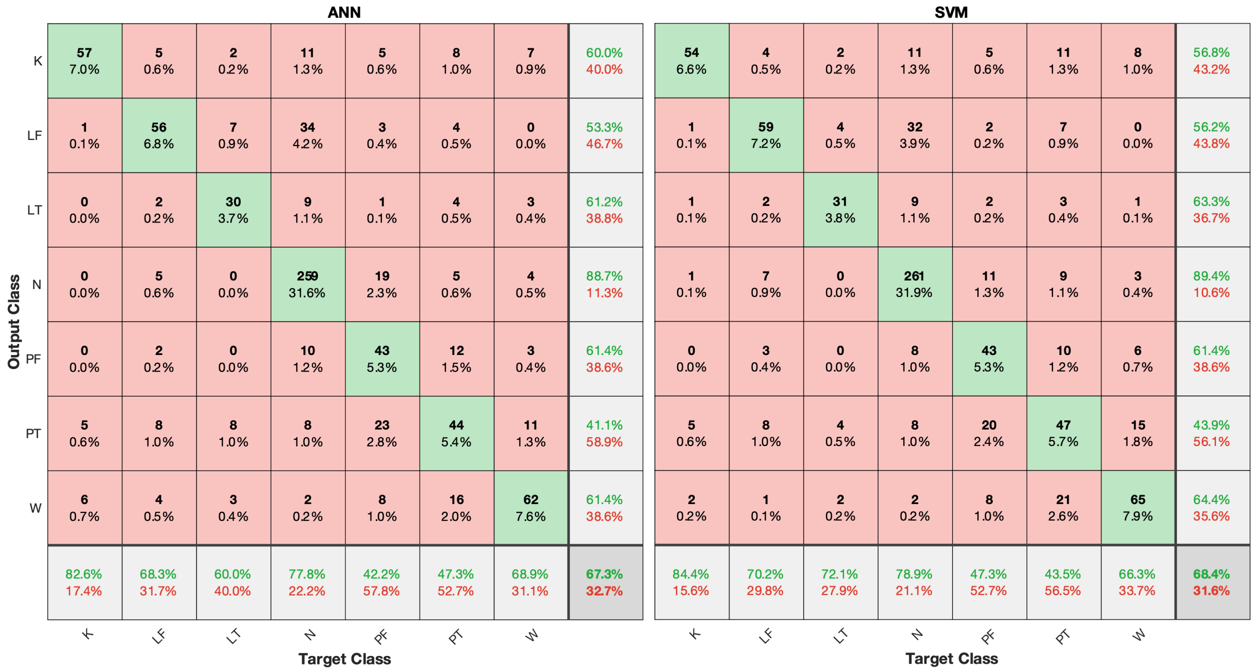

ANN

Output Class	K	LF	LT	N	PF	PT	W	
K	57 7.0%	5 0.6%	2 0.2%	11 1.3%	5 0.6%	8 1.0%	7 0.9%	60.0% 40.0%
LF	1 0.1%	56 6.8%	7 0.9%	34 4.2%	3 0.4%	4 0.5%	0 0.0%	53.3% 46.7%
LT	0 0.0%	2 0.2%	30 3.7%	9 1.1%	1 0.1%	4 0.5%	3 0.4%	61.2% 38.8%
N	0 0.0%	5 0.6%	0 0.0%	259 31.6%	19 2.3%	5 0.6%	4 0.5%	88.7% 11.3%
PF	0 0.0%	2 0.2%	0 0.0%	10 1.2%	43 5.3%	12 1.5%	3 0.4%	61.4% 38.6%
PT	5 0.6%	8 1.0%	8 1.0%	8 1.0%	23 2.8%	44 5.4%	11 1.3%	41.1% 58.9%
W	6 0.7%	4 0.5%	3 0.4%	2 0.2%	8 1.0%	16 2.0%	62 7.6%	61.4% 38.6%
	82.6% 17.4%	68.3% 31.7%	60.0% 40.0%	77.8% 22.2%	42.2% 57.8%	47.3% 52.7%	68.9% 31.1%	**67.3%** **32.7%**

Target Class

SVM

Output Class	K	LF	LT	N	PF	PT	W	
K	54 6.6%	4 0.5%	2 0.2%	11 1.3%	5 0.6%	11 1.3%	8 1.0%	56.8% 43.2%
LF	1 0.1%	59 7.2%	4 0.5%	32 3.9%	2 0.2%	7 0.9%	0 0.0%	56.2% 43.8%
LT	1 0.1%	2 0.2%	31 3.8%	9 1.1%	2 0.2%	3 0.4%	1 0.1%	63.3% 36.7%
N	1 0.1%	7 0.9%	0 0.0%	261 31.9%	11 1.3%	9 1.1%	3 0.4%	89.4% 10.6%
PF	0 0.0%	3 0.4%	0 0.0%	8 1.0%	43 5.3%	10 1.2%	6 0.7%	61.4% 38.6%
PT	5 0.6%	8 1.0%	4 0.5%	8 1.0%	20 2.4%	47 5.7%	15 1.8%	43.9% 56.1%
W	2 0.2%	1 0.1%	2 0.2%	2 0.2%	8 1.0%	21 2.6%	65 7.9%	64.4% 35.6%
	84.4% 15.6%	70.2% 29.8%	72.1% 27.9%	78.9% 21.1%	47.3% 52.7%	43.5% 56.5%	66.3% 33.7%	**68.4%** **31.6%**

Target Class

Figure 4.6 – Confusion matrices of NN and SVM models for configuration C2. Results were obtained using only the IMU located on the right forearm using the x-axis of the magnetometer. These confusion matrices correspond to the lowest values obtained in Figure 4.5.

Figure 4.5 presents the classification error for the configuration C2. The best location to minimize the classification error when using the minimal consumption configuration C2 (<0.99 mW) is the right forearm using the x-axis of the magnetometer. Note that the z-axis of accelerometers located on the upper body has a small classification error. The z axis is the axis oriented along the normal direction of the segments. The corresponding confusion matrices is presented in Figure 4.6. ANN model show 67.3 % accuracy and SVM model show 68.4 % accuracy. Using all the IMUs gives better performance but increases drastically the power consumption. Thus, maximal and minimal power consumption with their associated performance were investigated.

4.1.3.2 Pareto fronts

The multi-objective optimization problem presented previously is computed using genetic algorithm. The results are presented using Pareto fronts. Figure 4.7 shows the objectives functions evaluations and the non-dominated point corresponding to the Pareto front using NN classifier. The Pareto front gives the optimal solutions illustrated by the trade-offs between the network power consumption and the HAR classifier error. The obtained results can then be processed to determine the preferred configuration. Figure 4.8 presents the distribution of the IMUs on the human body with the corresponding number of activated axis for some Pareto solutions. The distribution and configuration of the IMU network along the human body is different for each Pareto front solutions. The table 4.7 presents the detailed configuration of the solutions obtained from the Figure 4.8. In this optimization, the algorithm limited the use of the gyroscope as it is the most greedy in power consumption. Some IMU locations are recurrent such as the right forearm or the left forearm. Table 4.8 presents the corresponding classification score obtained.

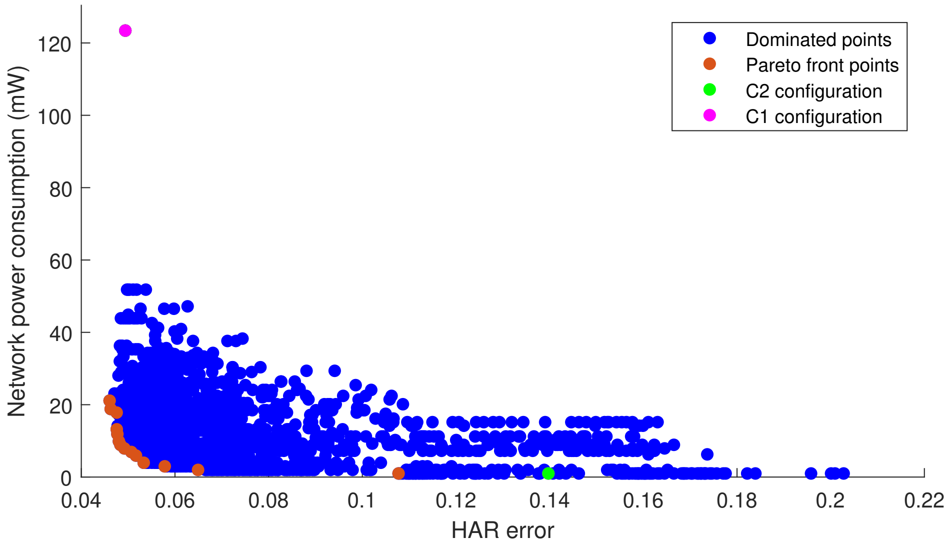

Figure 4.7 – Objectives functions evaluations using genetic algorithm. The Pareto front is illustrated by red dots. The configuration C1 is in magenta and the configuration C2 is in green.

Table 4.8 – Classification score (mean ± std) obtained for NN and SVM classifiers using 300 trainings. The values correspond to the solutions presented in Figure 4.8 and configuration C1. The corresponding power consumption is displayed.

Solution	**NN score (%)**	**SVM score (%)**	**Power consumption (mW)**
a	88.74 ± 3.3	91.80 ± 0.9	17.82
b	88.09 ± 4.5	91.62 ± 0.8	7.92
c	73.25 ± 2.1	79.97 ± 1.3	0.99
C1	89.69 ± 4.35	92.45 ± 0.83	123.42
C2	66.05 ± 1.82	70.86 ± 1.32	<0.99

In our application, the SVM classifier shows better results. Overall, the classification scores tends to the results obtained in the C1 configuration and are higher than configuration C2. The power consumption is lower than configuration C1 but higher than configuration C2. As the starting points of the genetic algorithm are generated randomly, the final result can differ from optimization computations. In addition, the classifiers training dataset are randomly divided leading to dispersion of error values. Figure 4.9 presents Pareto fronts obtained from 2 different runs of the optimization computations.

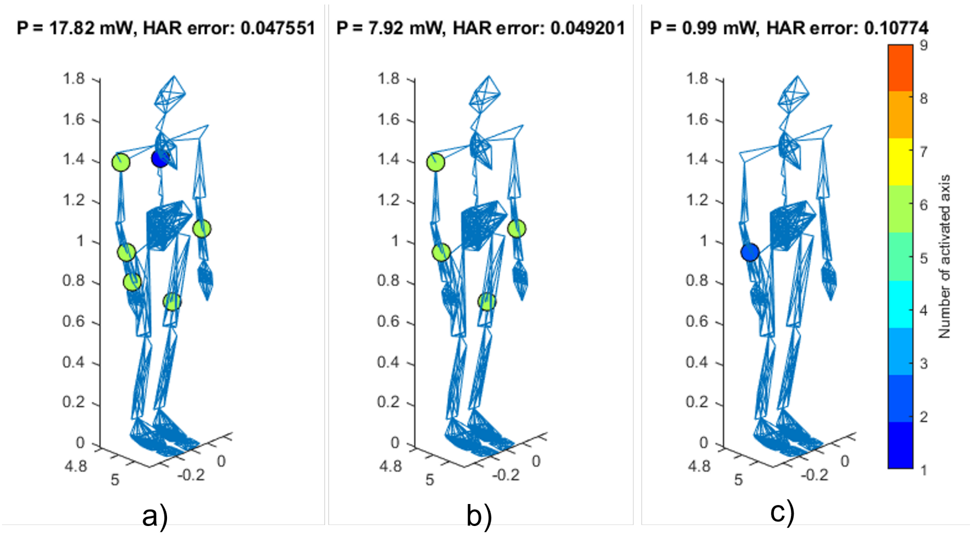

a)

b)

c)

Figure 4.8 – Example of Pareto front solutions obtained from the multi-objective optimization and NN classifier. The resulting configurations of the IMUs a), b) and c) are presented in table 4.7.

Table 4.7 – Example of Pareto front solutions obtained from the multi-objective optimization. The first group color corresponds to the solution a), the second to the solution b) and the last to the solution c).

Location	**Axis activation**			**Sampling Frequency (Hz)**		
	Acc. (xyz)	**Gyro. (xyz)**	**Mag. (xyz)**	**Acc.**	**Gyro.**	**Mag.**
2	100	000	000	240	14.9	240
6	110	011	110	119	59.5	14.9
7	111	000	111	240	119	119
10	111	000	111	240	119	59.5
15	111	000	111	240	119	240
4	111	000	111	240	119	240
6	111	000	111	59.5	119	14.9
10	111	000	111	240	119	59.5
4	111	000	111	240	119	240
15	111	000	111	240	119	240
6	101	000	000	240	240	59.5

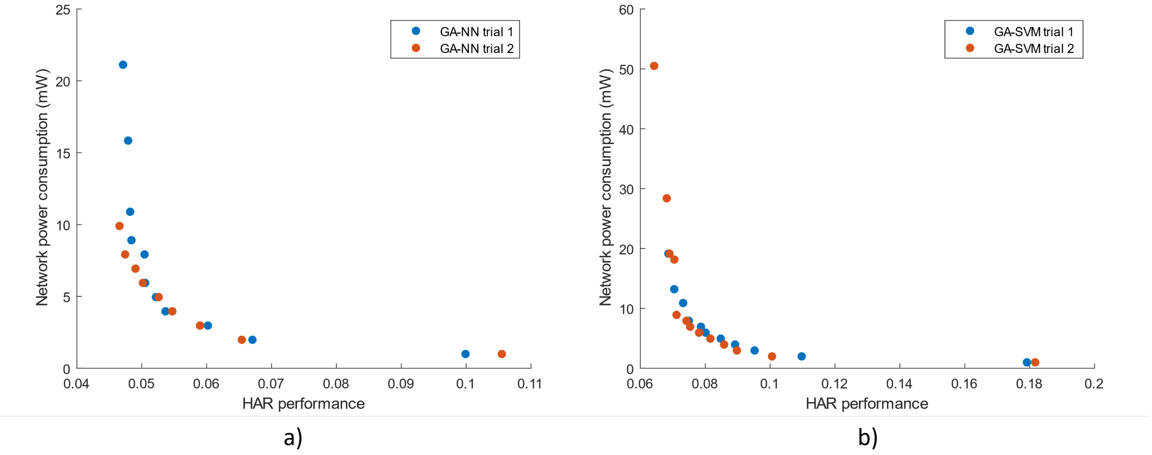

Figure 4.9 – Pareto front obtained from different optimization computations using a) NN classifier and b) SVM classifier.

The obtained Pareto fronts are close to each other but the solutions can differ.

4.1.4 Discussion

This first part of chapter 4 proposed a method based on a multi-objective optimization problem for determining the best location of IMUs on the human body for HAR. Maximum classification accuracy and minimum power consumption are defined as objectives. Problem definition and design variables characteristics lead to the use of a genetic algorithm. However, there is no unique solution to this engineering problem. Several configurations could be suitable for the targeted applications. Existing trade-offs are investigated using optimal Pareto fronts.

In the first step, the natural solutions to the problem illustrated by configuration C1 and C2 are investigated. These configurations present the classification accuracy with minimal and maximal power consumption configuration. Using all the IMU locations with maximum resolution mode (maximum sampling frequency) gives the best classification accuracy (> 90 %) but drastically increases the power consumption at maximum level. Using the minimum power consumption (i.e. one location and one axis only with low resolution mode) configuration gives low classification accuracy (< 70 %). This last solution consumes 124 times less power than C1.

In a second step, to explore the existing trade-offs between classification accuracy and power consumption the genetic algorithm is computed. Optimal solutions are represented on the Pareto front, multiple configurations exist. Investigated solutions show different IMU network distribution over the human body with their respective classification accuracy and power consumption. In addition, the determination of the best configuration also depends on the ergonomic constraints, this aspect is not investigated here. While the classification accuracy tends to the C1 configuration, the computed power consumption is reduced. Nevertheless, the stochastic character of the problem influences the final results by inducing a "noise". By averaging the errors from the various classifier training this phenomenon is reduced but is still present.

Nevertheless, the results depend not only on the power consumption model but also on the classification parameters such as the data segmentation or even the features. Other consideration is the computational cost, adding parameters will increase the problem complexity. Concerning the genetic algorithm, the obtained solutions can be improved by increasing the population size or the mutation ratio and method. The genetic algorithm optimization tends to global maxima (or minima) solutions, in our study the Pareto fronts converged towards it with various solutions. Indeed, as illustrated in Figure 4.9, multiple optimizations gave multiple closed Pareto fronts. Our study was limited by computational cost, as an example, with the current design variables and defined parameters the optimization execution time was approximately 3-5 days. Increasing the number of classifiers training reduces the 'noise' but increases drastically the computation time.

Future studies can look at other classifiers and power consumption model or can adapt some parameters to improve HAR accuracy. Crossover or mutation strategies can be modified to modulate the search in the solution space. In addition, studies based on SID for determining the optimal IMU location can be conducted, this would increase the number of possibilities.

4.1.5 Conclusion of part 1

Multiple configurations for IMU positioning on the human body exist. Nevertheless, extensive testing of all combinations is not feasible as it will take $1e^{64}$ years assuming a one-second run time for a test. It is necessary to investigate optimization method. Thus, the genetic algorithm is selected. We performed a multi-objective optimization for maximizing the HAR accuracy and minimizing the IMU network power consumption. The proposed method is promising for determining optimal solutions. Results show trade-offs between accuracy and power consumption. Nevertheless, the problem complexity easily increase which implies high computational cost.

4.2 Part 2: Optimization of cantilevered piezoelectric harvester geometry

4.2.1 Introduction

This part is based on the submitted conference abstract entitled *Hoareau, D.; Jodin, G.; Laaraibi, A.-r.A.; Prioux, J.; Razan, F.: Available Kinetic Energy Sources on the Human Body during Sports Activities: An Optimization Investigation using Cantilevered Piezoelectric Harvester Model, Eurosensors XXXIV, Italy, 2023.* Chapter 3 shows that the impacts induced by human sport activities are one of the most relevant features to operate cantilevered piezoelectric harvester. In addition, the optimal orientations of the simulated harvester on different body parts were investigated. In this part, we investigate the influence of the harvester dimensions on the simulated harvested energy.

Alameh et al. [120] investigate in their study the influence of cantilevered piezoelectric harvester geometry on the performance. The study was based on variable beam length, beam width and shape. The geometry impacts directly the performance, and results show that the T-shaped cantilever has more advantages and is relevant to a wide range of applications.

Nevertheless, the studies are generally conducted with periodic signals, when it comes to non-stationary signals such as the acceleration of the human body, the obtained results may differ. Following on from Chapter 3, this study evaluates the influence of the geometry of cantilevered piezoelectric harvester on human body accelerations. In the first part, the electromechanical model of cantilevered piezoelectric harvester and the study boundaries are defined. Then, based on methods introduced in chapter 3, the simulated harvester output power is investigated according to its dimensions.

4.2.2 Materials and methods

The study is limited to unimoprh rectangular beams without additional mass. Nevertheless, it should be kept in mind that adding mass at the end of the beam can be a common practice : it decreases the resonant frequency and thus adapts the resonator to its application. In Chapter 3, we have defined the length of the beam as L, the width as b and the thickness as h. The volume of active material is assumed constant (K), it allows to only evaluate the geometric distribution of the active layer with respect to the application.

The initial design of the harvester is the same as presented in chapter 3 (table 4.9), only L and b are defined as variables (i.e., h is constant).

Table 4.9 – Properties of the initial design of the unimorph cantilever.

Parameter	Piezoceramic	Substructure
Material	PZT	Composite
L (mm)	100	100
b (mm)	20	20
h (mm)	0.4	0.5
Tip mass	-	-
ρ_p, ρ_s (kg/m^3)	7800	7165
Y_p, Y_s (GPa)	66	100
Damping coefficient (ζ_1)	0.01	
External load (R_c)	5e6 Ohm	
d_{31} (pm/V)	-190	-
ε_{33}^S (nF/m)	15.93	-

The validity domain of the beam model is established when its transverse section is very small compared to its length [121], thus we defined the constraint presented in eq. 4.5.

$$L \geqslant 20\sqrt{b.h} \tag{4.5}$$

Using the performed sport circuit presented in chapter 3, harvester output power are evaluated on the 17 IMU locations. The Figure 4.10 presents the conducted method to evaluate the dimension influence on power prediction on the human body.

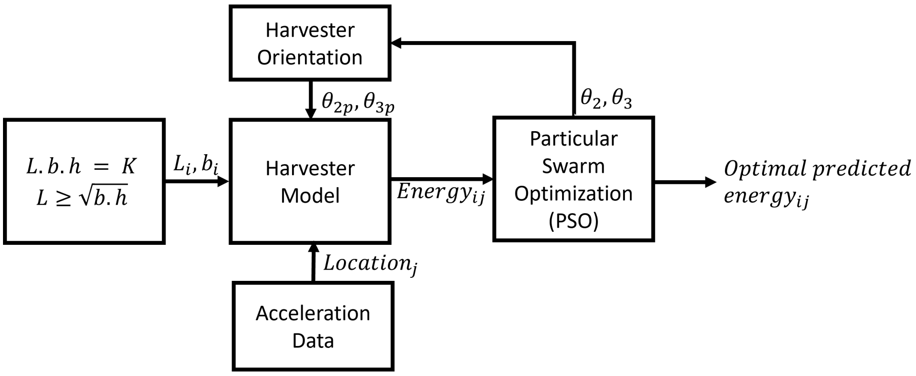

Figure 4.10 – Evaluation method of the influence of the harvester's dimensions. The harvester orientation is optimized to maximize the predicted energy.

According to eq. 4.5, numerous couples of length L and width b are evaluated. Each beam geometry is simulated to determine the predicted energy. In addition, the beam orientation on the human body locations is optimized using PSO to maximize the energy generation.

Besides, a brief sensitivity analysis is performed to compare the influence of the beam length versus the beam width. This helps to introduce ergonomics aspects, indeed, it may be better to increase for example the width than the length of the beam.

The harvester model is obtained using equation 3.7 presented in chapter 3. Because the harvester dimension impacts the resonant frequency, it might be necessary to simulate multiple vibrational modes. Thus, the harvester voltage response is expressed as illustrated in eq. 4.6.

$$V\left(p\right) = \frac{\sum_{r=1}^{N} \frac{-p\omega^2\varphi_r f_r(p)}{Z(\omega_r^2+p^2+2p\zeta_r\omega_r\omega)}}{\sum_{r=1}^{N} \frac{p\varphi_r\chi_r}{Z(\omega_r^2+p^2+2p\zeta_r\omega_r\omega)} + \frac{1+pRZ}{RZ}} \tag{4.6}$$

Where r is the mode number and N the total number of vibrational modes to be simulated. The expression of the variables can be found in chapter 3. In addition, the mechanical damping coefficients are not easy to obtain, generally experimental studies are conducted to identify their value. In the literature, we commonly find a damping ratio value of 1 % for the first mode, thus $\zeta_1 = 0.01$. The mechanical damping ratio of the vibrational modes can be modeled (eq. 4.7) using strain rate damping and viscous air damping [122].

$$\zeta_r = \frac{c_s I\omega_r}{2YI} + \frac{c_a}{2m\omega_r} \tag{4.7}$$

where c_a is the viscous air damping coefficient and c_s is the strain-rate damping coefficient. The strain-rate damping coefficient is proportional to structural stiffness and the viscous air damping coefficient is proportional to mass per unit length. In practice, it is necessary to conduct experiments to determine the value of these coefficients, it also involves knowing the natural frequencies. Another approach could be based on approximations. Khazaee et al. [123] investigated the damping mechanisms in cantilevered piezoelectric energy harvester. The results show that for a typical energy harvester structure (with a substrate shim and an epoxy bonding layer), structural damping dominates over viscous air damping, with a contribution of 75 % or more. Thus, we assumed that in the medium (here the air) the viscous air damping is negligible compared to strain-rate damping. The mechanical damping ration becomes $\zeta_r = \frac{c_s I \omega_r}{2YI}$. The value of c_s can be determined using the first mode damping value 0.01.

4.2.3 Results

As introduced in chapter 3, for simulation purposes, acceleration data are resampled by a factor 5. However, the Nyquist frequency of the acceleration data is 120 Hz, it is necessary to adapt the number of vibrational modes to be simulated in order to be representative of the dynamics present in the signals. Thus, the first three vibrational modes are simulated, using equation 4.5, 55 differents geometries are evaluated. Figure 4.11 presents the pair of beam length and width evaluated and the resonant frequencies of the vibrational modes. For the first vibrational mode (open circuit condition), the resonant frequency range is from 12.57 Hz to 57.28 Hz. Table 4.10 summarizes the frequency range of the beam geometries evaluated for vibrational mode 1 to 3. It may be noted that the resonance frequency is inversely proportional to the squared length of the beam.

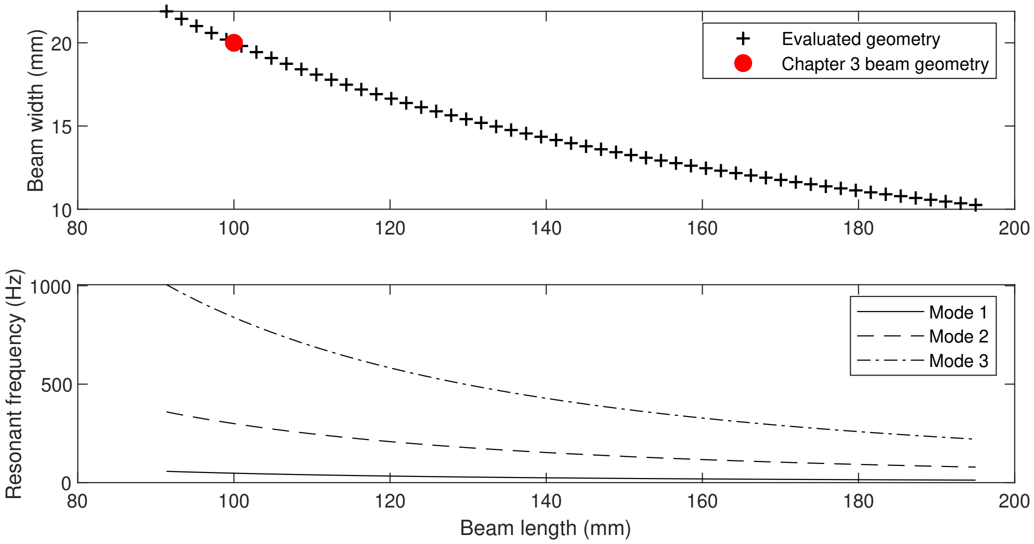

Figure 4.11 – Beam length and width used for geometry influence evaluation. In addition, the resonant frequencies of the beam for mode 1 to 3 are displayed for each geometry.

Table 4.10 – Resonant frequency range for vibrational mode 1 to 3. The lowest resonant frequencies (respectively the highest resonant frequencies) correspond to the pair L = 195 mm and b = 10.3 mm (respectively L = 91.4 mm and b = 21.9 mm).

Vibrational mode	**Lowest resonant frequency (Hz)**	**Highest resonant frequency (Hz)**
Mode 1	12.6	57.3
Mode 2	78.8	358.9
Mode 3	220.6	1005

Thus, the frequency band of the acceleration signal is represented in the frequency response of the harvester model. Figure 4.12 presents the transfer function of the harvester model for L = 195 mm and b = 10.3 mm. Using the method presented in Figure 4.10, the predicted energy of the harvester model for different geometry is computed. The best orientations are obtained using PSO with a swarm size equal to 20, the other parameters are set to Matlab default values.

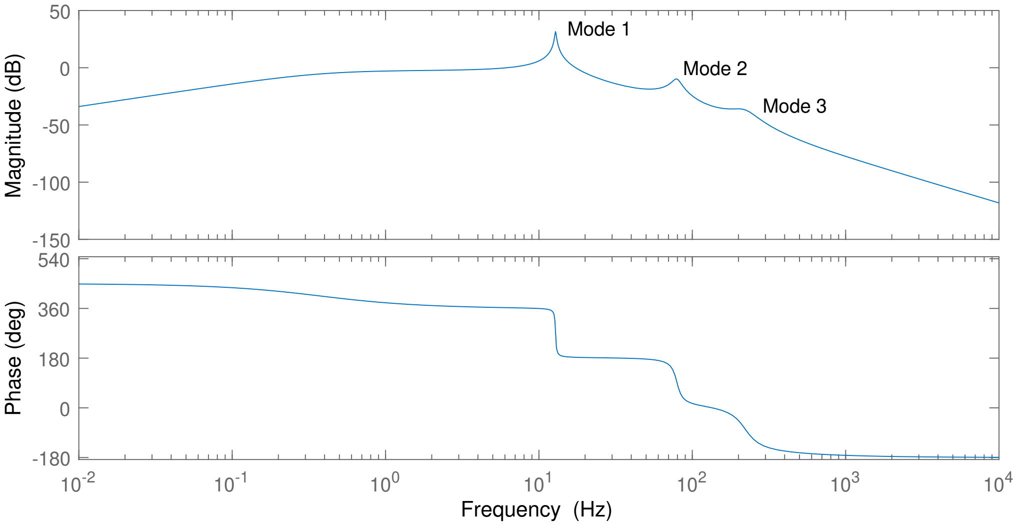

Figure 4.12 – Bode diagram of the harvester model for L = 195 mm and b = 10.26 mm. The magnitude corresponds to $V.s^2.m^{-1}$.

Figure 4.13 presents the normalized simulated energy according to the body locations and the first vibrational mode. In general, for most of the body locations, the decrease in the first mode resonant frequency increases the simulated energy. In addition, the best location to harvest energy depends on the first mode resonant frequency.

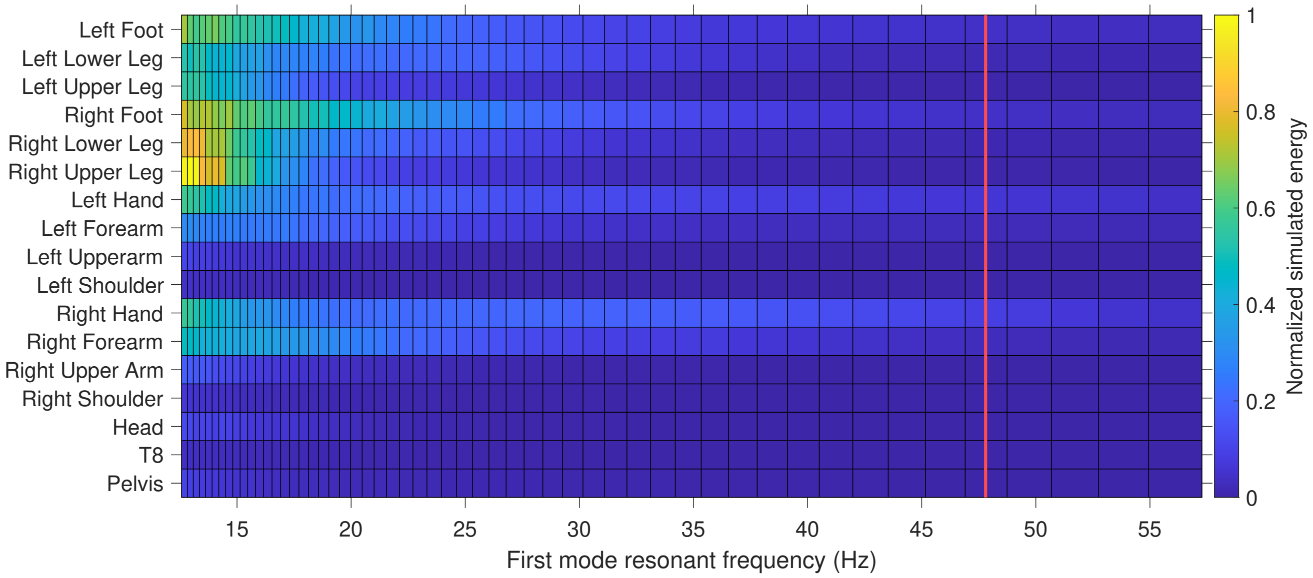

Figure 4.13 – Normalized simulated energy on body locations versus the first mode resonant frequency of the different harvester geometry. The red line represents the results obtained in chapter 3 according to the original geometry introduced in table 4.9.

In chapter 3 (red line), the harvester first mode resonant frequency was 48.8 Hz, the best location was the right hand. When the first mode operates at low frequency (< 15 Hz) the best location is on the right leg and around 10 times more energy is harvested.

Figure 4.14 presents examples of the best location to harvest energy according to the first mode resonant frequency. Each of the three results represents one of the columns from Figure 4.13, which shows the distribution of simulated energy on the human body. In this example, the best location for a first mode resonant frequency equal to 45.17 Hz is the right hand. The best location can change depending on the resonance frequencies of the harvester, for a first mode resonant frequency equal to 13.08 Hz the best location is the right upper leg. In this study, low frequency values correspond to a beam with a long length. Nonetheless, they are more constraining because more complex to be integrated. In some cases, it is easier to consider an increase in width than in length. Thus, we evaluate the sensitivity of these two parameters on the simulated energy. Table 4.11 presents a sensitivity analysis performed on the upper right leg location. This result is identified as a general result. From an initial geometry, the length and width were varied by 10 %. A variation of the width does not have much influence, indeed, in the example it represents only an increase of the energy of 0.5 %.

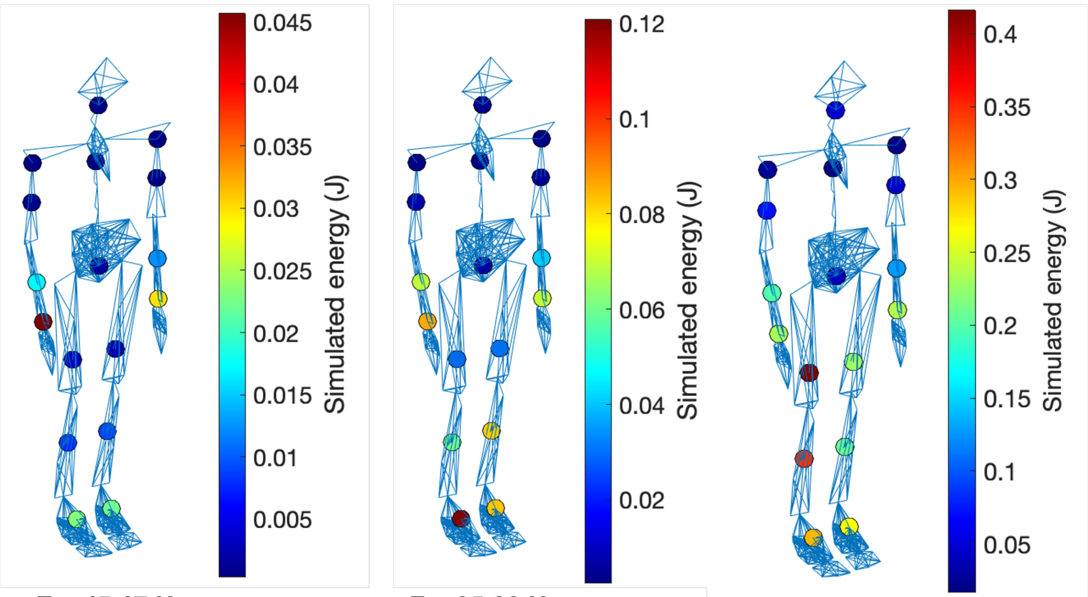

F = 45.17 Hz **F = 25.32 Hz** **F = 13.08 Hz**

Figure 4.14 – Simulated energy on body according to different harvester first mode resonant frequency. For each geometry, the greatest value of simulated energy on the human body is used to compute the normalization.

Table 4.11 – Sensitivity analysis of the parameters L and b. The initial values are L = 175.8 mm and b = 10.4 mm, the associated initial operating point of the model is 15.5 Hz for the first vibration mode. These simulated energies correspond to the location of the harvester on the upper right leg.

Energy (Initial operating point F = 15.5 Hz)	**L initial**	**L + 10 %**
b initial	254.8 mJ / 100 %	408.9 mJ / 160.5 %
b + 10 %	256.1 mJ / 100.5 %	-

By contrast, the variation in length represents a 60 % increase in energy. These results can be generalized to all the operating points studied here.

4.2.4 Discussion

In this part, we presented an evaluation of the influence of the harvester geometry on the simulated energy from human body accelerations. Using damping approximation (i.e., structural damping contribution only) and harvester orientation optimization (obtained with PSO), the model performance according to the body locations is assessed. Hence, this study highlights the feasibility of using cantilevered energy harvester for generating power.

The modification of the harvester geometry affects directly the mode resonant frequencies. As introduced before, the volume of active material is kept constant, therefore increasing the length only affects the geometry or the shape of the beam (the width adapts to the length). Results show that increasing the harvester length (i.e., decreasing the modes resonant frequencies) improves the simulated energy. The best location to harvest energy is dependent on the harvester geometry. The resonant frequencies can be adapted to meet body location preferences or constraints. Moreover, variation in length has a greater impact than variation in width. Ergonomic constraints may not be met, indeed, for example long beams are more difficult to integrate on the human body. Adding ergonomics boundaries by constraining the length and the width of the beam would provide more realistic results. In addition, maximizing or minimizing dimensions is not always sufficient. The behavior of the beam can be modified by adding a mass at the end or by changing the materials and the structure.

In addition, in order to simulate properly the model response to the acceleration data it is necessary to consider multiple vibrational mode. Based on chapter 3 materials, the acceleration data are resampled by a factor 5 for simulation purposes. This does not add information in the signals but reduces the simulation time step. However, it should be kept in mind that processing a high-frequency vibration modes involves a high-frequency sampled input signal. As an example, the highest resonant frequency studied is equal to 1005.03 Hz, which implies a sampling frequency of the input signal at least twice as high. In our case, this is not relevant because the information in the acceleration data is only described for frequencies less than or equal to 120 Hz. The high modes are not excited so the energy they simulate is not taken into consideration. Thus, the obtained simulated energy is under estimated.

4.2.5 Conclusion of part 2

Design of cantilevered piezoelectric energy harvester for human body motion is challenging. Many parameters such as the location, the orientation or the dimension impact the harvesting energy. Nevertheless, approaches based on optimization methods allow to converge towards the best configuration.

This study evaluated the influence of the length and width of the harvester beam with a constant active material volume and the optimized orientation on the human body accelerations. A comprehensive evaluation is performed under mechanical damping assumptions. The best locations of the harvester with respect to the resonance frequencies of its vibrational modes has been presented. Results suggest that low frequencies harvester are preferable to maximize the simulated energy.

To go further, new parameters related to geometry or mechanical characteristics can be introduced. Optimization methods used as in part 1 (NSGA-II) of this chapter can then be used to determine the optimal configuration. Similarly to chapter 3, future studies can look into improving the acceleration data sampling frequency to have a better representation of the harvester frequency response. Determining the damping coefficients experimentally will improve the accuracy of the results obtained. In addition, evaluating other parameters of the harvester such as its shape, additional mass end or thickness would be relevant to optimize its design according to the body constraints. The evaluation of the harmonic modes contribution in the simulated energy would be also interesting to adapt the resonator design.

Chapter 5

CLOTH ARTIFACTS AND SMART ACTIVITY ASSESSMENT SYSTEM DESIGN

This chapter is based on the published work entitled *Hoareau, D.; Fan, X.; Abtahi, F.; Yang, L. Evaluation of In-Cloth versus On-Skin Sensors for Measuring Trunk and Upper Arm Postures and Movements, Sensors, 2023* [124]. This work is the result of a collaboration with the Karolinska Institutet laboratory based in Sweden and was carried out within the framework of a PhD mobility. The objective is to evaluate the measurement artefacts of an existing system used for posture assessment.

In the first part, additional state-of-the-art is provided concerning the challenges in the ergonomics field. In addition, the performed experiment to evaluate the cloth artefacts using a smart workwear system with embedded IMUs is presented. Results are discussed using statistical metrics and analysis. In the second part, the design of an intelligent activity assessment system is conducted, related challenges are highlighted and future perspectives are suggested.

5.1 Part 1: Cloth Artefacts

5.1.1 Introduction

Work-related musculoskeletal disorders (MSDs) remain a substantial burden to individuals, organizations, and societies worldwide. In Europe, MSDs are the most prevalent work-related health problem: about 43 % of European Union (EU) workers reported back pain, and 41 % reported muscular pains in the shoulders, neck, and/or upper limbs in 2015 [125]. Work with tiring positions is still common in current workplaces and was reported by 43 % of workers for being exposed to at least a quarter of their work time in the EU [125]. In Sweden, it has been estimated that the total costs of MSDs were 102.3 billion SEK in 2012, which equaled 2.8 % of the national gross domestic product (GDP) [126].

In order to design effective intervention programs and prevent MSDs, a better understanding of the underlying mechanisms between exposures and outcomes, the development of practical and reliable risk assessment methods, and a wider use of such high-quality risk assessment methods, are among the key steps as suggested by researchers [127, 128, 129]. However, physical exposure has generally been assessed via questionnaires [130], which suffer from low accuracy and bias, and lack detailed information on exposure frequency or intensity [131, 132]. Exposure assessed with observational methods can also suffer from being sampled for a relatively short time period of the work day and high inter-rater variability [133, 134]. A limited number of studies included physical exposure data based on direct measurement and its association with occupational health outcomes. Two recent studies showed that direct measured arm elevation and trunk forward bending have a dose-response association with long-term sickness absence [135, 136]. With directly measured data of high accuracy, researchers found that ten more minutes of work time with the arm elevated more than 60° was associated with approximately 50 % higher risk of long-term sickness absence in four years, and five more minutes of work time with back forward bending over 60° was associated with 8 % higher risk [135, 136]. In addition, an action level for the median arm velocity has been proposed for the prevention of MSDs in the neck and upper extremities [137].

The latest technical development in wearable technology has provided opportunities to perform ergonomic risk assessments and interventions with accurate and convenient methods. Thanks to the growing market of wearable sensors, the development of new technologies are increasing for the risk assessment of work-related musculoskeletal disorders [138]. Systems composed of body area sensor networks providing continuous and automatic measurement have been created [139, 140].

The inertial measurement unit (IMU) is a widely used type of sensor with benefits of high accuracy, ease of implementation, and low user burden [141, 75, 142, 143]. A recent literature review on wearable inertial sensors for human motion analysis showed the increasing applications of such wearable sensors in industrial settings due to their portability, low cost, minimal invasiveness, and applicability outside of the laboratory environment [144]. More than half of the identified systems also provide real-time data analysis, which is an advantage for industrial applications including risk assessment, motion tracking to assist the design of collaborative robotics, and human action recognition [144]. Although embedded IMUs seem to be very relevant for the above applications, they measure motion but also motion errors induced by clothing artifacts. Thus, it is necessary to assess their contribution in order to determine the adapted compensation method.

To perform this evaluation, IMUs located in a garment are compared to IMUs located on the skin for measuring trunk and upper arm postures and movements. In the first part, the designed experiment is presented, simulated tasks are performed. Then, commonly used ergonomic exposure parameters, including the upper arm and trunk inclination angles, two types of upper arm velocities (the inclination velocity and the generalized velocity), and trunk inclination velocities, were calculated and compared during occupational activity. The resulting differences from the comparisons can provide knowledge about the accuracy and limitations of measurements for the practical use of smart workwear systems both in the lab and in the field.

5.1.2 Materials & Methods

5.1.2.1 Demographic data

Twelve volunteers (five males and seven females) participants were involved in this study. Before the experience, they were informed about the study and signed informed consent. The mean (± standard deviation) age of the participants was 32.8 ± 11.3 years, the height 174.2 ± 10.2 cm, the weight 68.7 ± 10.2 kg, and the BMI was 22.6 ± 2.7 kg/m^2. Eleven participants are right-handed, and one is left-handed. The study was approved by the Regional Ethics Committee in Stockholm (Dnr: 2019-01206).

5.1.2.2 Experimental setup

For this study, two sets of Inertial Measurement Units were used (Figure 5.1), with each set containing three sensors (Movesense, Suunto, Helsinki, Finland).

The first set of sensors was attached directly to the skin using double-sided tape, with two on the upper arms at the insertion of deltoids, and one on the upper back, at the level of T1-T2 vertebrae. An additional medical tape was put above the sensors on the skin to avoid relative movement. This setup is referred to as "skin sensors" in the following text. The second set of sensors was placed in an elastic T-shirt (Wergonic AB, Stockholm, Sweden), with pockets placed at both upper arms and upper back for the IMU sensors. The shape of the pocket and the extra sensor case with a matching shape feature were designed to prevent sensor rotation and limit relative movement errors (Figure 5.1). The second setup is referred to as "cloth sensors" in the following text. The shirt size, with a range of small to extra-large, was chosen for each participant to be comfortable and tight.

Figure 5.1 – To the left: the two sensor setups showing (a) the trunk sensor in the shirt, (b) the trunk sensor on the skin, (c) the right upper arm sensor on the skin, and (d) the right upper arm sensor in the shirt. To the right: the Wergonic T-shirt pocket and the matching sensor case.

The two sets of sensors were placed close to each other without overlapping. Both the accelerometer and the gyroscope data from the IMU sensors were sampled at 104 Hz and collected by the Movesense showcase iPhone application (Amer Sports Digital Services Oy, Helsinki, Finland) using Bluetooth

5.1.2.3 Experimental protocol

The experiment consisted of calibration steps and simulated work tasks. The calibration was necessary for the data fusion presented in the next section. It consisted of three calibration poses, and participants were instructed to hold each pose still for three seconds (Figure 5.2):

- **I-pose**: Stand up straight and look straight forward with arms at each side;
- **Forward**: trunk bending: Bow forward at about 90 degrees;
- **T-pose**: Stand up straight and look straight forward, and hold the arms horizontally to the sides at 90 degrees;

After the calibration, participants were introduced to the work tasks and instructed to perform the tasks as they would naturally do. When possible, they were also instructed to use their dominant hand to perform the tasks mainly. The duration of each task was two minutes. The different tasks were chosen to represent work scenarios using upper arms and back at low and high angle amplitudes and velocities. This allows the assessment of

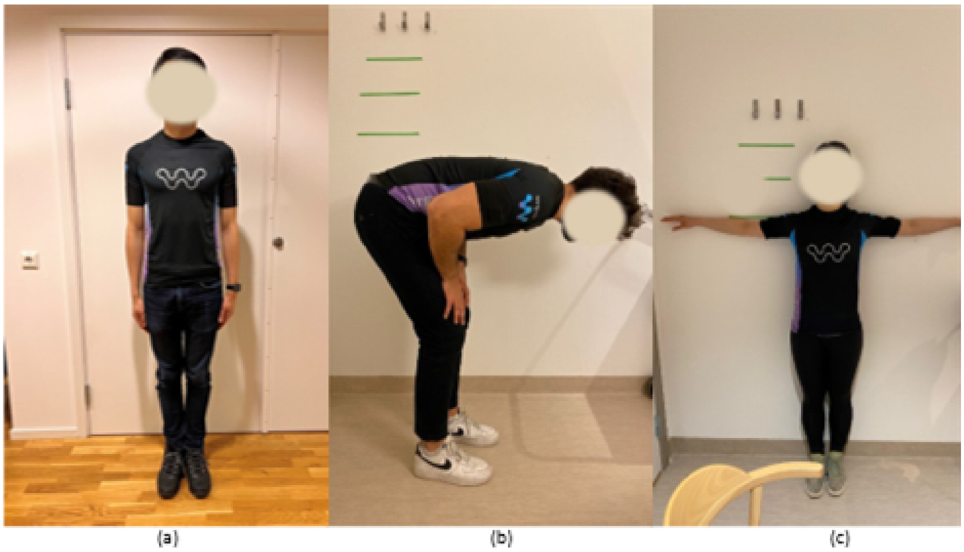

Figure 5.2 – Calibration poses: (a) I-pose of standing straight with arms relaxed by the body, (b) Forward trunk bending at about 90 degrees, and (c) T-pose of standing straight with both arms lifted at about 90 degrees.

the shirt setup in different conditions of use. The tasks performed were as follows (Figure 5.3):

- **Lifting boxes**: lift a light box from the floor to the table in front and put it back, and from floor to table to the side and put it back;
- **Sorting mail**: sort mail with marked letters into the corresponding compartments at different heights;
- **Wiping floor**: clean paper scraps on the floor and put them into a box using a shovel and broom;
- **Cleaning dishwasher**: empty cups and plates from the dishwasher and store them on shelves;
- **Cleaning windows**: clean windows with markers at different heights using a rag and spray bottle.


(a) (b) (c) (d) (e)

Figure 5.3 – Performed simulated work tasks: (a) Lifting boxes, (b) Sorting mail, (c) Wiping floor, (d) Cleaning dishwasher, and (e) Cleaning windows.

5.1.2.4 Data fusion and signal processing

Raw data from the IMUs were processed in Matlab (version R2022a, MathWorks, Inc., USA). The inclination angle, inclination velocity, and generalized velocity were computed for the sensors on the arms. The sagittal inclination angle and sagittal inclination velocity were computed for the trunk. The posture and movement computations of both the arms and trunk followed the processing steps described in Fan and al. [145]. Firstly, data from accelerometers and gyroscopes were integrated with a sensor fusion algorithm to reduce the effects of the non-gravitational (dynamic) acceleration and to generate corrected gravitational acceleration. In the sensor fusion algorithm, the original data were resampled to 128 Hz and processed by a Kalman filter with the recommended coefficients [146]: 0.005 rad/s for the gyroscope white noise, 0.1 m/s^2 for the accelerometer white noise, and 0.0005 rad/s^2 for the gyroscope bias. Then, the corresponding angles of each body part were calculated using the reference poses:

- **Inclination angles (Arms)**: Upper arm inclination angles were obtained by calculating the relative angle to the reference I-pose [147].
- **Forward/Sagittal inclination angles (Trunk)**: The forward inclination angles (inclination angles on the sagittal plane) were obtained using Hansson forward/backward projections and the according I-pose as the reference and forward trunk bending to indicate the direction [148].

Kalman filter

The Kalman filter was developed by Rudolf E. Kalman in 1960 [149]. It is based on random processes defined by the evolution of random variables. It consists in estimating a real discrete process x_k at time k by $\widehat{x}_{k|k}$ (estimated state at time k) and $\widehat{P}_{k|k}$ (the covariance matrix of error). It is an iterative process based on 2 stages: the prediction stage and update stage. Using observed values and the accuracy of the estimated state, one can obtained the estimation of the discrete process.

Finally, two types of angular velocities were calculated for comparison since both computational methods have been used and reported in previous research, and large differences in values have been observed between them [150, 151]. In addition, recent studies have identified large differences in the values between these two computational methods [145, 147, 152]. Since there are currently no standard metrics for assessing the arm's angular velocity, the performance of the in-cloth sensors vs. on-skin sensors using both metrics is worth evaluating. The two types of angular velocities were described below:

- The inclination velocities (arms and trunk): were computed by using a simple temporal derivation, i.e., dividing the difference between two samples of inclination angles by the sampling time;
- The generalized velocities (arms): the upper arm generalized velocities were obtained [148] by dividing the angular difference of the gravitation vectors between two samples on a unit sphere with the sampling time [148, 152].

5.1.2.5 Statistical analysis

After synchronizing and extracting the upper arm and trunk angles and velocities of each work task, a comparison between the skin sensors and cloth sensors was made on the following parameters. For the upper arm and trunk inclination angles, the 5^{th}, 10^{th}, 50^{th}, 90^{th}, and 95^{th} percentiles of the angles and the percentage of time with the angles less than 20°, as well as the time over 30°, 45°, 60°, and 90° were calculated. For the upper arm inclination and generalized velocities, as well as the trunk inclination velocities, the 5^{th}, 10^{th}, 50^th, 90^{th}, and 95^{th} percentiles were calculated. A paired comparison was made by using the mean absolute error (MAE) and its standard deviation (SD) for all parameters for each work task. In addition, Bland–Altman plots of the median and the 90^{th} percentile of the upper arm and trunk angles and inclination velocities for all tasks were applied to show the differences and the limits of agreement (calculated as mean ±1.96 SD) between the two sensor setups.

5.1.3 Results

5.1.3.1 Angular distributions

For the dominant upper arm, the cloth-sensor setup generally had small MAEs compared to the skin-sensor setup, ranging from 1.2° to 4.1° for the median upper arm inclination angle (Table 5.1).

Table 5.1 – The mean and the standard deviation (mean ± SD) of the mean absolute errors (MAEs) of the dominant upper arm inclination angle between cloth sensors and skin sensors during the five simulated tasks, with the reference value of skin sensors shown in brackets (N=12).

Dominant arm, Inclination	Simulated Work Tasks				
	Lifting boxes	Sorting mails	Wiping floor	Cleaning dishwasher	Cleaning windows
Percentile (◦)					
5^{th}	0.7 ± 0.5 (4.5)	1 ± 1.8 (3.7)	2.2 ± 1.6 (8.4)	0.6 ± 0.4 (5.6)	1.7 ± 1.2 (10.2)
10^{th}	0.7 ± 0.7 (6.4)	1.1 ± 1.8 (5)	2.4 ± 1.7 (11.4)	0.9 ± 0.3 (7.9)	2.5 ± 2.8 (15.8)
50^{th}	1.4 ± 1.1 (17.1)	1.5 ± 1.9 (11.8)	2.7 ± 2 (23.6)	1.2 ± 1.4 (23.6)	4.1 ± 3.5 (52.7)
90^{th}	3.5 ± 2.1 (32.4)	2.8 ± 3.1 (25.6)	2.5 ± 1.6 (36.6)	7.6 ± 3.8 (70.8)	7 ± 4.3 (103.2)
95^{th}	4.1 ± 2.2 (36.2)	3.6 ± 3.3 (34.3)	2.2 ± 1.4 (40.8)	8.3 ± 3.8 (83.1)	7.4 ± 5 (112.2)
Percentage of time (%)					
<20°	6.1 ± 4.4 (61.8)	4.6 ± 5.8 (81.1)	9.3 ± 8.5 (39.3)	2.6 ± 2.8 (41.8)	2.2 ± 2 (18.9)
>30°	3.1 ± 2.7 (13.9)	2.6 ± 4.1 (8.3)	7.1 ± 6.1 (27.2)	2.5 ± 3.1 (38.8)	2.4 ± 1.3 (71.4)
>45°	1.6 ± 2.5 (1.7)	1.3 ± 2.5 (3.4)	2.1 ± 4 (4.7)	1.5 ± 2 (23.4)	3.7 ± 2.5 (57.8)
>60°	0.1 ± 0.2 (0.1)	0.6 ± 1 (1.2)	0.4 ± 1.1 (0.2)	3.3 ± 2.4 (15.8)	4.4 ± 3.6 (44.6)
>90°	–	0.1 ± 0.5 (0.1)	–	2 ± 1.9 (3.1)	4.7 ± 2.4 (19.9)

Larger errors were observed for the cleaning dishwasher and cleaning windows tasks when looking at the higher percentiles, with MAEs of 7.6° and 7° for the 90^{th} percentile angle and MAEs of 8.3° and 7.4° for the 95^{th} percentile angle. The differences were smaller in the non-dominant upper arm, with the MAE ranging from 1.3° to 2° for the median upper arm inclination (Table A1 in the appendix). The differences and limits of agreement between the skin sensors and cloth sensors during the simulated tasks for the dominant and non-dominant arms are also presented with Bland-Altman plots in Figure 5.4. Similarly, larger differences were observed for the cleaning dishwasher and cleaning windows tasks. For the dominant arm, the mean difference was $-0.15°$ for the median inclination angle, and the limits of agreement were $-6.5°$ and $6.2°$.

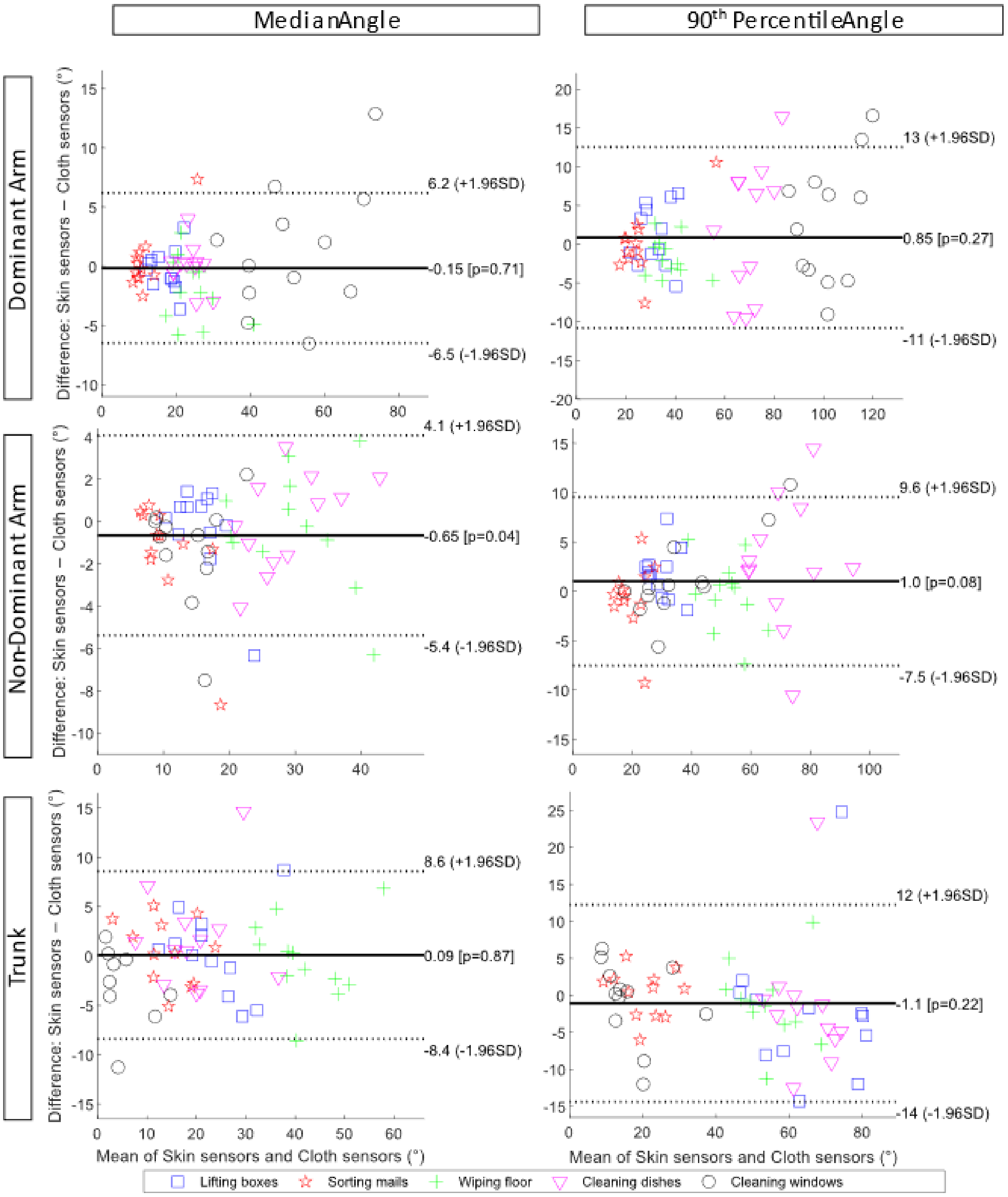

Figure 5.4 – Bland-Altman plots of the upper arm inclination and trunk forward inclination angle during the five simulated work tasks showing the limits of agreements between skin sensors and cloth sensors. From top to bottom: the dominant arm, non-dominant arm, and the trunk. To the left: the median angles, and to the right: the 90^{th} percentile angles.

The mean difference for the 90^{th} percentile dominant arm inclination was 0.85° with limits of agreement of $-11°$ and 13°. For the non-dominant arm, the limits of agreement were smaller than the dominant arm, with $-5.4°$ and 4.1° for the median inclination angle and $-7.5°$ and 9.6° for the 90^{th} percentile inclination angle. In addition, individual differences were observed, and larger errors between the cloth sensors and skin sensors were observed for few participants. Figure 5.5 and Figure 5.6 illustrate this variance in time-series angular measurements of the cloth sensors against the skin sensors.

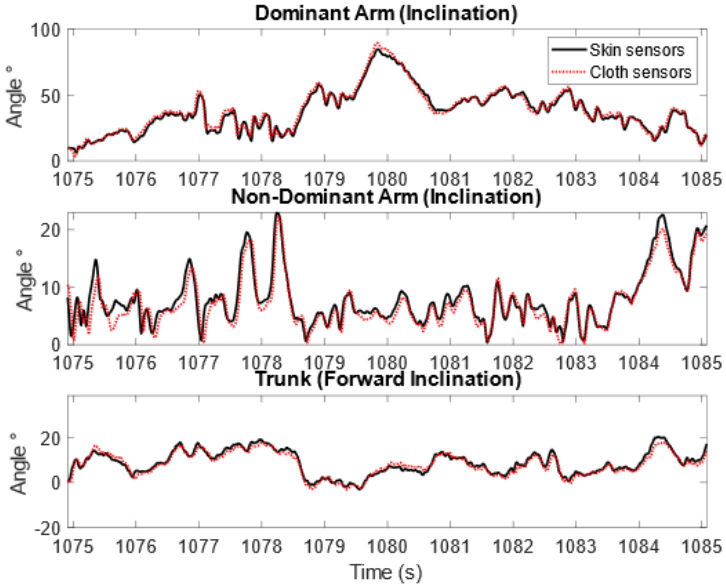

Figure 5.5 – An example of the upper arm inclination and trunk forward inclination angles measured by skin sensors and cloth sensors for one participant during the simulated window cleaning task for 10 seconds, showing good agreement between the skin sensors and cloth sensors.

In Figure 5.5, the angular measurements by the cloth sensors were in good agreement with the skin sensors, illustrated by the example of one participant cleaning windows. As a comparison, in Figure 5.6, larger differences were observed, as shown by the example of one participant cleaning the dishwasher. The differences became larger when the arms were lifted higher for the upper arms, and a constant difference was observed for the trunk inclination throughout the task. For the trunk, the MAEs between the cloth and skin sensors ranged from 2.7° to 3.7° for the median forward inclination angle (Table 5.2).

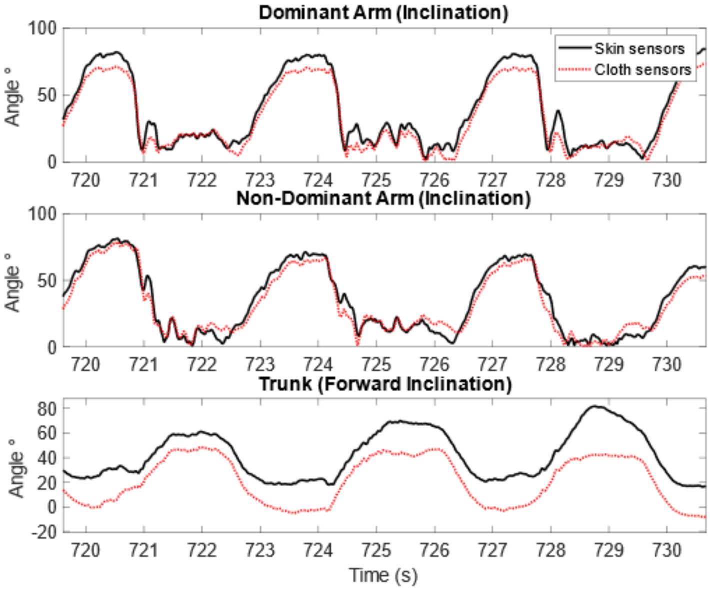

Figure 5.6 – An example of the upper arm inclination and trunk forward inclination angles measured by skin sensors and cloth sensors for one participant during the simulated dishwasher cleaning task for 10 seconds, showing worse agreement between the skin sensors and cloth sensors.

Table 5.2 – The mean ± standard deviation of the mean absolute errors (MAEs) of the trunk forward inclination angle between cloth sensors and skin sensors during the five simulated tasks, with the reference value of skin sensors shown in brackets (N=12).

Trunk, Forward inclination	Simulated Work Tasks				
	Lifting boxes	Sorting mails	Wiping floor	Cleaning dishwasher	Cleaning windows
Percentile (°)					
5th	2.8 ± 1.9 (2.4)	2.6 ± 1.4 (5.6)	2.5 ± 2 (20.5)	3.3 ± 4.1 (-3.8)	3.6 ± 3.3 (-8.4)
10th	2.9 ± 1.9 (5.8)	2.7 ± 1.5 (7.7)	2.6 ± 1.9 (25.2)	3.2 ± 4.8 (-0.7)	4.1 ± 3.3 (-6.1)
50th	3.2 ± 2.7 (23.6)	2.7 ± 1.7 (14.4)	3.1 ± 2.5 (41.9)	3.7 ± 3.9 (20.4)	3.7 ± 3.2 (3.1)
90th	6.8 ± 7.2 (63.8)	2.7 ± 1.7 (20.7)	3.9 ± 3.7 (53.6)	5.6 ± 6.7 (64)	3.9 ± 3.7 (16.6)
95th	6.8 ± 7.2 (67.3)	2.5 ± 1.9 (22.4)	4.1 ± 4.1 (56.3)	5.8 ± 6.4 (70.9)	3.9 ± 3.6 (21.1)
Percentage of time (%)					
<20°	4.8 ± 4.2 (42.5)	10.7 ± 11.4 (78.4)	2.4 ± 2.4 (6.8)	4.5 ± 6.9 (48.6)	4.4 ± 5.9 (93.1)
>30°	4.6 ± 5.3 (43.5)	1.4 ± 2.7 (2.9)	4.8 ± 4.2 (78.1)	3.4 ± 4 (42.6)	1.4 ± 1.7 (2.6)
>45°	4 ± 4.5 (30)	0 ± 0 (0.1)	7 ± 7.1 (36.7)	3.3 ± 4.6 (26.8)	0.2 ± 0.4 (0.5)
>60°	7.2 ± 9.3 (14.8)	0 ± 0.1 (0.1)	6.4 ± 10.9 (8.6)	4.2 ± 7.3 (14)	0 ± 0.1 (0)
>90°	–	–	–	–	–

The maximum MAEs were observed for the lifting boxes and cleaning dishwasher tasks, with MAEs equal to 6.8° and 5.8° for the 95^{th} percentile angle, respectively. For the percentage of time with angles less than 20°, the largest difference was observed for the task of sorting mail, with the MAE equal to 10.7 %. A potential reason could be that during this specific task, the participants spent a lot of time around 20° trunk inclination (mean time percentage of 78 %), and the error would lead to misclassification for trunk inclination $< 20°$. The Bland-Altman plots show the limits of agreement between the skin sensors and cloth sensors for the trunk inclination angle (bottom row, Figure 5.4. The mean difference of the median trunk inclination was 0.09° with limits of agreement of $-8.4°$ and 8.6°. Larger differences are observed for the 90^{th} percentile trunk inclination with a mean difference of $-1.1°$ and limits of agreement of $-14°$ and 12°. In addition, individual differences were observed, especially during the task of lifting boxes and cleaning the dishwasher.

5.1.3.2 Angular velocity

For the dominant arm, the MAEs between the cloth and skin sensors were generally small, ranging from 1°/s to 4.5°/s for the median inclination velocity (Table 5.3).

Table 5.3 – The mean ± standard deviation of the mean absolute errors (MAEs) of the dominant upper arm inclination velocity between cloth sensors and skin sensors during the five simulated tasks, with the reference value of skin sensors shown in brackets (N=12).

Dominant Arm, Inclination velocity	Simulated Work Tasks				
	Lifting boxes	Sorting mails	Wiping floor	Cleaning dishwasher	Cleaning windows
Percentile (°/s)					
5th	0.3 ± 0.3 (2.5)	0.4 ± 0.3 (2.1)	0.2 ± 0.1 (2.5)	0.3 ± 0.3 (2.4)	0.4 ± 0.3 (4.3)
10th	0.5 ± 0.6 (6.4)	0.7 ± 0.4 (5.5)	0.4 ± 0.3 (6)	0.5 ± 0.4 (5.8)	0.9 ± 0.6 (10.4)
50th	1.8 ± 1.5 (33.5)	3.3 ± 1.7 (30.1)	1 ± 0.7 (31.8)	1.4 ± 1.2 (32.2)	4.5 ± 3.4 (64.8)
90th	4.1 ± 3.3 (96.3)	10.9 ± 5.5 (90.5)	4.1 ± 4 (91.7)	5.1 ± 4.7 (108.7)	18.8 ± 16.3 (191.6)
95th	5.1 ± 3.8 (121.7)	15.3 ± 7.6 (116.5)	5.5 ± 5.7 (116.2)	9.4 ± 7.3 (142.3)	26.1 ± 24.8 (244.1)

Maximum errors are found for the sorting mails and cleaning windows tasks with MAEs equal to 15.3°/s and 26.1°/s for 95^{th} percentile inclination velocity, respectively. These larger differences might be due to the sleeves not following the upper arm movements properly, especially during faster motions and at high inclination angle positions. For the non-dominant arm, the MAEs between the two sensor setups of the median inclination velocity ranged from 0.5°/s to 2.1°/s (Table A2 in the appendix). The MAEs of the median trunk forward inclination velocity had smaller values ranging from 0.4°/s to 2°/s (Table 5.4).

Table 5.4 – The mean ± standard deviation of the mean absolute errors (MAEs) of the trunk inclination velocity between cloth sensors and skin sensors during the five simulated tasks, with the reference value of skin sensors shown in brackets (N=12).

Trunk, Forward inclination velocity	Simulated Work Tasks				
	Lifting boxes	Sorting mails	Wiping floor	Cleaning dishwasher	Cleaning windows
Percentile (°/s)					
5th	0.3 ± 0.2 (2.6)	0.1 ± 0.1 (1)	0.1 ± 0.1 (1.4)	0.2 ± 0.1 (1.6)	0.2 ± 0.2 (1.9)
10th	0.3 ± 0.3 (5)	0.1 ± 0.1 (2)	0.2 ± 0.1 (2.9)	0.3 ± 0.2 (3.2)	0.2 ± 0.2 (4.2)
50th	2 ± 3.1 (27.7)	0.4 ± 0.3 (9.8)	1 ± 0.7 (15.2)	0.9 ± 1.2 (17.6)	1.3 ± 0.7 (22.3)
90th	11 ± 10.7 (115.5)	1.6 ± 1 (28.7)	2.9 ± 2 (48.5)	3.5 ± 3.1 (64.5)	3.3 ± 1.8 (64.2)
95th	13.2 ± 12.1 (154.5)	2.1 ± 1.3 (36.9)	3.5 ± 3 (64)	5.2 ± 5.2 (87.8)	3.2 ± 1.8 (81.8)

The lifting boxes task had the maximum difference with MAE equal to 13.2°/s for 95^{th} percentile inclination velocity. The limits of agreement between the skin sensors and cloth sensors of the upper arms and trunk inclination velocities during the simulated tasks are also shown as Bland-Altman plots in Figure 5.7.

For the dominant arm, the mean difference value was 0.75°/s, and the limits of agreement were -5°/s and 7.1°/s for the median inclination velocity. The larger dispersion of data points was observed for the cleaning windows task. This could be partly due to the large variance in individual work techniques. For the 90^{th} percentile inclination velocity of the dominant arm, the mean difference value was 2.7°/s, and the limits of agreement were -23°/s and 28°/s. For the trunk median inclination velocity, the mean difference was 0°/s, and the limits of agreement were -3.8°/s and 3.8°/s. For the 90^{th} percentile trunk inclination velocity, the mean difference value was -1.5°/s, and the limits of agreement were -16°/s and 13°/s. A larger dispersion was observed for the lifting boxes task. The generalized angular velocities showed significantly higher differences between the two sensor setups. For the median upper arm generalized velocity, compared to the upper arm inclination velocity, the maximum MAEs increased from 3.8°/s to 15.3°/s for the dominant arm and from 2.3°/s to 3.9°/s for the non-dominant arm (Tables A3 & A4). The differences became more evident when looking at the 95^{th} percentile of angular velocity. This could be explained by the definition of generalized angular velocity, where movements in all directions are included, compared to the inclination velocity, where the only change in the inclination is included.

5.1.4 Discussion

This study evaluated in-cloth against on-skin sensors for measuring trunk and upper arm postures and movements for smart workwear systems during simulated work tasks.

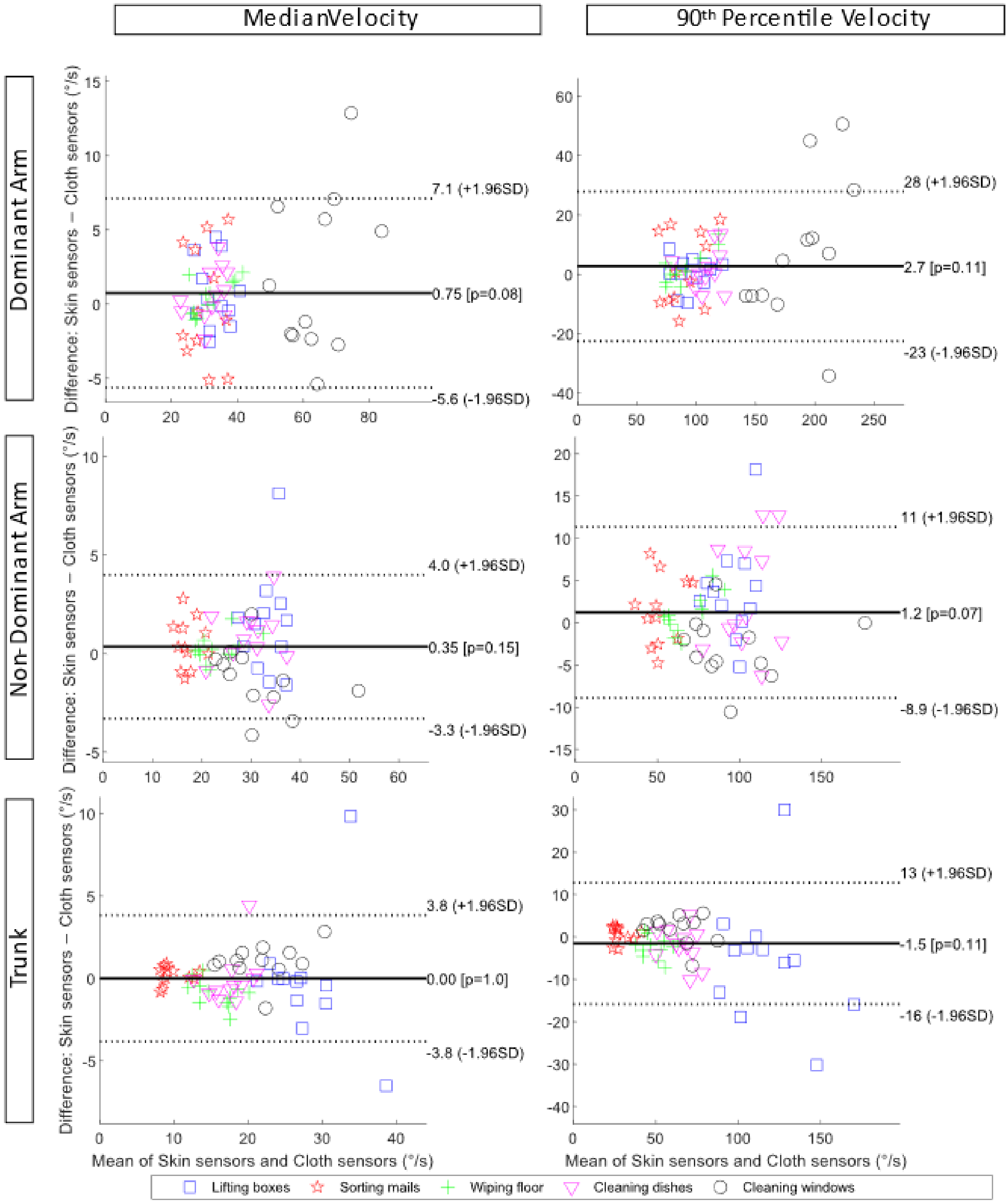

Figure 5.7 – Bland-Altman plots of the upper arm inclination velocity and trunk forward inclination velocity during the five simulated work tasks showing the limits of agreements between skin sensors and cloth sensors. From top to bottom: the dominant arm, non-dominant arm, and the trunk. To the left: the median inclination velocity, and to the right: the 90^{th} percentile inclination velocity.

For most tasks, high agreements between the two sensor setups were observed for the up-per arm and trunk angles. For the arm, slightly higher errors were observed for the 90^{th} and 95^{th} percentile of arm inclination angle and velocity during cleaning windows and cleaning the dishwasher. For the trunk, slightly higher errors were observed for the 90^{th} and 95^{th} percentile of trunk inclination and velocity for lifting boxes and cleaning the dishwasher. The generalized velocity had distinctively higher errors for both the upper arms and trunk. The in-cloth sensors showed acceptable accuracy on a group level for measuring upper arm and trunk inclinations and inclination velocities.

The simulated tasks in this study were chosen to cover a large range of work activities that may involve arm and trunk movements, thus evaluating the in-cloth sensors in different settings. Activities like cleaning windows and cleaning dishwashers involved higher movement amplitudes for the dominant arm. The errors of the in-cloth sensor compared to on-skin sensors were higher in these cases, which is expected. As shown in Table 5.1, the MAEs increased in general from the 5^{th} to 95^{th} percentile of the upper arm angle. Still, the MAEs were less than 4.1° for all the median arm inclination values. A similar phenomenon was observed in the arm inclination velocities (Table 5.3). The median arm inclination velocity had MAEs smaller than 4.5°/s in all tasks. Higher errors were observed when the generalized velocities were calculated (Table A3). The maximum MAE for the median generalized velocity was 15.3°/s during cleaning windows (reference value being 124.2°/s), and the MAEs were significantly higher for the 95^{th} percentile of arm generalized velocity. This is expected since the definition of generalized velocity includes motions on all planes, compared to the inclination velocity, which only includes motions/changes in the inclination. Therefore, the performance of the in-cloth sensors can be affected to a higher degree by the cloth and motion artifacts during the tasks.

For the non-dominant arm, the in-cloth sensors had lower MAEs than the dominant arm regarding the inclination angle and velocity (Table A1). This is also expected as the non-dominant arm was less used. The maximum MAE was observed for the 95^{th} percentile inclination angle while cleaning the dishwasher, during which participants usually used their non-dominant arm to a larger degree. For the median inclination angles, the MAEs were less than 2° for all tasks. Concerning the non-dominant arm inclination velocities (Table A2), the overall MAEs were smaller than 6.6°/s. Higher MAEs were also observed for the non-dominant arm generalized velocities (Table A4). Regarding the trunk, lifting boxes and cleaning dishwashers involved higher movement amplitudes. The maximum MAE for trunk forward inclination angles was 6.8° for all tasks, which was observed during lifting boxes (Table 5.2). In general, the errors for trunk inclination velocity were quite small, with maximum MAEs of 2°/s and 13.2°/s for the median and 95^{th} percentile values, respectively, observed during the lifting boxes task (Table 5.4).

One thing worth noticing is that the MAEs for trunk inclination remained on a similar level from the 5^{th} percentile to the 95^{th} percentile throughout each task, even when the trunk forward inclination angle was small. Whereas for the upper arms, the MAEs in general increased for the higher percentiles of arm inclination (Table 5.1) and when the arms were lifted higher. This type of error is further illustrated in Figure 5.6. The relatively constant error for the trunk could be caused by the non-optimal fit of the cloths. The looseness of the garment where the trunk sensor was located or a potential overlapping of the cloth-sensor and skin-sensor could lead to the cloth-sensor having a slightly different tilt compared to the skin. Regarding the errors observed for the upper arms, it could potentially be caused by the elasticity of the sleeve fabric, leading to slightly larger cloth artifacts when lifting the arms high.

In addition to the fit of the clothes, different individual work techniques and individual height may also imply variances in the level of errors. For example, there was a high variance in the individual arm inclination angles and velocities during cleaning windows and the dishwasher and a high variance in trunk velocities while lifting boxes. Therefore, this variance is good to include in the experiment so the results can represent different work scenarios and individuals.

Another limitation was the placement of the two sensor setups, which should ideally be at the same location, i.e., at the insertion of the deltoids and the level of T1–T2 vertebrae. However, since overlapping of the sensors was undesirable, they could not be placed in the same place. Therefore, the cloth sensors were placed carefully close to the skin sensors without overlapping each other. However, for a few participants, the overlapping of the cloth sensors on the skin sensors of the upper arms was observed. This can lead to overestimated errors of the cloth sensors since normal wear of the T-shirt will be tighter on the skin and potentially a better fit on the body without another sensor in between.

Future studies can look into error-correcting algorithms for the in-cloth sensors set up to improve their performance for smart workwear systems. This study highlights the existing errors in such a system and can contribute to how to find the most adapted approach in future studies. One potential method is the use of artificial intelligence-based algorithms; for example, Lorenz et al. [76] used a probabilistic neural network based on a supervised learning method to reduce loose cloth artifacts.

5.1.5 Conclusion of part 1

This work evaluated the in-cloth sensors against the on-skin sensors in simulated work tasks for upper arms and trunk posture assessment. Errors from in-cloth sensors were quite low for all median values of inclination angles and velocities. Larger errors were observed for the 90^{th} and 95^{th} percentiles of inclination angles and velocities. The performance depended on the tasks and was affected by individual factors, such as the fit of the clothes. Nevertheless, future work should compensate for the cloth artifacts and thus improve measurement accuracy. In conclusion, in-cloth sensors showed acceptable accuracy for measuring upper arm and trunk postures and movements on a group level. Considering the compromise between accuracy, comfort, and usability, such a system is potentially a practical tool for ergonomic assessment for researchers and practitioners.

Application aspects and IMU localization has been investigated, analysis of technological aspects related to wearable electronics are discussed then.

5.2 Part 2: Design of a smart activity assessment system

5.2.1 Introduction

Smart activity assessment systems aim to perform HAR with respect to the triptych: Robustness - Reliability - Precision (RRP). Its design must consider the ergonomic aspects. The morphology and the comfort of the users are significant factors. The study presented below aims to highlight the technological challenges and relate them to the sensor positioning issues discussed in the previous studies of this manuscript. The development of a complete smart garment requires engineering tasks that are not temporally conducted in this thesis work. Therefore, the engineering approach is conducted through rapid prototyping. In addition, the development of such a system can be used as a pedagogical support.

Thus, in this last part of this chapter, an overview of the design of an smart garment prototype is presented. Based on commercialized IMUs and a tight-fitting garment, rigid components are integrated to perform inertial measurements. Challenges related to the integration of electronic components are highlighted. This study was part of a student project, realized by Clemence Alglave, the objective was to evaluate the system performance.

5.2.2 System design

5.2.2.1 System description

The general structure of the smart activity assessment system (SAAS) can be described using the systems modeling language (SysML [1]). Figure 5.8 presents the block definition diagram of the SAAS. The SAAS is composed of a finite number of IMUs which are located on the whole garment. The measurements are acquired using a microcontroller, data can be sent wirelessly using a radio or stored in an internal memory. Energy storage,

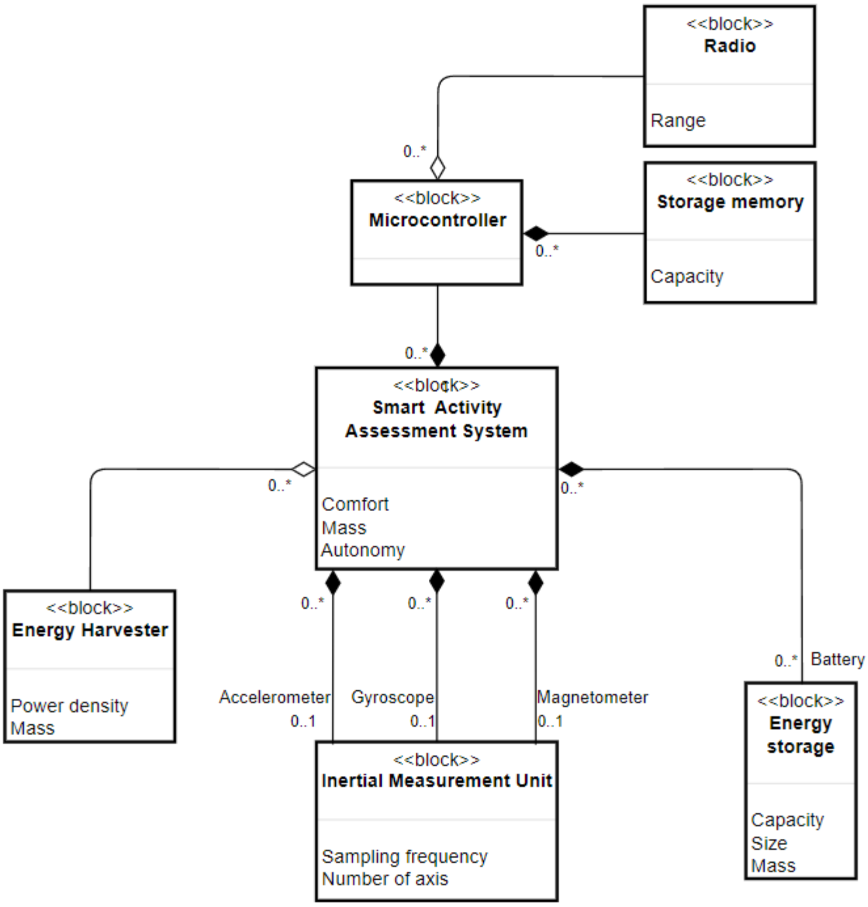

Figure 5.8 – Block definition diagram of the smart activity assessment system.

---

[1] `https://sysml.org/`

such as batteries, can power the components. Additional energy harvesters can be added to reduce battery capacity needs.

5.2.2.2 Technological choices

For rapid development and practical educational aspect, our first choice was the use of an Arduino board for data acquisition. This card was the MKR Zero [2] which is more easily integrated thanks to its small dimensions. The analogical and numerical inputs enable the acquisition and the processing of IMU data using the microcontroler SAMD21. In this first version of the prototype, collected data are saved locally as the board have a micro SD card holder. Regarding the choice of the IMUs, there are several commercialized brands. We opted for IMUs with low energy consumption and with a small size. We decided to integrate the M5 Stack 6DOF IMU [3] composed of accelerometers and gyroscopes only. Online available Arduino libraries exist facilitating the programming of this component, the communication protocol is the I^2C.

I^2C protocol

The I^2C protocol is a bidirectional synchronous serial half-duplex bus where multiple devices called masters and slaves can be connected. Exchanges take place between the master and the slaves, but only the master can decide when these exchanges should take place. This protocol is interesting when it comes to developing a low complexity system. 2 wires are necessary for data transmission and 1 wire for the ground.

However, as the IMUs only possess one address it is necessary to use a I^2C multiplexer. Thus, we integrated the TCA 9548A [4] multiplexer, the device operates at low voltage. To electrically power the system, a simple 3.7V 1800mAh LiPo battery is used. The T-shirt is long-sleeved and tight-fitting, made of 67 % polyester, 30 % polyamide, 3 % elastane. This allows to limit the relative movements and to be as close as possible to the body. The components are fixed on the garment using sewing threads, a pocket has been designed in the back to hold the battery.

---

[2] `https://docs.arduino.cc/hardware/mkr-zero`

[3] `https://shop.m5stack.com/products/6-axis-imu-unitmpu6886?variant=36022518186148`

[4] `https://www.ti.com/lit/ds/symlink/tca9548a.pdf`

5.2.2.3 First design

In the first design of the system, IMUs are distributed on each segment of the upper body, they are located on the forearms, upper arms, the sternum and the back. Figure 5.9 presents the schematic of the first system design.

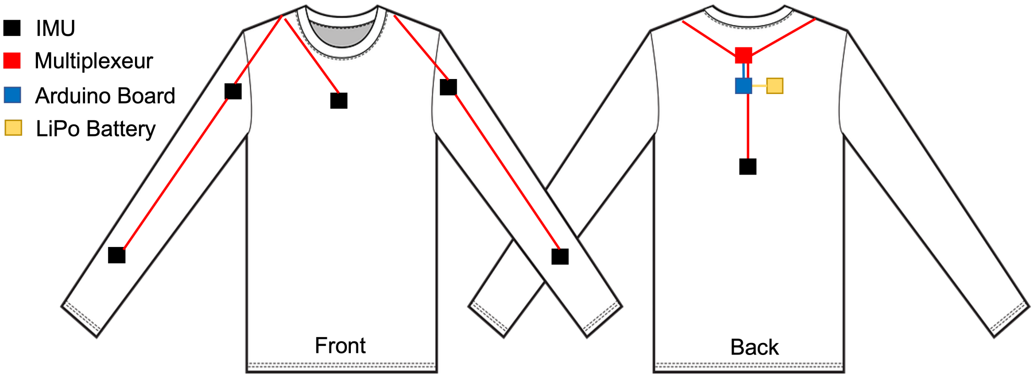

Figure 5.9 – Schematic of the first system version.

To connect each IMUs, 4 wires is needed in total. Two wires are used to power the devices (ground and suply voltage) and two other wires are used for I^2C data transmission (serial data line and serial clock line). The IMUs are connected to the multiplexer which is connected to the MKR Zero board. The MKR Zero board and the multiplexer board are located on the upper back to improve the comfort and reduce the length of wire required. Figure 5.10 shows the system designed equipped on the human body.

5.2.2.4 First test

The system had the opportunity to be tested through an experiment during a student project. The aim was to evaluate not only its comfort but also the triptych RRP. Thus, common sports activities such as those described in Chapter 3 were performed. Figure 5.11 presents the prototype worn by a particpant performing sport activities.

5.2.3 System characterization

5.2.3.1 Experiment conclusions

During the experiment the system showed a good performance as regard to its reliability and its robustness. The data was collected without interruption, and saved on

Figure 5.10 – Picture of the designed SAAS prototype.

Figure 5.11 – Experiment using the SAAS prototype.

the SD card. We were able to compute the data and compare the results to a reference system. However, the results showed inconsistency in the data measured by the system, impacted by a weak coupling due to the poor level of fixation of the components. Hence, it is necessary to improve the integration of those components in order to enhance the accuracy of the system.

5.2.3.2 User feedback

Apart from the RRP, the system must also be ergonomic and comfortable to wear. Unfortunately, due to the use of long, loose and non-stretchable wires, the movements of the user are affected and restrained by the wires, when large movements are performed and the piece of clothing is extended. Additionally, the designed system is embedded in a t-shirt and thus, does not perfectly fit all the morphology, even when the t-shirt is tight fitting. This reduces the comfort of wearing the device. Finally, despite the small sizes of the components, their rigidity compared to the flexibility of the garment makes their interfacing more difficult.

5.2.3.3 Discussion and perspectives

As discussed before, the main difficulties are found in the ergonomic and the comfort of the devices. This is mainly linked to the integration of electronic component in a piece of clothing. Indeed, despite the robustness and reliability of the system, improvements must be made in order to guarantee not only the accuracy but also the comfort of the system. The first difficulty is the integration of the rigid components in the cloth. To solve this issue, one can turn to soft electronics. Moreover, the question of the connectivity between soft and rigid electronics must be addressed [153]. Currently, the design of a second-version prototype based on conductive yarns is being investigated. Figure 5.12 presents a system with integrated components using conductive yarns.

The sleeve integrates an Arduino Nano 33 BLE board [5] and an MPU6050 [6] IMU conncted by conductive yarns. Data transmission was performed using the integrated Bluetooth radio. The system shows better components integration improving the comfort and the ergonomics. Nevertheless, the robustness of connections between the components and the conductive yarns are not always ensured.

---

[5] `https://store.arduino.cc/products/arduino-nano-33-ble?queryID=undefined`

[6] `https://invensense.tdk.com/wp-content/uploads/2015/02/MPU-6000-Datasheet1.pdf`

Figure 5.12 – Components integrated in a sleeve using conductive yarns.

Regarding fixations, the relative movement artifacts between the devices and the garment can be limited by the use of pockets (as presented in the first part of this chapter). Moreover, practical questions, such as cleaning, have not been addressed but should be looked into.

For now, it is impossible to find a universal piece of clothing, corresponding to all morphology. Therefore, the dimensions of the system must be adapted to each user to ensure comfort.

5.2.4 Conclusion of part 2

In this part, we proposed a design of a SAAS. The challenges related to the integration of electrical components are highlighted. New techniques and advancements in the field of flexible electronics and wearable electronics offer new opportunities. Indeed, better integration and interfacing should limit external factors and improve data reliability and comfort. Based on the difficulties and considerations discussed before, this work not only presents the challenges but also the related perspectives.

This work is still on-going, new design are being studied. In addition, in parallel to this thesis, the conception of a SAAS for smart insole for pressure measurement is the subject of an other thesis realized by Laaraibi Abdo-Rahmane-Anas, where similar challenges are raised. In addition, his thesis also deals about the development of a smart garment integrating smart textile for upper body posture assessment.

CONCLUSION

In this thesis, we investigated the aspects related to the design of an human activity recognition (HAR) system based on IMU measurements. Through a systemic approach, we are interested in the available information and energy sources on the human body. Indeed, HAR systems face several challenges including, not only the determination of IMU locations on the human body, but also autonomous and ergonomic constraints. In addition, the technological and practical aspects of an intelligent activity assessment system for HAR are addressed through the design of a prototype wearable system. Defined by many parameters and a high level of interactions, the HAR system can be characterized as a complex system. Thus, optimization methods are implemented to evaluate the optimal configurations of the HAR system.

Nevertheless, efficient optimization methods exist and their implementation allows to explore the possibilities to converge towards optimal configurations.

The location and the number of IMUs on the human body affect the accuracy of the HAR and the energy consumption of the system. High energy requirements increase the amount of energy storage needed, which, depending on the technology, can have an impact on ergonomics and environmental sustainability. In addition, from a practical perspective, the integration of electrical components on a smart activity assessment system is not trivial and can be difficult. External artefacts such as relative cloth movements induce measurements errors. Hence, this thesis proposed to highlight these aspects both individually and jointly. The contributions made are presented in the different chapters, the methods and the results obtained are summarized in the following section.

Summary of contributions

Chapter 2 starts with the observation that the literature provides multiple HAR applications with different IMU configurations on the human body. Nevertheless, testing experimentally all configurations to obtained the optimal is not feasible because it is time consuming. Thus, it is necessary to investigate new methods to evaluate the optimal configurations. The second chapter of this thesis presents a method based on synthesized

IMU data (SID) to conduct configuration evaluation. Data from a biomechanical model based on motion capture of the whole human body are extracted. Indeed, this data makes it possible to evaluate multiple locations on the body without the need to conduct many experiments. However, as these data are not directly obtained from direct sensor measurements, it is necessary to evaluated their reliability according to HAR applications. In this study, we compared the measurements of the SID with real IMU data (RID). In addition, we performed HAR on 154 locations with SID. Results show consistency of SID. They can be used for evaluating real IMU configuration according to HAR application. However, one must keep in mind the assumptions and conditions under which this study was conducted: the biomechanical model is based on an osteoarticular model and does not consider soft tissue artefacts. This point is particularly addressed in Chapter 5 part 1. In addition, only few features have been selected and HAR has been performed on the acceleration norm using a single IMU at a time. The optimizations of Chapter 4 part 1 compute HAR with a larger set of features. Perspectives suggest to deepen the features selection and data fusion techniques. Futures studies can be based on the use of SID to evaluate HAR materials such as IMU configurations.

Therefore, thanks to this first contribution, available information sources aspect has been investigated. The second contribution of this thesis is related to energy aspects. In harmony with the need to reduce environmental impact and move towards self-powered systems, piezoelectric harvesting from the human body is considered an suitable solution. Based on kinetic energy and described in the literature as a promising candidate for energy harvesting, piezoelectric generators can be very interesting. Nevertheless, challenges related to their design for harvesting energy on the human body or their location and orientation has been addressed. In addition, depending on the application, the size, fragility or energy harvested may limit its performance. Investigation of such a system in sports applications is still not very developed, thus, we proposed to explore this possibility. As there are no general method and difficulties in performing experiments, we proposed a numerical approach based on an electromechanical model to determine the best configuration of cantilevered piezoelectric harvester. Based on measured acceleration data on the human body, the best location and orientation of a cantilevered piezoelectric harvester has been investigated numerically. The simulated energy obtained was examined with respect to the acceleration characteristics. Results show that depending on the human body location, the best orientation can be obtained using the existing invariants in the structure of the harvester. Analysis of data acceleration shows that the impacts present in the activities could represent more than 80 % of the energy simulated by the model. Thus, impacts are relevant features to operate energy cantilevered piezoelectric harvester on the human body. In addition, the feasibility of configuration optimizing the simulated energy has been highlighted, it showed that it is not always ergonomically feasible. Nonetheless, the study has been constrained by the sampling frequency of the sensors (limiting the high frequency information contain in acceleration data). Only three orientations has been considered for the harvesters. This limitation is overcome with the search for optimal orientations presented in Chapter 4 part 2. Thus, in the same perspective as the first contribution, the method proposed here allows to study the best configuration of these piezoelectric harvesters without performing cumbersome experiments requiring expensive and constraining materials.

Chapters 2 and 3 both introduced a first uncoupled aspect of information and energy sources on the human body. Thus, in the continuity of this thesis, we introduce a coupling between these two different sources. The third contribution is presented in Chapter 4, we address the optimization of HAR accuracy and energy consumption. The aim was to determine the optimal IMU configuration to maximize accuracy and minimize power consumption. The evaluation of the configuration is not based on SID for the moment, to get rid of SID assumptions and as a first proof of concept, we directly used real IMU data. In addition, limiting the study to the 17 real IMUs reduces the size of the problem, which is fairly large already. When performing HAR, we generally rely on empirical rules to configure the system. However, this does not guarantee optimal results despite possible good results. Due to the complexity of the problem (interactions between parameters and their number), there is no simple method. Therefore, we investigated a method based on a heuristic algorithm (NSGA-II) to solve the problem. Using Pareto fronts, we illustrated the trade-offs between the HAR accuracy and the power consumption. Results show various possible distribution of IMUs on the human body, ergonomic constraints and practical aspects could be investigated to provide decision criterion. These two points are addressed in Chapter 4. The main difficulties rely on the stochasticity of the problem, its influence can be reduced, but it requires higher computational costs. Additional materials has been explored, especially geometry influence on the simulated energy of harvester model. Low frequency harvester are more suitable but are challenging to design. In addition, the best location to harvest energy depend on the harvester sampling frequency.

Although the ergonomic aspect has been emphasized and discussed through the first studies, it has not yet been addressed. In addition, errors induced by the integration of the sensors on activity assessment system are not negligible, it is necessary to consider them. In Chapter 5, the last contribution of this thesis involves the investigation of cloth artefacts in a smart workwear system for posture assessment. Challenges related to the design of a smart activity assessment system is also addressed. Evaluating systems performance in real use cases is a real opportunity, it allows to have a direct vision of the stakes. Hence, during performed simulated work tasks, errors induced by cloth relative movements on integrated IMU are evaluated. Results show high error values for large movements. Individuals factors and quality of the fit of the cloth contribute to the errors. Nevertheless, considering the comfort and usability of the system, it is a promising tool for posture assessment. Future studies tend to deal with the compensation of these errors. In the second part of this chapter, the design of a smart activity assessment system has brought up a lot of issues. Challenges are mainly related to the comfort and the integration of the components in a wearable system. As the comfort and the security of the user are a necessity, the integration of the interfacing of soft and rigid component are a crucial step.

Therefore, the contributions made are present in different level of HAR system design.

Final word and perspectives

The multidisciplinary approach has allowed to investigate HAR systems as a whole and highlight the main issues. Different aspects were addressed, dealing not only with information sources and energy sources but also the application aspects. Many areas of improvement are possible, other couplings can be explored in order to bring out new issues. Challenges related to the system design such as components integration and comfort can be transposed to other applications. This work is currently followed by another thesis realized by Laaraibi Abdo-Rahmane-Anas. His work focuses on the development of a smart insole for pressure measurements and a smart cloth for posture assessment.

PUBLICATIONS

International journals with proofreading committee

Hoareau, D., Jodin, G., Chantal, P. A., Bretin, S., Prioux, J., & Razan, F. (2022). Synthetized inertial measurement units (IMUs) to evaluate the placement of wearable sensors on human body for motion recognition. The Journal of Engineering, 2022(5), 536-543. `https://doi.org/10.1049/tje2.12137`

Hoareau, D., Jodin, G., Laaraibi, A. R. A., Prioux, J., & Razan, F. (2023). Available Kinetic Energy Sources on the Human Body during Sports Activities: A Numerical Approach Based on Accelerometers for Cantilevered Piezoelectric Harvesters. Energies, 16(6), 2695. `https://doi.org/10.3390/en16062695`

Hoareau, D., Fan, X., Abtahi, F., & Yang, L. (2023). Evaluation of In-Cloth versus On-Skin Sensors for Measuring Trunk and Upper Arm Postures and Movements. Sensors, 23(8), 3969. `https://doi.org/10.3390/s23083969`

Laaraibi, A. R. A., Jodin, G., Hoareau, D., Bideau, N., & Razan, F. (2023). Flexible dynamic pressure sensor for insole based on inverse viscoelastic model. IEEE Sensors Journal, 23(7), 7634-7643. `https://doi.org/10.1109/JSEN.2023.3245822`

[**Submitted**] Laaraibi, A. R. A., Depontailler C., Jodin, G., Hoareau, D., Bideau, N., & Razan, F (2023). An innovative wearable sensing system based on flexible piezoresistive sensors to estimate upper body joint angle using a Nonlinear AutoRegressive eXogenous Neural Model. IEEE Sensors Journal.

[**Draft to be submitted**] Hoareau, D., Jodin, G., Laaraibi, A. R. A., Prioux, J., & Razan, F. (2023). Optimal IMUs Positioning on the Human Body: Multi-objective Optimization of Human Activity Recognition and Power Consumption. IEEE Sensors Journal.

International conferences

Hoareau, D., Jodin, G., Prioux, J., & Razan, F. (2021). Evaluation tool of information sources for optimal inertial measurement unit placement for motion classification.

European College of Sport Science (virtual).

Hoareau, D., Jodin, G., Prioux, J., Laaraibi, A. R. A., Bartasyte, A., Margueron, S., Poulin-Vittrant, G., Bavencoffe, M., Brenes, A., Lefeuvre, E., & Razan, F. (2022). Towards eco-design of self-powered wearable devices: analysis of available energy on the human body for lead-free piezoelectric energy harvester positioning. ICAMPAM, Keystone, USA.

[**Accepted**] Yang, L., Hoareau, D., Abtahi, F., & Fan, X (2023). Evaluation of Cloth-Sensor Versus Skin-Sensor for Ergonomic Assessment of Trunk and Upper Arms Using a Smart Workwear System. AHFE, San Francisco, USA.

[**Accepted**] Hoareau, D., Jodin, G., Laaraibi, A. R. A., Prioux, J., & Razan, F. (2023). Available Kinetic Energy Sources on the Human Body During Sports Activities: An Optimization Investigation Using Cantilevered Piezoelectric Harvester Model. Eurosensors, Lecce, Italy.

[**Accepted**] Laaraibi, A. R. A., Jodin, G., Costanza, M., Hoareau, D., Margueron, S., Bideau, N., & Razan, F. (2023). A Low Cost, Self-Powered, Plantar Pressure Distribution Sensing Insole. Eurosensors, Lecce, Italy.

[**Submitted**] Lefeuvre, E., Brenes, A., Hoareau, D., Jodin, Razan, F., & Poulin-Vittrant, G. (2023). Human Body Piezoelectric Energy Harvesting Using USECE Interface Circuit. ICAE, Jeju, Korea.

National conferences

Hoareau, D., Jodin, G., Prioux, J., & Razan, F. (2021). Reconnaissance de mouvement : outil d'évaluation des sources d'informations pour le placement optimal de centrales inertielles. Sciences2024, ENS Rennes.

[**Submitted**] Laaraibi, A. R. A., Jodin, G., Costanza, M., Hoareau, D., Margueron, S., Bideau, N., & Razan, F. (2023). A Low Cost, Self-Powered, Plantar Pressure Distribution Sensing Insole. JRNSE, Paris, France.

APPENDICES

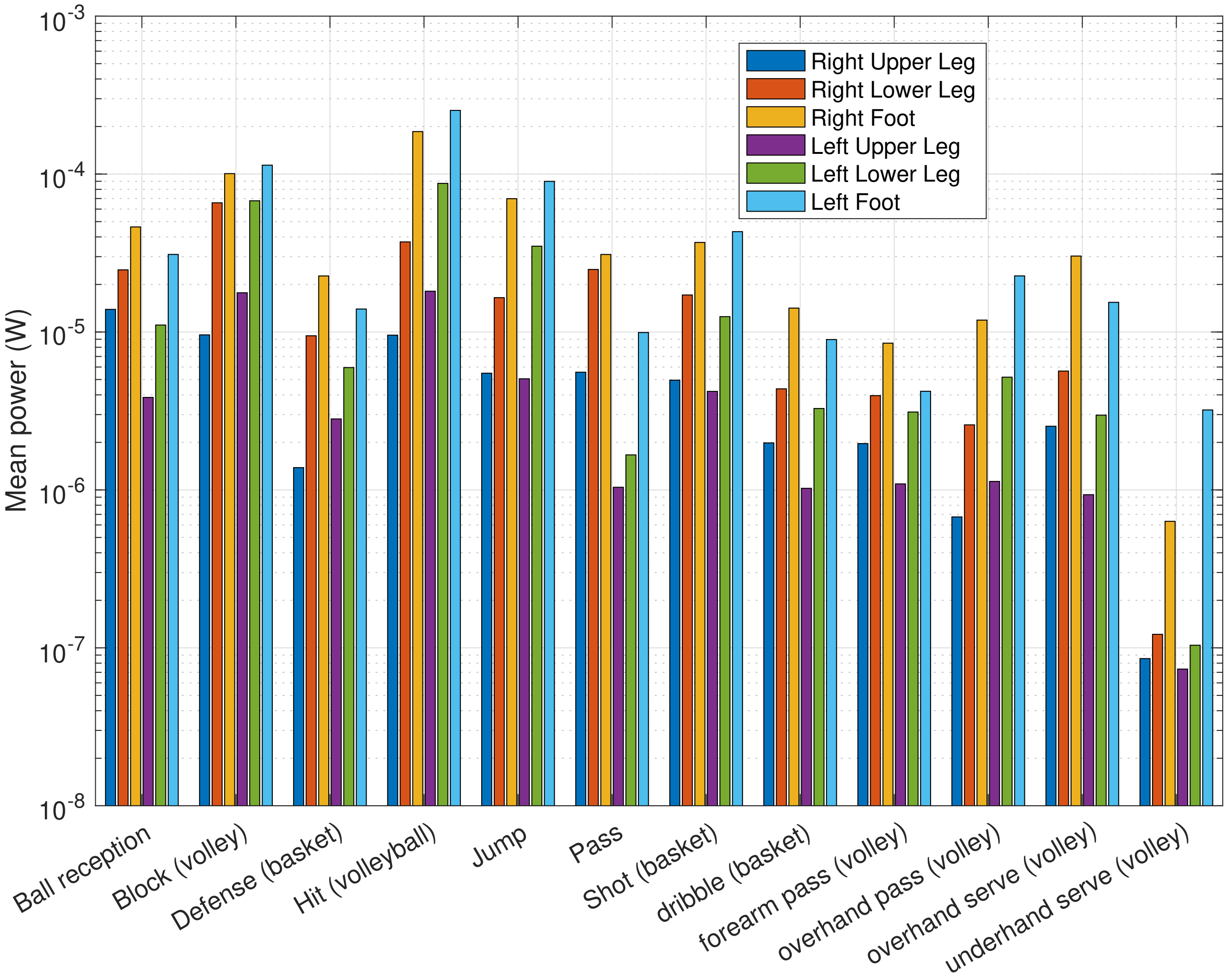

Figure A1 – Mean power prediction for some body locations according to performed activities.

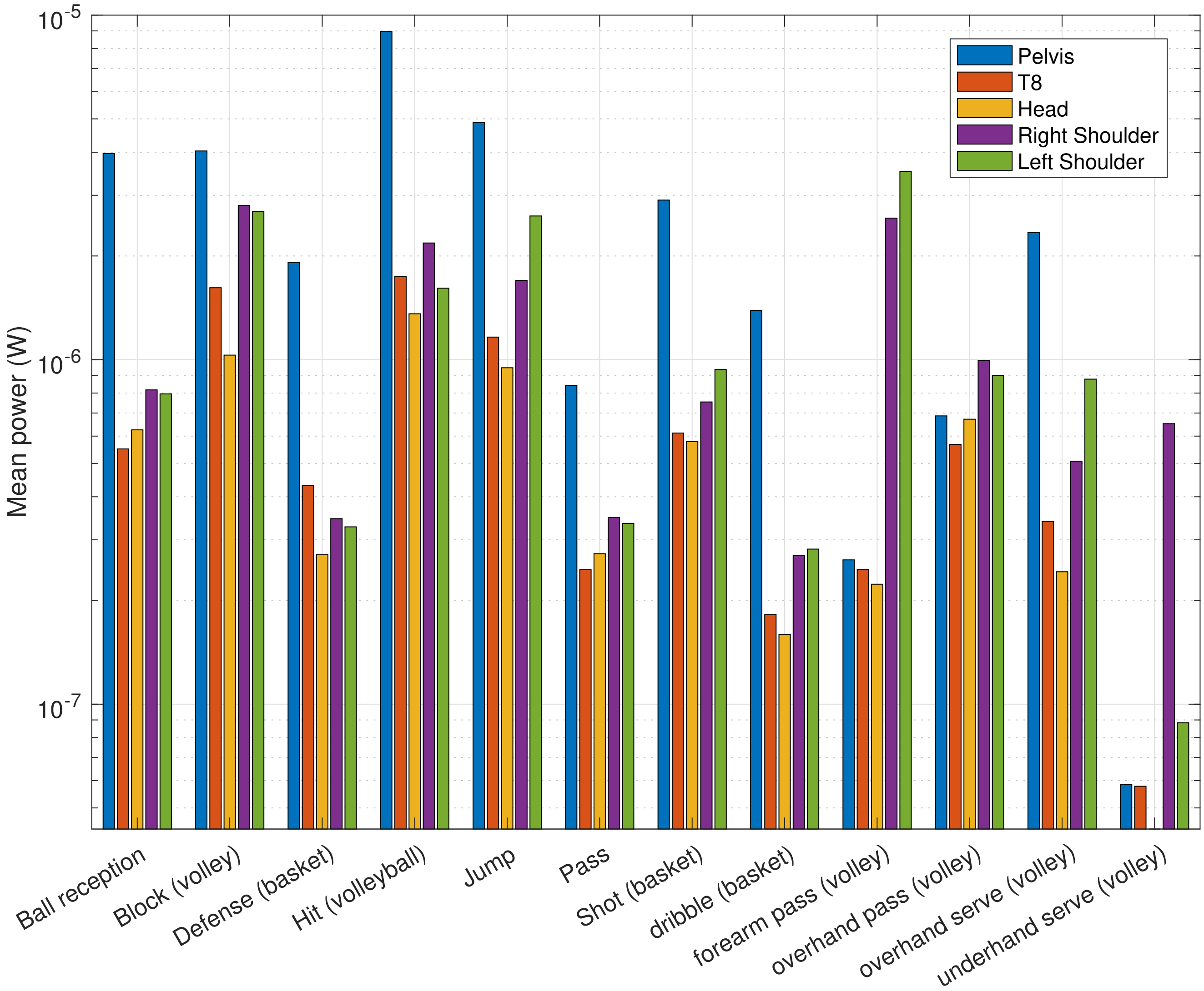

Figure A2 – Mean power prediction for some body locations according to performed activities.

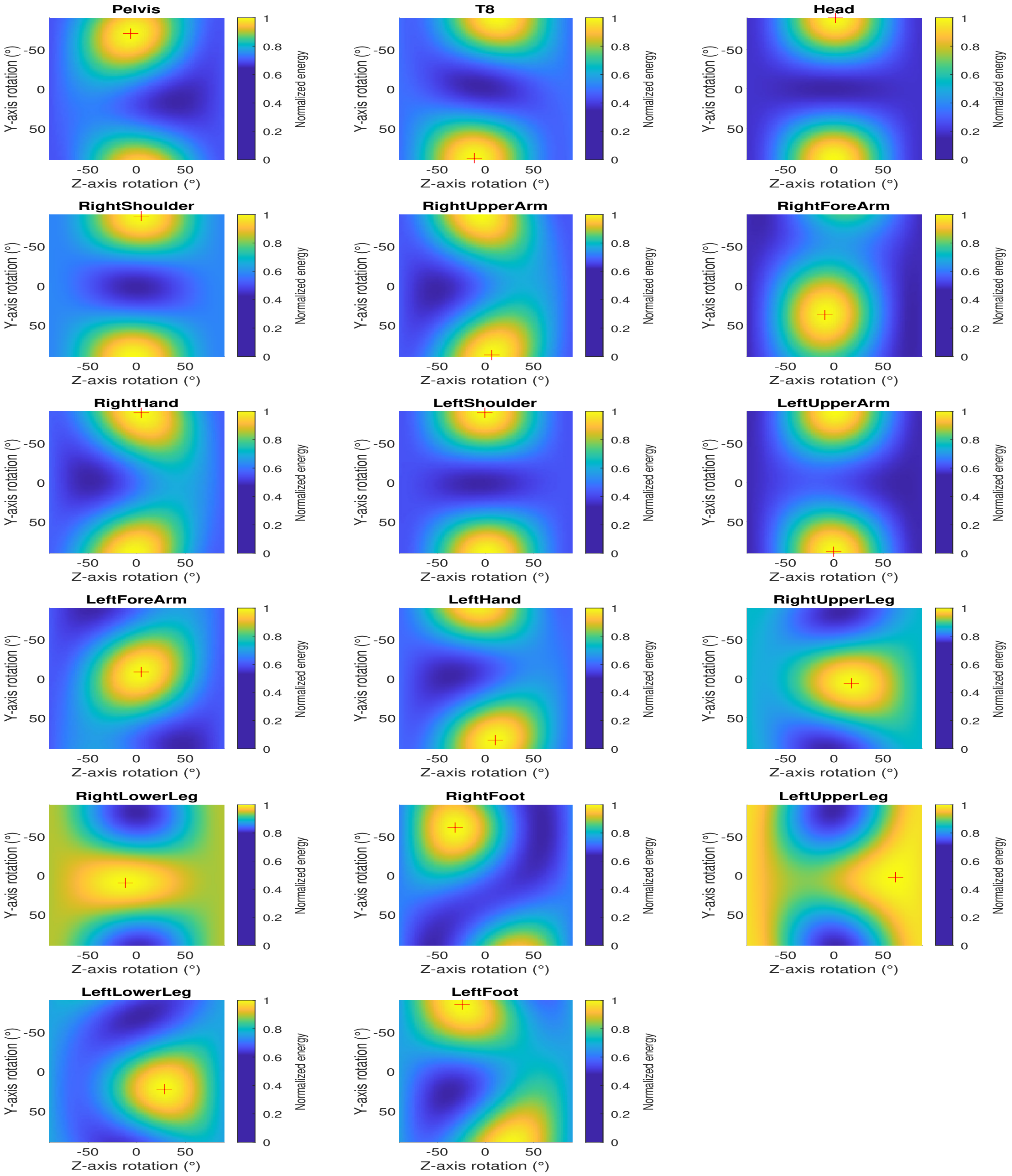

Figure A3 – Orientation influence on harvester normalized energy simulation from IMU local reference frame. Optimal orientation is indicated by a red cross. Xsens location labels are used.

Table A1 – The mean ± standard deviation of the mean absolute errors (MAEs) of the non-dominant arm inclination angle between cloth sensors and skin sensors during the five simulated tasks, with the reference value of skin sensors shown in brackets (N=12).

Non-Dominant arm, inclination	Simulated Work Tasks				
	Lifting boxes	Sorting mails	Wiping floor	Cleaning dishwasher	Cleaning windows
Percentile (°)					
5th	1.1 ± 2 (3.8)	1.4 ± 2.5 (3.5)	2.2 ± 1.7 (9.5)	0.9 ± 1 (5.8)	1.2 ± 1.6 (3.3)
10th	1.4 ± 2.2 (5.4)	1.4 ± 2.5 (4.6)	2.4 ± 1.7 (12.6)	0.9 ± 0.6 (8.6)	1.4 ± 2 (4.7)
50th	1.3 ± 1.7 (15.6)	1.7 ± 2.3 (9.7)	2 ± 1.8 (29.8)	1.9 ± 1.1 (28.8)	1.7 ± 2.2 (13.3)
90th	2.4 ± 1.9 (30.6)	2.2 ± 2.6 (19.4)	2.6 ± 2.4 (51.9)	5.5 ± 4.3 (72.9)	2.8 ± 3.5 (37.6)
95th	3 ± 2.1 (35)	2.8 ± 2.9 (24.4)	2.7 ± 2.4 (57.2)	6.5 ± 4.1 (83.2)	5.4 ± 4.3 (50.8)
Percentage of time (%)					
<20°	4.8 ± 3.8 (65.2)	7.8 ± 20.4 (91.5)	4.3 ± 2.5 (28.9)	3.5 ± 2.3 (37.1)	4.7 ± 6.8 (71.8)
>30°	4.2 ± 5.1 (11.7)	0.9 ± 1.6 (2.3)	3.7 ± 3.3 (48)	2.8 ± 2.3 (47.4)	1.4 ± 2.1 (14.1)
>45°	0.6 ± 1.4 (0.9)	0.4 ± 0.8 (1.2)	3.9 ± 4.9 (22.8)	1.5 ± 1.5 (29.7)	1.2 ± 1.5 (7.4)
>60°	0 ± 0 (0)	0.2 ± 0.3 (0.4)	2.1 ± 3.4 (4.7)	2.2 ± 2.1 (17.6)	0.9 ± 1.3 (4.3)
>90°	0 ± 0 (0)	0 ± 0.1 (0)	0 ± 0 (0.1)	1.8 ± 1.8 (3.4)	0.5 ± 0.8 (1.4)

Table A2 – The mean ± standard deviation of the mean absolute errors (MAEs) of the non-dominant arm inclination velocity between cloth sensors and skin sensors during the five simulated tasks, with the reference value of skin sensors shown in brackets (N=12).

Non-Dominant arm, inclination velocity	Simulated Work Tasks				
	Lifting boxes	Sorting mails	Wiping floor	Cleaning dishwasher	Cleaning windows
Percentile (°/s)					
5th	0.3 ± 0.2 (2.7)	0.2 ± 0.1 (1.5)	0.2 ± 0.1 (1.8)	0.2 ± 0.2 (2.3)	0.3 ± 0.2 (2.6)
10th	0.6 ± 0.4 (6.6)	0.3 ± 0.2 (3.5)	0.2 ± 0.1 (4.4)	0.3 ± 0.3 (5.2)	0.4 ± 0.2 (5.8)
50th	2.1 ± 2.1 (34)	1 ± 0.8 (17.4)	0.5 ± 0.5 (23.5)	1.4 ± 1.1 (30.3)	1.6 ± 1.3 (30.9)
90th	4.9 ± 4.7 (97.7)	3.5 ± 2.4 (52.7)	1.9 ± 1.6 (68.6)	5.5 ± 4.6 (106)	3.7 ± 3 (94.7)
95th	6.6 ± 5.4 (124.6)	4.9 ± 3.7 (69.3)	1.9 ± 1.5 (88)	6.6 ± 4 (140.5)	5 ± 4.3 (122.2)

Table A3 – The mean ± standard deviation of the mean absolute errors (MAEs) of the dominant arm generalized velocity between cloth sensors and skin sensors during the five simulated tasks, with the reference value of skin sensors shown in brackets (N=12).

Dominant arm, generalized velocity	Simulated Work Tasks				
	Lifting boxes	Sorting mails	Wiping floor	Cleaning dishwasher	Cleaning windows
Percentile (°/s)					
5th	1.1 ± 0.6 (11.3)	1.5 ± 0.7 (11.6)	0.6 ± 0.4 (11.1)	0.9 ± 0.6 (10.8)	1.8 ± 1.4 (19.4)
10th	1.4 ± 0.7 (17.1)	2.1 ± 0.8 (17.4)	0.9 ± 0.5 (17.3)	1.2 ± 0.9 (16.6)	2.4 ± 2 (31.3)
50th	4.5 ± 4.3 (53)	7 ± 2.9 (53.1)	5.6 ± 3.3 (57.6)	3.8 ± 2.2 (58.5)	15.3 ± 5.1 (124.2)
90th	21.9 ± 28.1 (134.9)	20.5 ± 11.9 (132.2)	39.7 ± 29.5 (179.9)	15.6 ± 18.7 (170.8)	54 ± 30.1 (324.6)
95th	30.7 ± 40.9 (174.7)	25.9 ± 16.1 (164.9)	58.4 ± 49.7 (256.6)	26.5 ± 35.3 (235.7)	71.5 ± 40.2 (398.1)

Table A4 – The mean ± standard deviation of the mean absolute errors (MAEs) of the non-dominant arm generalized velocity between cloth sensors and skin sensors during the five simulated tasks, with the reference value of skin sensors shown in brackets (N=12).

Non-Dominant arm, generalized velocity	Simulated Work Tasks				
	Lifting boxes	Sorting mails	Wiping floor	Cleaning dishwasher	Cleaning windows
Percentile (°/s)					
5th	1.1 ± 1.2 (11.9)	0.7 ± 0.4 (6.8)	0.6 ± 0.7 (9.2)	1 ± 0.8 (9.6)	0.9 ± 0.9 (12.3)
10th	1.6 ± 1 (17.9)	0.8 ± 0.6 (10.4)	0.9 ± 0.8 (13.7)	1.2 ± 0.7 (14.7)	1 ± 1.1 (18.3)
50th	3.9 ± 3.8 (55.2)	2.7 ± 2.4 (32.7)	2.3 ± 1.4 (41.1)	3.6 ± 1.5 (53.4)	3.4 ± 1.6 (56.6)
90th	29.7 ± 42.1 (145.3)	12.9 ± 17 (94.1)	12.7 ± 23.2 (104.4)	12.5 ± 8.4 (159.4)	18 ± 23.6 (148.5)
95th	39.1 ± 53.2 (191.9)	12.4 ± 8.6 (123.4)	25.8 ± 49.5 (136.6)	22.9 ± 18.7 (216.4)	27.4 ± 35.3 (189.9)

BIBLIOGRAPHY

[1] Nicolas et al. Vignais, « Innovative system for real-time ergonomic feedback in industrial manufacturing », in: Applied ergonomics 44.*4* (2013), pp. 566–574.

[2] David Whiteside et al., « Monitoring hitting load in tennis using inertial sensors and machine learning », in: International journal of sports physiology and performance 12.*9* (2017), pp. 1212–1217.

[3] Technavio, « Inertial Measurement Unit (IMU) Market by Component, End-user, and Geography - Forecast and Analysis 2023-2027 », in: Reports for Electrical Components and Equipment (2023), URL: `https://www.technavio.com/report/inertial-measurement-unit-imu-market-industry-analysis`, (accessed: 23 February 2023).

[4] Mingxing Zhang et al., « Integrated Sensing and Computing for Wearable Human Activity Recognition with MEMS IMU and BLE Network », in: Measurement Science Review 22.*4* (2022), pp. 193–201.

[5] Thomas Kautz et al., « Activity recognition in beach volleyball using a Deep Convolutional Neural Network: Leveraging the potential of Deep Learning in sports », in: Data Mining and Knowledge Discovery 31 (2017), pp. 1678–1705.

[6] Marianne Lossec, « Systèmes multisources de récupération d'énergie dans l'environnement humain : modélisation et optimisation du dimensionnement », Theses, École normale supérieure de Cachan - ENS Cachan, July 2011, URL: `https://theses.hal.science/tel-00618233`.

[7] Salman Khalid et al., « A review of human-powered energy harvesting for smart electronics: recent progress and challenges », in: IJPEM - Green Technology 6 (2019), pp. 821–851.

[8] Yang Bai et al., « Investigation of a cantilever structured piezoelectric energy harvester used for wearable devices with random vibration input », in: Mechanical Systems and Signal Processing 106 (2018), pp. 303–318.

[9] Yuchi Liu et al., « Piezoelectric energy harvesting for self-powered wearable upper limb applications », in: Nano Select 2.*8* (2021), pp. 1459–1479.

[10] Precedence research, « Wearable Technology Market - Global Industry Analysis, Size, Share, Growth, Trends, Regional Outlook, and Forecast 2022-2030 », in: ICT (2022), URL: `https://www.precedenceresearch.com/wearable-technology-market`, (accessed on 23 February 2023).

[11] S Zohreh Homayounfar and Trisha L Andrew, « Wearable sensors for monitoring human motion: a review on mechanisms, materials, and challenges », in: SLAS TECHNOLOGY: Translating Life Sciences Innovation 25.*1* (2020), pp. 9–24.

[12] Nadarajah Manivannan Gobinath Aroganam and David Harrison *, « Consumer Sport Applications », in: Sensors 19 (2019), pp. 1–26.

[13] European Agency for Safety and Health at Work, « Work-related musculoskeletal disorders: prevalence, costs and demographics in the EU, report », in: Publications Office of the European Union (2019), URL: `https://osha.europa.eu/sites/default/files/Work-related_MSDs_prevalence_costs_and_demographics_in_the_EU_report.pdf`, (accessed: 23 February 2023).

[14] Maria Lua et al. Nunes, « Posture Risk Assessment in an Automotive Assembly Line using Inertial Sensors », in: IEEE Access 10 (2022), pp. 83221–83235.

[15] Fan Bo et al., « IMU-Based Monitoring for Assistive Diagnosis and Management of IoHT: A Review », in: Healthcare, vol. 10, 7, MDPI, 2022, p. 1210.

[16] Amin M Nasrabadi et al., « A new scheme for the development of IMU-based activity recognition systems for telerehabilitation », in: Medical Engineering & Physics 108 (2022), p. 103876.

[17] Carlotta Caramia et al., « IMU-based classification of Parkinson's disease from gait: A sensitivity analysis on sensor location and feature selection », in: IEEE journal of biomedical and health informatics 22.*6* (2018), pp. 1765–1774.

[18] Fan Wu, Taiyang Wu, and Mehmet Rasit Yuce, « Design and implementation of a wearable sensor network system for IoT-connected safety and health applications », in: 2019 IEEE 5th World Forum on Internet of Things (WF-IoT), IEEE, 2019, pp. 87–90.

[19] Dhruv R Seshadri et al., « Wearable sensors for monitoring the internal and external workload of the athlete », in: NPJ digital medicine 2.*1* (2019), pp. 1–18.

[20] Jace A Delaney et al., « Acceleration-based running intensities of professional rugby league match play », in: International journal of sports physiology and performance 11.*6* (2016), pp. 802–809.

[21] Jose Manjarres et al., « Physical workload tracking using human activity recognition with wearable devices », in: Sensors 20.*1* (2019), p. 39.

[22] Matthias W et al. Hoppe, « Validity and reliability of GPS and LPS for measuring distances covered and sprint mechanical properties in team sports », in: PloS one 13.*2* (2018), e0192708.

[23] Mareike Roell et al., « Validation of wearable sensors during team sport-specific movements in indoor environments », in: Sensors 19.*16* (2019), p. 3458.

[24] SangUk Han and SangHyun Lee, « A vision-based motion capture and recognition framework for behavior-based safety management », in: Automation in Construction 35 (2013), pp. 131–141, ISSN: 0926-5805, DOI: `https://doi.org/10.1016/j.autcon.2013.05.001`, URL: `https://www.sciencedirect.com/science/article/pii/S0926580513000514`.

[25] Nobuyasu Nakano et al., « Evaluation of 3D markerless motion capture accuracy using OpenPose with multiple video cameras », in: Frontiers in sports and active living 2 (2020), p. 50.

[26] Basilio Pueo Ortega and Jose M Jimenez Olmedo, « Application of motion capture technology for sport performance analysis », in: Retos: nuevas tendencias en educacion fisica, deporte y recreacion *32* (2017), pp. 241–247.

[27] Woojoo Kim et al., « Ergonomic postural assessment using a new open-source human pose estimation technology (OpenPose) », in: International Journal of Industrial Ergonomics 84 (2021), p. 103164.

[28] Catapult, « le clearsky de catapult reçoit la certification "fifa quality" avec la technologie portable la plus performante », in: Blog (2019), URL: `https://www.catapultsports.com/fr/blog/catapults-clearsky-receives-fifa-`

`quality-certification-with-best-performing-wearable-technology`, (accessed on 23 March 2023).

[29] Engadget article: 100 years of motion-capture technology.

[30] Matt Topley and James G Richards, « A comparison of currently available optoelectronic motion capture systems », in: Journal of biomechanics 106 (2020), p. 109820.

[31] Ge Wu et al., « ISB recommendation on definitions of joint coordinate system of various joints for the reporting of human joint motion—part I: ankle, hip, and spine », in: Journal of biomechanics 35.*4* (2002), pp. 543–548.

[32] Ge Wu et al., « ISB recommendation on definitions of joint coordinate systems of various joints for the reporting of human joint motion—Part II: shoulder, elbow, wrist and hand », in: Journal of biomechanics 38.*5* (2005), pp. 981–992.

[33] T.-W. Lu and J.J. O'Connor, « Bone position estimation from skin marker co-ordinates using global optimisation with joint constraints », in: Journal of Biomechanics 32.*2* (1999), pp. 129–134, ISSN: 0021-9290, DOI: `https://doi.org/10.1016/S0021-9290(98)00158-4`, URL: `https://www.sciencedirect.com/science/article/pii/S0021929098001584`.

[34] Gentiane Venture et al., « Monitoring the segment parameters during long term physical training from motion capture data », in: Annual International Conference of the IEEE EMBC, IEEE, 2009, pp. 5247–5250.

[35] Alwin Poulose, Odongo Steven Eyobu, and Dong Seog Han, « An indoor position-estimation algorithm using smartphone IMU sensor data », in: Ieee Access 7 (2019), pp. 11165–11177.

[36] Michael Alexander et al. Wirth, « Comparison of a new inertial sensor based system with an optoelectronic motion capture system for motion analysis of healthy human wrist joints », in: Sensors 19.*23* (2019), p. 5297.

[37] John L Crassidis, « Sigma-point Kalman filtering for integrated GPS and inertial navigation », in: IEEE Transactions on Aerospace and Electronic Systems 42.*2* (2006), pp. 750–756.

[38] Henk Luinge and Per Slycke Daniel Roetenberg, « Xsens MVN: Full 6DOF human motion tracking using miniature inertial sensors, https://www.xsens.com/products/mvn-animate. », in: Xsens Motion Technologies BV, Tech. Rep 1 (2009), pp. 1–7.

[39] Abdo-Rahmane Anas Laaraibi et al., « Flexible dynamic pressure sensor for insole based on inverse viscoelastic model », in: IEEE Sensors Journal (2023).

[40] Muhammad Haseeb Arshad, Muhammad Bilal, and Abdullah Gani, « Human Activity Recognition: Review, Taxonomy and Open Challenges », in: Sensors 22.*17* (2022), p. 6463.

[41] Pratap Chandra Sen, Mahimarnab Hajra, and Mitadru Ghosh, « Supervised classification algorithms in machine learning: A survey and review », in: Emerging technology in modelling and graphics, Springer, 2020, pp. 99–111.

[42] Dakhaz Mustafa Abdullah and Adnan Mohsin Abdulazeez, « Machine learning applications based on SVM classification a review », in: Qubahan Academic Journal 1.*2* (2021), pp. 81–90.

[43] Himani Bhavsar and Mahesh H Panchal, « A review on support vector machine for data classification », in: IJARCET 1.*10* (2012), pp. 185–189.

[44] Larhmam, in: Wikipedia (2018), URL: `https://upload.wikimedia.org/wikipedia/commons/7/72/SVM_margin.png`, (accessed on 23 March 2023).

[45] Sachin Salunkhe et al., « Prediction of life of piercing punches using artificial neural network and adaptive neuro fuzzy inference systems », in: International Journal of Materials Engineering Innovation 10 (Feb. 2019), DOI: `10.1504/IJMATEI.2019.097892`.

[46] Sagar Sharma, Simone Sharma, and Anidhya Athaiya, « Activation functions in neural networks », in: Towards Data Sci 6.*12* (2017), pp. 310–316.

[47] WJ Zhang et al., « On definition of deep learning », in: 2018 World automation congress (WAC), IEEE, 2018, pp. 1–5.

[48] Chigozie Nwankpa et al., « Activation functions: Comparison of trends in practice and research for deep learning », in: arXiv preprint arXiv:1811.03378 (2018).

[49] Filippo Casamassima, Elisabetta Farella, and Luca Benini, « Context aware power management for motion-sensing body area network nodes », in: (2014), pp. 1–6, DOI: `10.7873/date.2014.183`.

[50] Mingyuan Gao et al., « Wearable power management system enables uninterrupted battery-free data-intensive sensing and transmission », in: Nano Energy 107 (2023), p. 108107.

[51] Yasin Emre Durmus et al., « Side by side battery technologies with lithium-ion based batteries », in: Advanced energy materials 10.*24* (2020), p. 2000089.

[52] Marit Mohr et al., « Toward a cell-chemistry specific life cycle assessment of lithium-ion battery recycling processes », in: Journal of Industrial Ecology 24.*6* (2020), pp. 1310–1322.

[53] Luis Moreno-Merino et al., « Comparative assessment of button cells using a normalized index for potential pollution by heavy metals », in: Science of the Total Environment 526 (2015), pp. 187–195.

[54] Movesense, « Movesense Medical sensor », in: Movesense (2023), URL: `https://www.movesense.com/product/movesense-medical/`, (accessed on 24 March 2023).

[55] Yang Zou, Lin Bo, and Zhou Li, « Recent progress in human body energy harvesting for smart bioelectronic system », in: Fundamental Research 1.*3* (2021), pp. 364–382, ISSN: 2667-3258, DOI: `https://doi.org/10.1016/j.fmre.2021.05.002`, URL: `https://www.sciencedirect.com/science/article/pii/S2667325821000698`.

[56] Corina Covaci and Aurel Gontean, « Piezoelectric energy harvesting solutions: A review », in: Sensors 20.*12* (2020), p. 3512.

[57] Alexis Brenes et al., « Maximum power point of piezoelectric energy harvesters: A review of optimality condition for electrical tuning », in: Smart materials and structures 29.*3* (2020), p. 033001.

[58] Guylaine Poulin-Vittrant et al., « Fabrication and characterization of ZnO nanowire-based piezoelectric nanogenerators for low frequency mechanical energy harvesting », in: Physics Procedia 70 (2015), pp. 909–913.

[59] Bao Yang et al., « Recent advances in wearable textile-based triboelectric generator systems for energy harvesting from human motion », in: EcoMat 2.*4* (2020), e12054.

[60] Melissa Hyland et al., « Wearable thermoelectric generators for human body heat harvesting », in: Applied Energy 182 (2016), pp. 518–524.

[61] Achala Satharasinghe, Theodore Hughes-Riley, and Tilak Dias, « A review of solar energy harvesting electronic textiles », in: Sensors 20.*20* (2020), p. 5938.

[62] Waqas Shakoor and Farid Khan, « Solar Based Human Embedded Energy Harvester », in: IBCAST, IEEE, 2021, pp. 432–438.

[63] Husam Hamid Ibrahim et al., « Radio frequency energy harvesting technologies: A comprehensive review on designing, methodologies, and potential applications », in: Sensors 22.*11* (2022), p. 4144.

[64] Petar Jokic and Michele Magno, « Powering smart wearable systems with flexible solar energy harvesting », in: 2017 IEEE International symposium on circuits and systems (ISCAS), IEEE, 2017, pp. 1–4.

[65] Dieff Vital, Shubhendu Bhardwaj, and John L Volakis, « Textile-based large area RF-power harvesting system for wearable applications », in: IEEE Transactions on Antennas and Propagation 68.*3* (2019), pp. 2323–2331.

[66] Jarosław Kwapień and Stanisław Drożdż, « Physical approach to complex systems », in: Physics Reports 515.*3-4* (2012), pp. 115–226.

[67] Joaquim RRA Martins and Andrew Ning, Engineering design optimization, Cambridge University Press, 2021.

[68] Miqing Li, Shengxiang Yang, and Xiaohui Liu, « Diversity comparison of Pareto front approximations in many-objective optimization », in: IEEE Transactions on Cybernetics 44.*12* (2014), pp. 2568–2584.

[69] Kalyanmoy Deb et al., « A fast and elitist multiobjective genetic algorithm: NSGA-II », in: IEEE transactions on evolutionary computation 6.*2* (2002), pp. 182–197.

[70] Russell Eberhart and James Kennedy, « Particle swarm optimization », in: Proceedings of the IEEE international conference on neural networks, vol. 4, Citeseer, 1995, pp. 1942–1948.

[71] Marco Dorigo and Gianni Di Caro, « Ant colony optimization: a new meta-heuristic », in: Proceedings of the 1999 congress on evolutionary computation, vol. 2, IEEE, 1999, pp. 1470–1477.

[72] Khaled Mohamed, Hassan Elgamal, and Sallam A Kouritem, « An experimental validation of a new shape optimization technique for piezoelectric harvesting cantilever beams », in: Alexandria Engineering Journal 60.*1* (2021), pp. 1751–1766.

[73] Jane McCann and David Bryson, Smart clothes and wearable technology, Woodhead Publishing, 2022.

[74] Ezgi Ismar et al., « Futuristic clothes: electronic textiles and wearable technologies », in: Global Challenges 4.*7* (2020), p. 1900092.

[75] Sol Lim and Clive D'Souza, « A narrative review on contemporary and emerging uses of inertial sensing in occupational ergonomics », in: International journal of industrial ergonomics 76 (2020), p. 102937.

[76] Michael Lorenz et al., « Towards Artefact Aware Human Motion Capture using Inertial Sensors Integrated into Loose Clothing », in: 2022 International Conference on Robotics and Automation (ICRA), IEEE, 2022, pp. 1682–1688.

[77] Udeni Jayasinghe, William S Harwin, and Faustina Hwang, « Comparing clothing-mounted sensors with wearable sensors for movement analysis and activity classification », in: Sensors 20.*1* (2019), p. 82.

[78] Sam Gleadhill, Daniel James, and James Lee, « Validating temporal motion kinematics from clothing attached inertial sensors », in: Proceedings, vol. 2, 6, MDPI, 2018, p. 304.

[79] Valentina Camomilla, Raphaël Dumas, and Aurelio Cappozzo, « Human movement analysis: The soft tissue artefact issue », in: Journal of biomechanics 62 (2017), pp–1.

[80] Hassan Elahi, Marco Eugeni, and Paolo Gaudenzi, « A review on mechanisms for piezoelectric-based energy harvesters », in: Energies 11.*7* (2018), p. 1850.

[81] Xue Ying, « An overview of overfitting and its solutions », in: Journal of physics: Conference series, vol. 1168, IOP Publishing, 2019, p. 022022.

[82] Roberto de Fazio et al., « Development of a self-powered piezo-resistive smart insole equipped with low-power ble connectivity for remote gait monitoring », in: Sensors 21.*13* (2021), p. 4539.

[83] Youngsu Cha et al., « Flexible piezoelectric energy harvesting from mouse click motions », in: Sensors 16.*7* (2016), p. 1045.

[84] Suna Ju and Chang-Hyeon Ji, « Impact-based piezoelectric vibration energy harvester », in: Applied Energy 214 (2018), pp. 139–151.

[85] Keli Li et al., « Wearable energy harvesters generating electricity from low-frequency human limb movement », in: Microsystems & nanoengineering 4.*1* (2018), p. 24.

[86] Iman Izadgoshasb et al., « Optimizing orientation of piezoelectric cantilever beam for harvesting energy from human walking », in: Energy conversion and management 161 (2018), pp. 66–73.

[87] Alper Erturk and Daniel J Inman, Piezoelectric energy harvesting, John Wiley & Sons, 2011.

[88] Xuesu Xiao and Shuayb Zarar, « Machine learning for placement-insensitive inertial motion capture », in: 2018 IEEE International Conference on Robotics and Automation (ICRA), IEEE, 2018, pp. 6716–6721.

[89] Damien Hoareau et al., « Synthetized inertial measurement units (IMUs) to evaluate the placement of wearable sensors on human body for motion recognition », in: The Journal of Engineering 2022.*5* (2022), pp. 536–543.

[90] « Accuracy of human motion capture systems for sport applications; state-of-the-art review », in: European Journal of Sport Science 18.*6* (2018), pp. 806–819, ISSN: 15367290, DOI: `10.1080/17461391.2018.1463397`, URL: `https://doi.org/10.1080/17461391.2018.1463397`.

[91] Manon Kok, Jeroen D. Hol, and Thomas B. Sch"on, « Using inertial sensors for position and orientation estimation », in: Foundations and Trends in Signal Processing 11.*1-2* (2017), pp. 1–153, ISSN: 19328354, DOI: `10.1561/2000000094`, arXiv: `1704.06053`.

[92] Emily E. Cust et al., « Machine and deep learning for sport-specific movement recognition: a systematic review of model development and performance », in: Journal of Sports Sciences 37.*5* (2019), pp. 568–600, ISSN: 1466447X, DOI: `10.1080/02640414.2018.1521769`, URL: `https://doi.org/10.1080/02640414.2018.1521769`.

[93] Nor Surayahani Suriani, Fadilla Atyka Nor Rashid, and Nur Yuzailin Yunos, « Optimal accelerometer placement for fall detection of rehabilitation patients », in: Journal of Telecommunication, Electronic and Computer Engineering 10.*2-5* (2018), pp. 25–29, ISSN: 22898131.

[94] Seungeun Chung et al., « Sensor data acquisition and multimodal sensor fusion for human activity recognition using deep learning », in: Sensors (Switzerland) 19.*7* (2019), ISSN: 14248220, DOI: `10.3390/s19071716`.

[95] Antoine Muller et al., « CusToM: a Matlab toolbox for musculoskeletal simulation », in: Journal of Open Source Software 4.*33* (2019), pp. 1–3.

[96] Hendrio Bragança et al., « A smartphone lightweight method for human activity recognition based on information theory », in: Sensors 20.*7* (2020), p. 1856.

[97] Ram Shankar Pathak, The wavelet transform, vol. 4, Springer Science & Business Media, 2009.

[98] Ståle Andreas van Dorp Skogstad et al., « Filtering motion capture data for real-time applications », in: (2013).

[99] Enders Robinson and Dean Clark, « Sampling and the Nyquist frequency », in: The Leading Edge 10.*3* (1991), pp. 51–53.

[100] Dana Solav et al., « Bone orientation and position estimation errors using Cosserat point elements and least squares methods: Application to gait », in: Journal of biomechanics 62 (2017), pp. 110–116.

[101] Roberto Lugo, Peter Kung, and C Benjamin Ma, « Shoulder biomechanics », in: European journal of radiology 68.*1* (2008), pp. 16–24.

[102] Damien Hoareau et al., « Available Kinetic Energy Sources on the Human Body during Sports Activities: A Numerical Approach Based on Accelerometers for Cantilevered Piezoelectric Harvesters », in: Energies 16.*6* (2023), p. 2695.

[103] Alessandro Nastro et al., « Wearable Ball-Impact Piezoelectric Multi-Converters for Low-Frequency Energy Harvesting from Human Motion », in: Sensors 22.*3* (2022), p. 772.

[104] Srimanta Baishya et al., « A high precision lumped parameter model for piezoelectric energy harvesters », in: IEEE Sensors Journal 17.*24* (2017), pp. 8350–8355.

[105] Henry A Sodano, Gyuhae Park, and DJ Inman, « Estimation of electric charge output for piezoelectric energy harvesting », in: Strain 40.*2* (2004), pp. 49–58.

[106] Alper Erturk and Daniel J Inman, « A distributed parameter electromechanical model for cantilevered piezoelectric energy harvesters », in: Journal of vibration and acoustics 130.*4* (2008).

[107] Nicholas M Stone and Andrew E Kilding, « Aerobic conditioning for team sport athletes », in: Sports Medicine 39 (2009), pp. 615–642.

[108] Jonathan M Lilly, « Element analysis: A wavelet-based method for analysing time-localized events in noisy time series », in: Proceedings A: Mathematical, Physical and Engineering Sciences 473.*2200* (2017), p. 20160776.

[109] Donald B Percival and Harold O Mofjeld, « Analysis of subtidal coastal sea level fluctuations using wavelets », in: Journal of the American Statistical Association 92.*439* (1997), pp. 868–880.

[110] TL Lago, « Digital sampling according to Nyquist and Shannon », in: Sound and vibration 36.*2* (2002), pp. 20–22.

[111] Adrien Morel et al., « A comparative study of electrical interfaces for tunable piezoelectric vibration energy harvesting », in: Smart Materials and Structures 31.*4* (2022), p. 045016.

[112] Giulia Bassani, Alessandro Filippeschi, and Carlo Alberto Avizzano, « Manual Material Handling Dataset for Biomechanical and Ergonomics Analysis. », in: (Apr. 2021), DOI: `10.5281/zenodo.4633087`, URL: `https://doi.org/10.5281/zenodo.4633087`.

[113] Giulia Bassani, Alessandro Filippeschi, and Carlo Alberto Avizzano, « A Dataset of Human Motion and Muscular Activities in Manual Material Handling Tasks for Biomechanical and Ergonomic Analyses », in: IEEE Sensors Journal 21.*21* (2021), pp. 24731–24739.

[114] Daniel Roetenberg, Henk Luinge, Per Slycke, et al., « Xsens MVN: Full 6DOF human motion tracking using miniature inertial sensors », in: Xsens Motion Technologies BV, Tech. Rep 1 (2009), pp. 1–7.

[115] Antonio A Aguileta et al., « Multi-sensor fusion for activity recognition—A survey », in: Sensors 19.*17* (2019), p. 3808.

[116] Emily E Cust et al., « Machine and deep learning for sport-specific movement recognition: a systematic review of model development and performance », in: Journal of sports sciences 37.*5* (2019), pp. 568–600.

[117] Ben D Fulcher and Nick S Jones, « hctsa: A computational framework for automated time-series phenotyping using massive feature extraction », in: Cell systems 5.*5* (2017), pp. 527–531.

[118] Carl H Lubba et al., « catch22: CAnonical Time-series CHaracteristics: Selected through highly comparative time-series analysis », in: Data Mining and Knowledge Discovery 33.*6* (2019), pp. 1821–1852.

[119] Jayanta Kumar Basu, Debnath Bhattacharyya, and Tai-hoon Kim, « Use of artificial neural network in pattern recognition », in: International journal of software engineering and its applications 4.*2* (2010).

[120] Abdul Hafiz Alameh, Mathieu Gratuze, and Frederic Nabki, « Impact of geometry on the performance of cantilever-based piezoelectric vibration energy harvesters », in: IEEE Sensors Journal 19.*22* (2019), pp. 10316–10326.

[121] Oliver A Bauchau and James I Craig, « Euler-Bernoulli beam theory », in: Structural analysis (2009), pp. 173–221.

[122] Alper Erturk and Daniel J Inman, « On mechanical modeling of cantilevered piezoelectric vibration energy harvesters », in: Journal of intelligent material systems and structures 19.*11* (2008), pp. 1311–1325.

[123] Majid Khazaee et al., « The investigation of viscous and structural damping for piezoelectric energy harvesters using only time-domain voltage measurements », in: Applied Energy 285 (2021), p. 116427.

[124] Damien Hoareau et al., « Evaluation of In-Cloth Versus On-Skin Sensors for Measuring Trunk and Upper Arm Postures and Movements », in: Sensors 23.*8* (2023), p. 3969.

[125] Jan De Kok et al., « Work-related MSDs: prevalence, costs and demographics in the EU (European Risk Observatory Executive summary) », in: Publications Office of the European Union (2019), pp. 1–18.

[126] Ida Ahlberg, « The economic costs of musculoskeletal disorders-A cost-of-illness study in Sweden for 2012 », in: (2014).

[127] Allard J Van Der Beek et al., « A research framework for the development and implementation of interventions preventing work-related musculoskeletal disorders », in: Scandinavian Journal of Work, Environment & Health (2017), pp. 526–539.

[128] Richard Wells, « Why have we not solved the MSD problem? », in: Work 34.*1* (2009), pp. 117–121.

[129] M Forsman et al., « The search for practical and reliable observational or technical risk assessment methods to be used in prevention of musculoskeletal disorders », in: Agron. Res 15 (2017), pp. 680–686.

[130] Carel TJ Hulshof et al., « The prevalence of occupational exposure to ergonomic risk factors: A systematic review and meta-analysis from the WHO/ILO Joint Estimates of the Work-related Burden of Disease and Injury », in: Environment international 146 (2021), p. 106157.

[131] Gert-Åke Hansson et al., « Questionnarie versus direct technical measurements in assessing postures and movements of the head, upper back, arms and hands », in: Scandinavian journal of work, environment & health (2001), pp. 30–40.

[132] Markus Koch et al., « Validity of questionnaire and representativeness of objective methods for measurements of mechanical exposures in construction and health care work », in: PLoS One 11.*9* (2016), e0162881.

[133] Esa-Pekka Takala et al., « Systematic evaluation of observational methods assessing biomechanical exposures at work », in: Scandinavian journal of work, environment & health (2010), pp. 3–24.

[134] Ida-Märta Rhén and Mikael Forsman, « Inter-and intra-rater reliability of the OCRA checklist method in video-recorded manual work tasks », in: Applied Ergonomics 84 (2020), p. 103025.

[135] Nidhi Gupta et al., « How does accelerometry-measured arm elevation at work influence prospective risk of long-term sickness absence? », in: Scandinavian Journal of Work, Environment & Health 48.*2* (2022), p. 137.

[136] Nidhi Gupta et al., « Does occupational forward bending of the back increase long-term sickness absence risk? A 4-year prospective register-based study using device-measured compositional data analysis », in: Scandinavian Journal of Work, Environment & Health 48.*8* (2022), pp. 651–661.

[137] Inger Arvidsson et al., « Action levels for the prevention of work-related musculoskeletal disorders in the neck and upper extremities: a proposal », in: Annals of Work Exposures and Health 65.*7* (2021), pp. 741–747.

[138] Di Wang, Fei Dai, and Xiaopeng Ning, « Risk assessment of work-related musculoskeletal disorders in construction: State-of-the-art review », in: Journal of Construction Engineering and management 141.*6* (2015), p. 04015008.

[139] Antonio Lanata et al., « A new smart-fabric based body area sensor network for work risk assessment », in: 2020 IEEE International Workshop on Metrology for Industry 4.0 & IoT, IEEE, 2020, pp. 187–190.

[140] Liyun Yang et al., « Towards smart work clothing for automatic risk assessment of physical workload », in: Ieee Access 6 (2018), pp. 40059–40072.

[141] Karnica Manivasagam and Liyun Yang, « Evaluation of a New Simplified Inertial Sensor Method against Electrogoniometer for Measuring Wrist Motion in Occupational Studies », in: Sensors 22.*4* (2022), p. 1690.

[142] Chunxi Huang et al., « Development and validation of a wearable inertial sensors-based automated system for assessing work-related musculoskeletal disorders in the workspace », in: International Journal of Environmental Research and Public Health 17.*17* (2020), p. 6050.

[143] Xuanxuan Zhang et al., « Manufacturing worker perceptions of using wearable inertial sensors for multiple work shifts », in: Applied ergonomics 98 (2022), p. 103579.

[144] Elisa Digo, Stefano Pastorelli, and Laura Gastaldi, « A Narrative Review on Wearable Inertial Sensors for Human Motion Tracking in Industrial Scenarios », in: Robotics 11.*6* (2022), p. 138.

[145] Xuelong Fan et al., « Effects of sensor types and angular velocity computational methods in field measurements of occupational upper arm and trunk postures and movements », in: Sensors 21.*16* (2021), p. 5527.

[146] Howard Chen, Mark C Schall Jr, and Nathan B Fethke, « Measuring upper arm elevation using an inertial measurement unit: An exploration of sensor fusion algorithms and gyroscope models », in: Applied ergonomics 89 (2020), p. 103187.

[147] Liyun Yang, Wilhelmus JA Grooten, and Mikael Forsman, « An iPhone application for upper arm posture and movement measurements », in: Applied ergonomics 65 (2017), pp. 492–500.

[148] GA Hansson et al., « Validity and reliability of triaxial accelerometers for inclinometry in posture analysis », in: Medical and biological engineering and computing 39 (2001), pp. 405–413.

[149] Rudolph Emil Kalman, « A new approach to linear filtering and prediction problems », in: (1960).

[150] Catarina Nordander et al., « Exposure–response relationships for work-related neck and shoulder musculoskeletal disorders–Analyses of pooled uniform data sets », in: Applied ergonomics 55 (2016), pp. 70–84.

[151] Jens Wahlström et al., « Full-shift trunk and upper arm postures and movements among aircraft baggage handlers », in: Annals of Occupational Hygiene 60.*8* (2016), pp. 977–990.

[152] Mikael Forsman et al., « Mind the gap–development of conversion models between accelerometer-and IMU-based measurements of arm and trunk postures and movements in warehouse work », in: Applied Ergonomics 105 (2022), p. 103841.

[153] Jessica Stanley et al., « A review of connectors and joining technologies for electronic textiles », in: Engineering Reports 4.*6* (2022), e12491.

[154] Xuzhong Yan et al., « Wearable IMU-based real-time motion warning system for construction workers' musculoskeletal disorders prevention », in: Automation in construction 74 (2017), pp. 2–11.

[155] Daning Hao et al., « Solar energy harvesting technologies for PV self-powered applications: A comprehensive review », in: Renewable Energy (2022).

COLLEGE DOCTORAL BRETAGNE
MATHS, TELECOMS
INFORMATIQUE, SIGNAL
SYSTEMES, ELECTRONIQUE

rennes
école
normale
supérieure

Titre : Optimisation du positionnement de capteurs et de récupérateurs d'énergie pour la conception de systèmes portables de reconnaissance d'activité physique.

Mot clés : Activité physique, Centrales inertielles, Récupérateurs piézoélectriques, Optimisation, Classification

Résumé : L'analyse des mouvements humains offre la possibilité d'évaluer et d'améliorer par exemple les performances sportives. Des systèmes embarqués portables ont ainsi vu le jour avec l'utilisation de centrales inertielles (IMU). Cependant, des problématiques subsistent, la détermination du nombre ou encore du placement de ces systèmes sur le corps humain n'est pas trivial et représente une problématique commune à toutes les applications. Cette thèse propose d'étudier les sources d'informations sur le corps humain permettant de placer de manière optimale ces systèmes. Les méthodes employées se basent sur l'utilisation d'algorithmes d'apprentissage supervisée comme le SVM et sur un modèle biomécanique. Portées par le contexte des capteurs portables, les notions de système embarqué et d'autonomie sont aussi abordées. Un aspect énergétique est traité à travers la simulation de générateurs piézoélectriques. Ainsi, une analyse des sources d'énergie pour différents placements et orientations de récupérateurs sur le corps humain est conduite. Enfin, une méthode d'optimisation multicritère est implémentée pour répondre aux problématiques visées par cette thèse.

Title: Optimization of the positioning of sensors and energy harvesters for the design of portable physical activity recognition systems.

Keywords: Physical activity, IMU, Piezoelectric harvesters, Optimization, Classification

Abstract: The analysis of human motion offers the possibility of evaluating and improving sports performance, for example. Wearable systems have been developed using inertial measurement units (IMU). However, there are still issues, the determination of the number or the placement of these systems on the human body is not trivial and represents a common challenge to all applications. This thesis aims at investigating the sources of information on the human body in order to optimize the placement of these systems. The methods employed are based on the use of supervised learning algorithms such as SVM and on a biomechanical model. In the context of wearable sensors, the notions of embedded system and autonomy are also addressed. An energetic aspect is treated through the simulation of piezoelectric generators. Thus, an analysis of energy sources for different placements and orientations of harvesters on the human body is conducted. Finally, a multi-objective optimization method is implemented to meet the objectives of this thesis.